Magnetic thin film Fe ring structures and devices

Yufeng Hou

A dissertation

Submitted in partial fulfillment of the

Requirements for the degree of

Doctor of Philosophy

University of Washington

2014

Reading Committee:

Kannan M. Krishnan, Chair

Majorie Olmstead

Marco Rolandi

Program Authorized to Offer Degree:

Materials Science & Engineering

University of Washington

Abstract

Magnetic thin film Fe ring structures and devices

Yufeng Hou

Chair of the Supervisory Committee:
Professor Kannan M. Krishnan
Materials Science & Engineering

Magnetic thin film ring structures show distinct magnetic states and highly reproducible switching behavior, which makes them candidates for multiple magnetoelectronic and sensing devices. The magnetic states and switching behaviors of thin film ring structures are closely related to their physical properties such as the lateral size, thickness, width and the material anisotropy.

In order to systematically study the magnetic properties of thin film ring structures, we use different techniques such as photolithography and electron-beam lithography to fabricate magnetic thin film Fe ring structures with different outer diameter (D_{out}), thickness (t_{Fe}) and inner-to-outer diameter ratio (D_{in}/D_{out}). The magnetization reversal processes of these Fe ring structures are studied using magneto-optical Kerr effect and magnetic force microscopy. To explain the magnetic behavior of the Fe ring structures observed in experiments, we use LLG micromagnetic simulation to model the domain

configuration of the Fe ring during switching. The evolution of magnetic reversal behaviors in Fe ring structures is also explained by calculating the energy densities of vortex state, single-domain state and axial state with micromagnetic simulator.

To control the magnetic switching behavior of the Fe ring structures, exchange bias interfacial coupling is introduced into the ring structure by growing a bilayer of IrMn/Fe in the ring structure. By studying the angular dependence of the hysteresis loop shift, we find that exchange bias induces a magnetic unidirectional anisotropy and a collinear magnetic uniaxial anisotropy in the ring structure. Exchange bias induced magnetic anisotropies cause anisotropic magnetic reversal modes in IrMn/Fe (10 nm) ring and a higher one-step to two-step transitional thickness in IrMn/Fe (*x* nm) ring structures.

After study the magnetic properties of the Fe rings and exchange biased IrMn/Fe rings, we incorporate them into one ring shape magnetic tunneling junction device with current perpendicular to plane configuration. In the ring-MTJ device, a Fe ring free layer and an exchange biased IrMn/Fe ring pinned layer are sandwiched by an MgO barrier layer between them. Depending on the relative orientation of the magnetization in the Fe ring and IrMn/Fe ring, the resistance of the device is higher when they are antiparallel than parallel, which may be used as memory element in a magnetoresistive random-access memory.

ACKNOWLEDGEMENTS

First, I would like to thank my supervisor, Professor Kannan M. Krishnan for giving me this wonderful opportunity to join his group and work in the field of magnetism. In my 6 years of Ph.D life, he offered me a lot of his encouragement and guidance. The research is always challenging, but he leads me throughout all the difficulties to this point. I also would like to thank him for giving me the opportunity to be trained on many different techniques and in industry during the summers.

I also want to thank my committee members, Prof. Marjorie Olmstead, Prof. Marco Rolandi and Prof. Qiuming Yu for their time and insight, which helped to make this work complete.

A lot of people kindly offered me help with measurements and data interpretation in this thesis. I want to thank Dr. Dirk Weiss for his instructions on lithographically patterning. Dr. Yuanming Liu, Dr. Shuhong Xie for their help on the magnetic force microscopy. I want to thank Dr. Michael Sheinfein for his instructions on the micromagnetic simulations.

The colleagues in my group also offered me great support in the past 6 years. Here I want thank many past and current members of the group: Dr. Tianlong Wen, Dr. Yicheng Li, Dr. Matt Ferguson, Dr. Amit Khandhar, Zheng Li and Hamed Arami for their kind scientific and emotional support.

Finally, my deepest appreciation belongs to my family. Without their support through the years, I would not have been able to go this far.

TABLE OF CONTENTS

page

Chapter 1

FERROMAGNETIC RING STRUCTURES AND CRITICAL LENGTH SCALES FOR NANOMAGNETISM

1.1 Introduction and background

With continuously improving fabrication techniques in thin film deposition [1], lithography patterning [2] and self-assembly, [3] the past decade has witnessed a vast boom in research of magnetic thin film structures [1,4] and devices [5] with lateral dimensions approaching the critical length scales where the basic magnetic interactions compete with each other in magnitude. [6] By carefully modulating the atomic, electronic and chemical structure of the thin film via controlling its growth condition, [7] or physically confining it in one, two or all three dimensions, [8] these new magnetic thin-film structures with reduced size exhibit distinct magnetic properties that are significantly different from their bulk counterparts. [9] This enhances their potential use as platforms for studying new physical phenomena in the nanometer scale [10] and inspires novel devices with enhanced performance. [11]

1.2 Magnetic vortex state in ferromagnetic nano-disks and rings

Among all the magnetic thin-film structures, circular shaped 2-D magnetic disk and ring structures are of particular interest because of their flux closure vortex state. First discovered in 2000, [12] the magnetic vortex state in circular disks has attracted a lot of

research interests in the past decade. [13, 14, 15, 16, 17] As shown in Figure 1.1, if the material of the disk does not have strong magnetocrystalline anisotropy, at remanence (external field $H_{ex} = 0$), in order to minimize the magnetostatic energy, the magnetic moments of the disk tend to curl around the disk edges to form close loops along the azimuthal angle direction, which is called a vortex state.

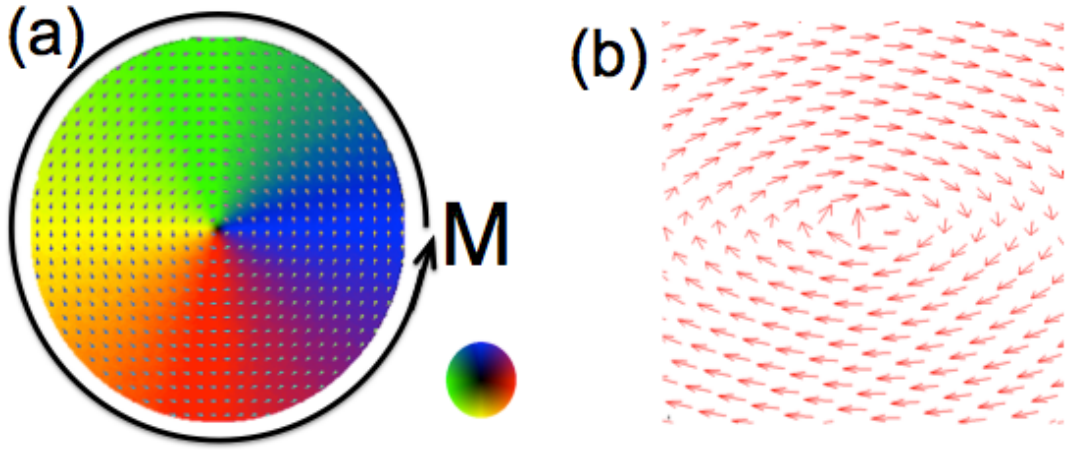

Figure 1.1 (a) In-plane view of the spin configurations of vortex state in thin film disk (b) magnetic moment in the center of the vortex core is pointing in the out-of-plane direction.

For such a 2-D circular disk in vortex state, there are no net magnetization and no stray fields in the disk plane, which results in zero magnetostatic energy. The only energy price comes from the exchange interaction that exists between neighboring non-parallel moments. However, as you approach the center of the disk, as the curvature of the closed loop increases, the angle between adjacent spins become larger and larger, the magnitude of the exchange energy between neighboring spins increases accordingly and finally the exchange interaction forces the spins to align along the normal direction of the disk plane,

forming a structure called vortex core [Figure 1.1(b)]. For polycrystalline Fe, the vortex core size is reported to be 14 nm in diameter. [18]

In the vortex state of the magnetic thin-film disk, there exist two degrees of freedom, as shown in Figure 1.2: (1) the direction of the vortex core magnetic moment, or polarity, can either point up or point down; (2) the circulation direction of the magnetization in the disk plane, or chirality, can either be clockwise (CW) or counter-clockwise (CCW). Theoretical simulation and experiment show that these two degrees of freedom are independent of each other, i.e. you can change the polarity of the center moment without affecting the chirality of the disk, and vice versa.

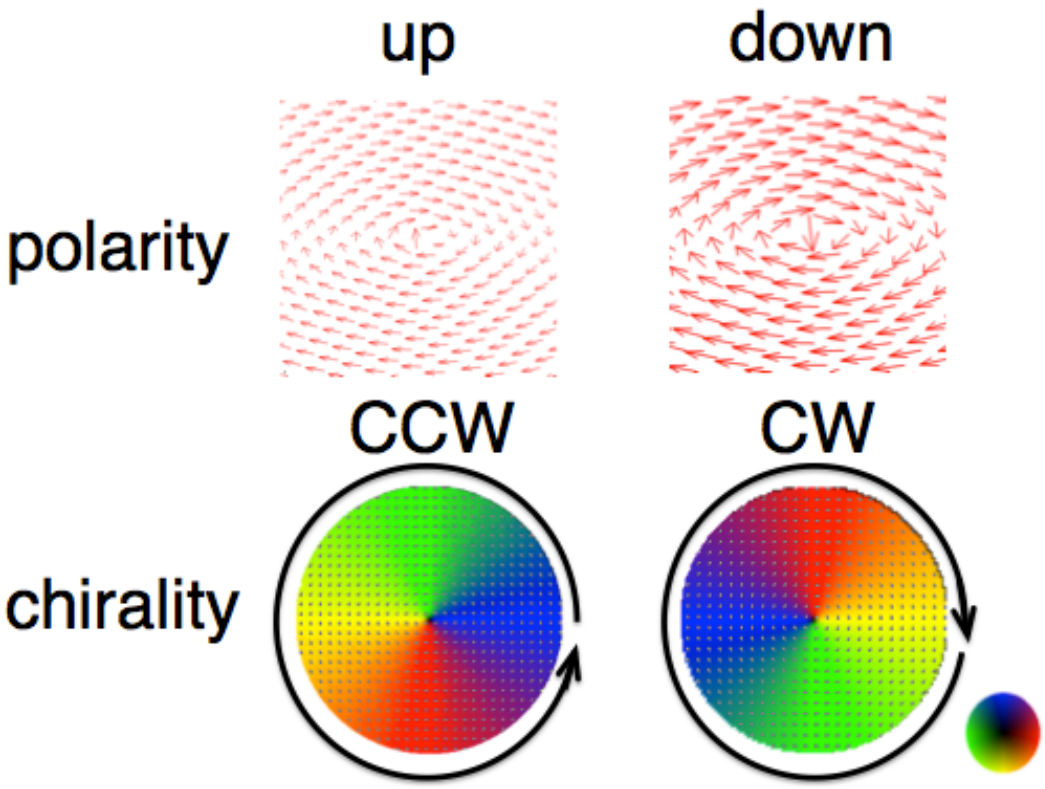

Figure 1.2 Two degrees of freedom in the magnetic vortex state of disks: polarity and chirality

Because of its zero stray field, high stability and two degrees of freedom, magnetic thin-film disk has been proposed as the potential candidate for high density magnetic recording media, [19] elements of magnetic logic device [20] and magnetic agents for in-vitro hyperthermia to kill cancer cells.[21]

However, as discussed earlier, formation of the vortex state sacrifices the exchange energy to minimize magnetostatic energy. As a result, the energy density per volume of the disk increases drastically as you approach the disk center. In Figure 1.3(b), we plot the energy density map of the magnetic thin-film disk in vortex state. The vortex core area appears as a bright spot in the center with very high energy density compared to the rest of the disk.

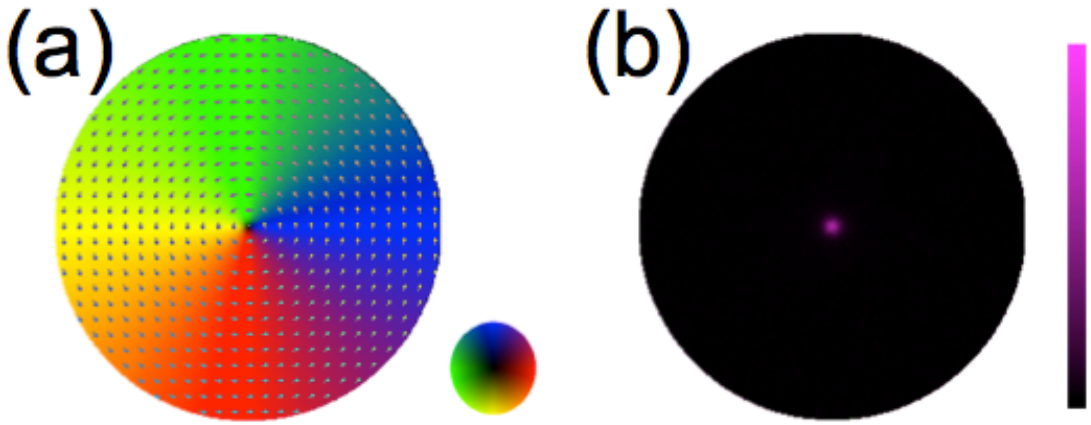

Figure 1.3 (a) Spin configuration of the magnetic thin-film disk in vortex state (b) energy density map of (a), showing the high energy vortex core in the center of the disk.

In large magnetic thin-film disk (outer diameter larger than $1\ \mu m$), compared with the energy saving by forming the vortex state, the vortex core only adds a small amount to the total energy of the disk. However, as the size of the disk decreases to the nanometer

range, the energy contribution of the vortex core becomes an increasingly significant part of the total energy of the disk. According to theoretical calculations, report shows that the energy of vortex core is so high that the vortex state is not stable in permalloy magnetic thin-film disks below 100 nm. [22] For disks with smaller size, it forms single-domain state in which all the spins in the disk are aligned along one direction in the disk plane. This critical size of the magnetic vortex state is fatal for applications such as magnetic storage because it sets the lower boundary of the recording element size and severely limits the recording density.

One solution to the size limitation problem is simply removing the vortex core from the center of the disk. By eliminating the central portion of the disk, it can be switched to a ring. The magnetic thin-film ring loses the freedom of the vortex core polarity but still keeps the freedom of chirality in its vortex state, as shown in Figure 1.4(a). As a result of the removal of the high-energy vortex core, the vortex state in magnetic thin-film ring structure is far more stable than disk. Theoretical calculations [23] show that the vortex state is stable in ring structures with an outer diameter as small as 30 nm. Because of its ability to maintain vortex state at small size, ferromagnetic ring structure has been proposed as a practical type of high-density data storage devices, [24, 25, 26, 27] magnetic logics [28] and biomedical sensors. [29]

1.3 Magnetic states and switching behavior of ferromagnetic nanorings

Besides the flux-closure magnetic vortex state, some other unique magnetic states, such as the onion state, have been found in ring structures. The onion state is usually formed in

the remanence state after the ferromagnetic ring is saturated by an in-plane external magnetic field. A pair of 180° head-on domain walls are formed in the original field direction, as shown in Figure 1.4(b). Because of this pair of domain walls, the onion state in the ring structure provide an ideal platform to study the structure [30] and motion [31] of magnetic domain walls, and their interactions with each other. [32]

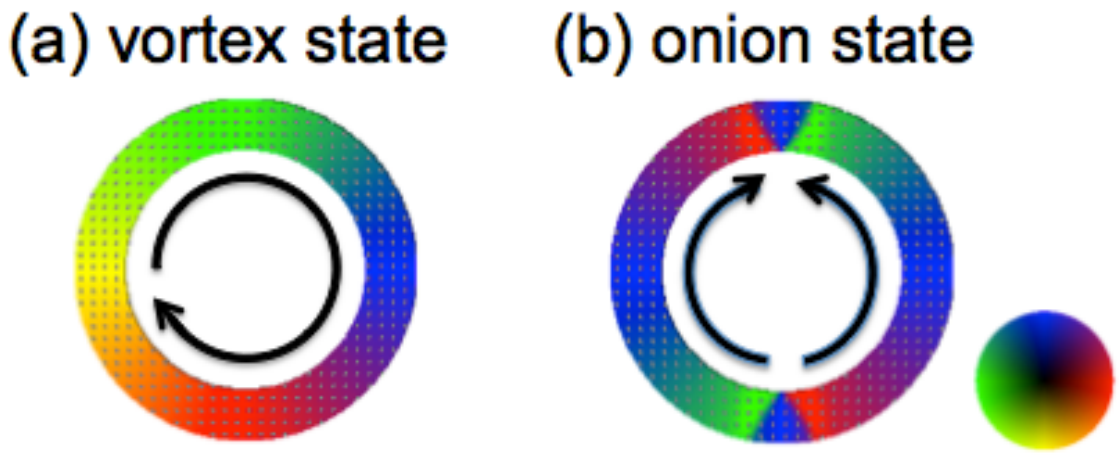

Figure 1.4 Magnetic states in thin film ring structure (a) vortex state (b) onion state.

For fundamental science and applications purposes, the magnetic switching behavior of the ferromagnetic ring structures between these states is an interesting research subject. Reports show that the switching process is highly sensitive to the size, [33, 34] width, [35] thickness, [36] and anisotropy [37] of the ring.

Generally, two types of switching processes have been observed in the ring structures, as shown in Figure 1.5. The first type is the single-step switching, where the hysteresis loop of the ring shows a single jump from positive saturation [Figure 1.5(a)] to negative saturation [Figure 1.5(e)]. The ferromagnetic ring remains in the high remanence quasi-saturated state at remanence [Figure 1.5(c)], at coercive field, H_c, the magnetization of

the ring reverses via domain nucleation and growth [Figure 1.5(d)]. After the nucleation step, the magnetization of the ring is fully reversed in the negative direction [Figure 1.5(e)].

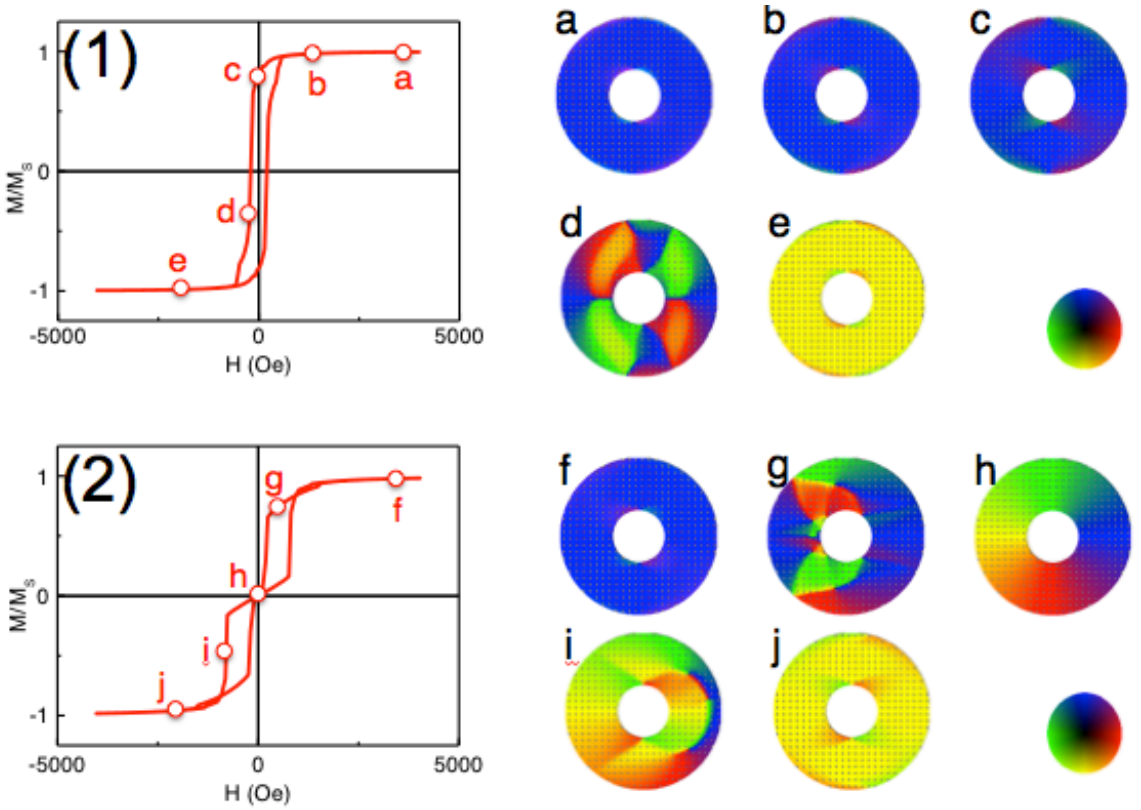

Figure 1.5 Two types of switching modes in the magnetic thin-film ring structure (1) single-step switching with quasi-saturated state formed at remanence, as shown in 1(c); (2) Double step switching with vortex state formed at remanence, as shown in 2(h).

The second type of switching, as shown in Figure 1.5(2), is a double-step switching process. From positive saturation [Figure 1.5(f)], the ferromagnetic ring first switches its magnetization in the left (or, right) half via domain nucleation [Figure 1.5(g)] and forms the flux-closure vortex state [Figure 1.5(h)]. Reversing the field direction in the negative direction can lead to the collapse of the vortex state, and the magnetization of the right half ring also switches via domain nucleation [Figure 1.5(i)], and finally, the ring

saturates in the negative direction [Figure 1.5(j)]. Since the intermediate vortex state is formed at remanence ($H_{ex} = 0$), the hysteresis loop shows a constricted shape.

1.4 Magnetic interactions and critical length scale

The formation of these different magnetic states and switching behaviors is the result of the competitions between different magnetic interactions and energy terms. The three major magnetic energy terms that dominate the magnetization process in the nanometer scale are exchange energy, magnetocrystalline energy, and magnetostatic energy.

Exchange interaction governs the coupling between neighboring spins, which typically spans a length scale on the order of a lattice parameter. Exchange coupling is produced by overlap of electronic orbitals, and therefore is short-ranged. The strength of the exchange interaction is often characterized by the exchange integral J of the material, which has been calculated numerically from first principles for many ferromagnetic materials based on the electron structure. The sign of J also determines if the spins are coupled ferromagnetically ($J > 0$) or antiferromagnetically ($J < 0$).

The magnetocrystalline energy term is a measure of the energy required to change the magnetization axis of an ordered array of spins. The magnetization includes contributions from the spin and orbital moment of the electron. The orbital moment is strongly coupled with the crystal symmetry. The interaction between spin and orbital moment (spin–orbit coupling) can be altered by changing the atomic structure and site symmetry of the material.

The magnetostatic energy comes from the magnetic dipole-dipole interaction in the material. The dipole interaction is long range and tends to minimize the stray field of the system by forming domain structures.

The exchange, magnetocrystalline and magnetostatic energies are of different origins and have different interaction range. The balancing of these interactions creates the characteristic length scales in magnetism. Among them, there is the exchange length:

$$l_{ex} = \sqrt{\frac{2A}{\mu_0 M_S^2}} \tag{1-1}$$

in which A is the exchange stiffness constant of the material,

$$A = \frac{JS^2 c}{a} \tag{1-2}$$

where a is the length of the edge of the unit cell, and where c=1, 2, and 4 for simple-cubic (sc), body-center-cubic (BCC) and face-center cubic (FCC) lattices, respectively. μ_0 is the vacuum permeability and M_s the saturation magnetization of the material. The exchange length reflects the balance of short-range exchange interactions and long-range dipole-dipole interactions. In the size range below the exchange length, exchange interaction is the dominant force to determine the magnetic behavior of an object.

And the dimensionless magnetic hardness parameter

$$\kappa = \sqrt{|K_1|/\mu_0 M_S^2} \tag{1-2}$$

which is the ratio of magnetocrystalline anisotropy to magnetostatic energy.

And the domain wall width:

$$\delta = \pi l_{ex}/\kappa \tag{1-3}$$

Smaller than this size, magnetic multi-domain states with Bloch domain walls are not

going to form.

Expressions for some characteristic magnetic length scales are summarized in Table 1.1, [38] together with their values for a range of magnetic materials.

Table 1.1 Characteristic magnetic length scales (nm)

Length	Expression	Fe	Co	Ni	NiFe	$Fe_{90}Ni_{10}B_{20}$	CoPt	$Nd_2Fe_{14}B$	$SmCo_5$	Sm_2FeN_3	CrO_2	Fe_3O_4	$CoFe_2O_4$
κ	$\sqrt{\lvert K_1 \rvert / \mu_0 M_S^2}$	0.12	0.5	0.1	0.01	0.01	2.47	1.54	4.30	2.13	0.36	0.21	0.84
l_{ex}	$\sqrt{\frac{2A}{\mu_0 M_S^2}}$	4.2	5.8	8.7	5.9	4.3	6.1	3.3	6.2	4.3	7.6	8.5	9.0
δ_w	$\pi l_{ex}/\kappa$	64	24	125	800	900	4.5	3.9	2.6	3.7	44	73	20
R_{sd}	$36\,\kappa\, l_{ex}$	10	56	24	1.6	0.7	310	110	560	190	48	38	160

Here, κ is the hardness parameter; l_{ex} is the exchange length; δ_w is the Bloch domain wall width; R_{sd} is the maximum equilibrium single-domain particle size, which also shows the balance between the exchange interaction and the magnetostatic interaction.

These critical length scales provide good references for the investigation of magnetic domain configuration and switching behavior of the magnetic thin-film nanostructures because they show the approximate length range where the magnetic property of the structure starts to change.

Besides the critical length scale set by fundamental magnetic behavior, to study ferromagnetic nanostructures, different techniques used for lithography and characterization also have their resolution and sensitivity limitations. Figure 1.6 lists some relevant length scales: [39]

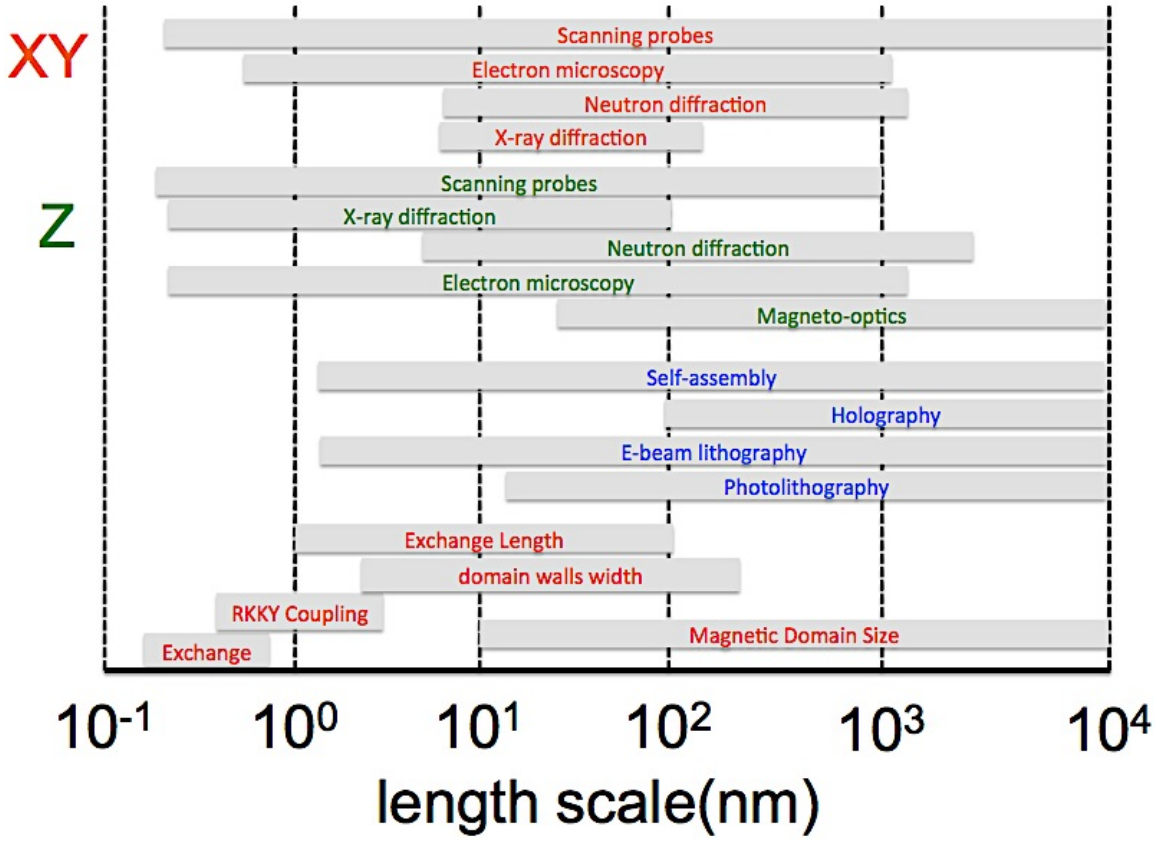

Figure 1.6 Length scales relevant to different magnetic phenomena (red), nanofabrication techniques (blue), tools suitable for probing magnetic structures across the thin dimension of a film (green), those that are applicable to studies of lateral inhomogeneities (orange).

The evolution of the properties of magnetic thin film structures with size is discussed in the following sections.

1.5 Geometric parameters to define a magnetic thin-film ring structure

As discussed in the previous sections, in this thesis, we systematically study the magnetic properties of ferromagnetic ring structures. A lot of work has been done to discuss the relationship of the magnetic behavior of the ferromagnetic ring structure and its physical properties, such as the geometry [40, 41, 42] and materials. [43] As shown in Figure

1.7, there are three geometric parameters that can define the shape of the ring: the lateral size (D_{out}), the center hole size (D_{in}) and the thickness (t_{Fe}).

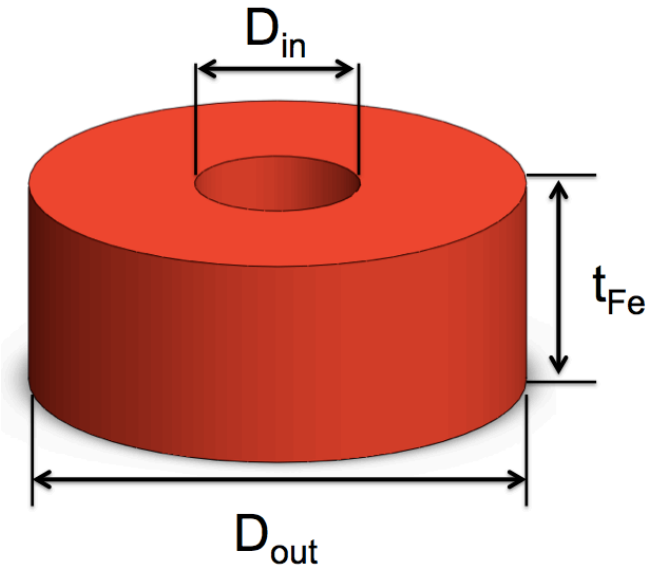

Figure 1.7 Three geometric parameters that define the ring geometry: the outer diameter D_{out}, the inner hole size D_{in} and the thickness t_{Fe}.

In this thesis, we describe the relationship between the physical properties of the ferromagnetic nanorings and their magnetic behavior. We use a series of fabrication, characterization and simulation tools to study the magnetic behavior of the ferromagnetic ring structures (Chapter 2). Then we systematically varied the thickness (Chapter 3), size (Chapter 4), width (Chapter 5) and interface properties (Chapter 6) of the ring and studied their effects on the magnetic properties of the ring structure. A prototype magnetic ring based magnetic tunnel junction (MTJ) device for magnetic random access memory (MRAM) is discussed in the last chapter (Chapter 7).

Chapter 2

NANOFABRICATION, CHARACTERIZATION AND MODELING

In Chapter 2, we discuss the fabrication techniques that are used to produce thin-film ferromagnetic ring structures, including thin film deposition and lithography patterning. A series of characterization methods, such as X-ray diffraction (XRD), magneto-optical Kerr effect (MOKE) and magnetic force microscopy (MFM) that are applied to study the magnetic behaviors of these nanoring patterns is also discussed. Finally, details of the micromagnetic simulation that is used to model and explain these behaviors are presented.

2.1 Growth of magnetic thin-films structures: ion beam sputtering (IBS)

The fabrication of the multilayer nanorings starts with thin film deposition. Thin-film technology is simultaneously one of the oldest arts and one of the newest sciences. The ancient craft of gold beating has been practiced continuously for at least four millennia for durable ornamentation and protection purpose.[44] The modern thin-film technology is universally applied in electronic semiconductor devices and optical coatings. [45]

The act of applying a thin film to a surface is thin film deposition. Depending on the mechanism of the process, typical thin film deposition methods can be classified into chemical deposition and physical deposition. [46] Chemical deposition involves chemical reaction of certain precursors at the substrate surface, which includes plating, chemical vapor deposition (CVD) and atomic layer deposition (ALD). [47] Physical deposition, on

the other hand, transports the material to the substrate via mechanical, electromagnetic and thermodynamic means. [48] Here, in this thesis, the focus is on the physical deposition methods. Physical deposition includes thermal evaporation, sputtering, pulsed laser deposition, cathodic arc deposition and electro-hydrodynamic deposition.

All the thin film and lithographically patterned structure samples discussed in this thesis are grown in the ion beam sputtering (IBS) system in our laboratory. The schematic setup of the IBS system is depicted in Figure 2.1. The system consists of a main sputtering chamber and a small load lock, connected by a vacuum gate. The main sputtering chamber is constantly maintained at a high vacuum of 10^{-8} Torr by the constant pumping of a cryopump located at the bottom of the sputtering chamber operating at 11 K. A water-cooled helium compressor keeps the low temperature of the cryopump. The load lock is designed to help maintaining the vacuum of the main sputtering chamber so that samples can be transferred into/out of the main chamber via a magnetic transporter on the load-lock side and venting only takes place in the small load lock chamber after the vacuum gate is closed.

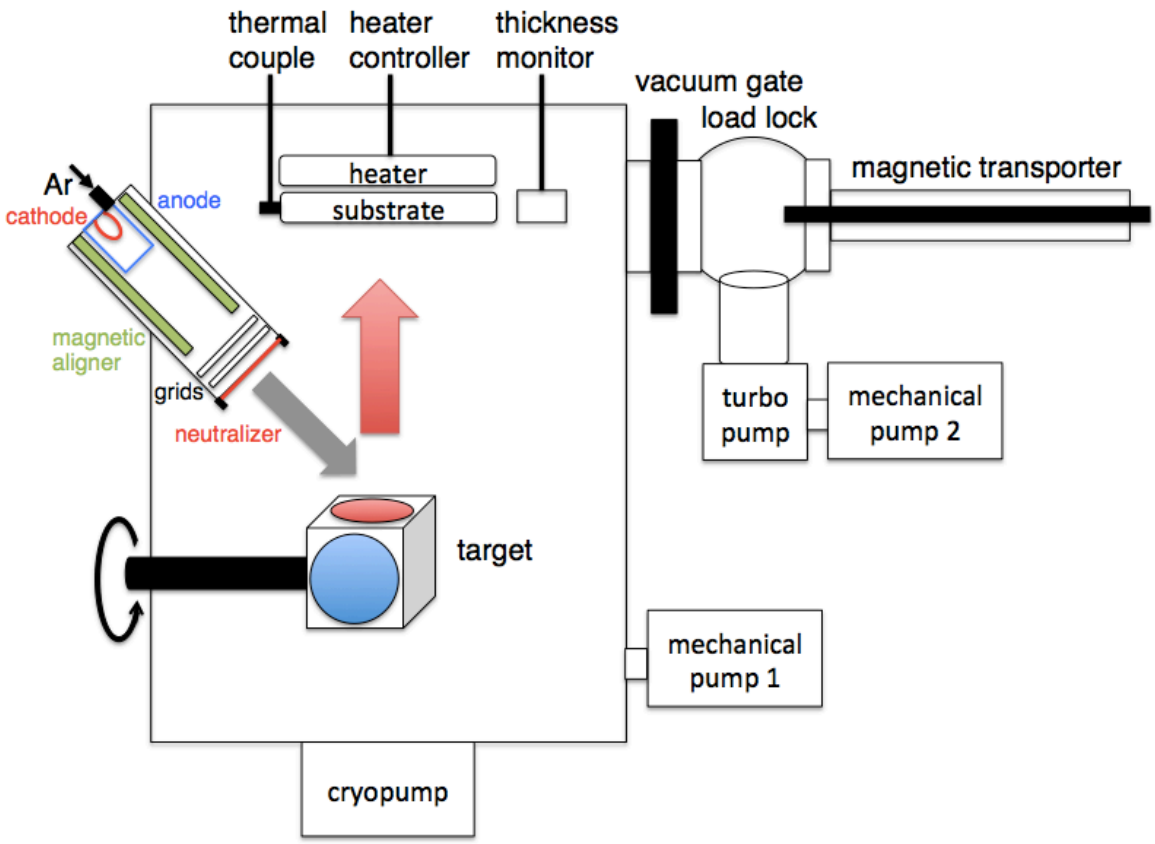

Figure. 2.1 Schematic illustration of the set up of the ion beam sputtering system

1. The IBS system utilizes a Kaufman ion source to generate a relatively high-intensity focused ion beam directed at the target to be sputtered. The ion source consists of a discharge chamber and grids with a common central axis. Applying a high voltage field of 250-1000 V between the anode and cathode inside the discharge chamber creates an electrostatic field inside the ion source, confining electrons around a saddle point in the center of the chamber. When argon gas is injected into the ion source from the back, the high electric field causes the Ar atom to ionize, creating plasma inside the discharge chamber. The ions are then accelerated from the source to the exit grids by the high electrical fields between

the two lenses of the grid. The magnetic field from the magnetic aligner keeps the direction of the ion stream to be along the source axis. When the ions pass through the grids, the apertures focus the beam and create a "collimated" ion beam. As the ions leave the source they are neutralized by electrons from a second external filament called the neutralizer. The resulting neutral atom flux impinges upon a target material, transfers momentum between the ion and the target, to sputter this material onto the sample.

Since the beam is electrically neutral, the IBS system can sputter both conductive and insulating targets. The targets are placed at the focal plane of the ion source. The target holder has a cubic shape and can hold up to 4 different targets at one time. During sputtering, the targets can be switched by rotating the target holder.

The substrate is placed at the ceiling of the main chamber facing downwards. During the thin film growth, the sputtered elements diffuse along the gas pressure gradient from the ion source to the substrate and get deposited. At the back of the sample holder is a vacuum sample heater, which heats the sample in the temperature range of 300 K to 800 K. A thermocouple is mounted at the sample holder to monitor the instantaneous temperature of the sample. Right next to the sample holder is a quartz crystal microbalance (QCM) thickness monitor, which detects the resonant frequency shift of the quartz crystal due to the deposited thin film, and thus calculate the film thickness.

2.2 Patterning of magnetic thin film: photolithography and electron beam lithography

In order to pattern continuous thin films into nanostructures, nanofabrication techniques such as lithography and etching must be applied. For our ferromagnetic ring samples, depending on the lateral size of the sample, two different types of lithography techniques have been used: photolithography and electron beam lithography (EBL).

Photolithography is one of the most commonly used patterning techniques in the semiconductor industry.[49] In photolithography, a substrate, spin-coated with a thin layer of photoresist, is exposed to an ultraviolet (UV) light source through a photomask. The photomask is typically a quartz plate covered with patterned microstructures of an opaque chromium film. The photoresist exposed to the UV light becomes either more (positive tone resist) or less (negative tone resist) soluble in the developer solution. In either case, the pattern on the photomask is thus transferred to the film of photoresist. The patterned photoresist can be subsequently used as a mask for doping or etching of the substrate. [50]

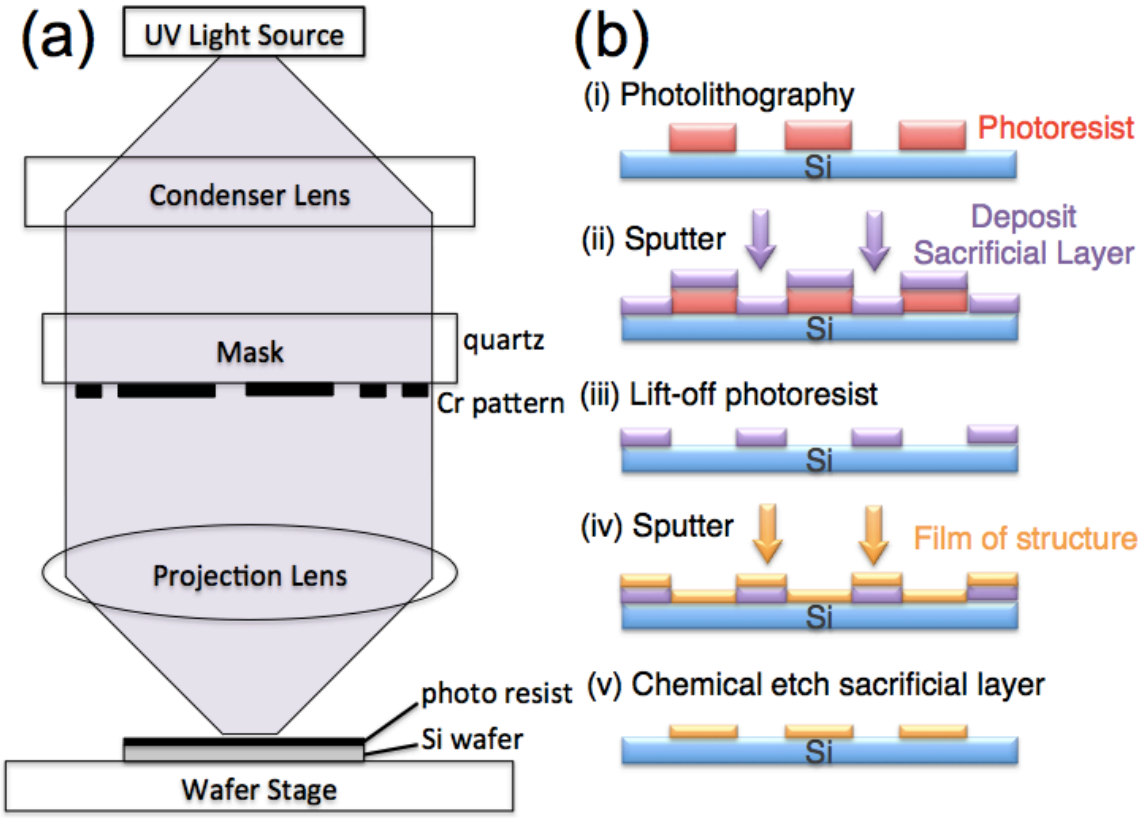

Figure 2.2 (a) illustration of the exposure step in the photolithography that transfers the pattern from the mask to the photoresist layer; (b) illustration of the post-development pattern transfer process that creates the ferromagnetic nanostructures.

Because of the development of the semiconductor industry, the process of photolithography is well developed and implemented with strict standards. For our sample, all the photolithography patterning is carried out inside the Microfabrication Facility's (MFF) class 1000 cleanroom at University of Washington Seattle campus. Class X here means that in each cubic foot of air in the factory, there are less than X total particles greater than 0.5 μm in size.

First, substrates, i.e. Si wafers, are cleaned using chemical baths or plasma procedures in order to remove contaminants that may lead to poor adhesion or defect formation in the resist layer. The cleaning process usually starts with a piranha solution cleaning, as

shown in Figure 2.3(a), which uses a 3:1 mixture of H_2SO_4 and H_2O_2 to decompose the residual resist or other organic contaminations into CO_2 and H_2O. Then the Si wafers are subjected to a three-step standard cleaning procedure, which is invented by Kern and Puotinen at RCA in 1965. In RCA cleaning, the wafers are first immerged in high-pH solution consisting of $5H_2O + 1H_2O_2 + 1NH_4OH$ at 70 – 80 °C for 10 minutes (called SC-1) [Figure 2.3(b)]. This solution oxidizes organic films and removes metal ions on the wafer. The second step is a short immersion in a 1:50 solution of $HF + H_2O$ at 25 °C, in order to remove the thin oxide layer and some fraction of ionic contaminants [Figure 2.3(c)]. The third and last step (called SC-2) is performed with a 1:1:6 solution of $HCl + H_2O_2 + H_2O$ at 75 or 80 °C [Figure 2.3(d)]. This treatment effectively removes the remaining traces of metallic (ionic) contaminants.

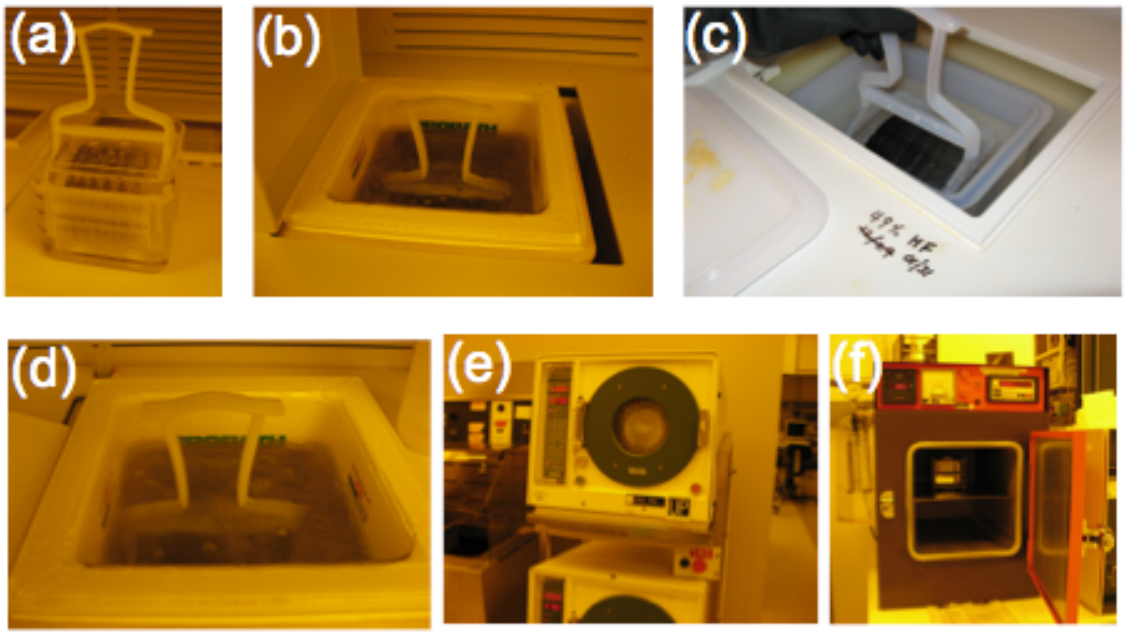

Figure 2.3 Standard procedure of photolithography before applying the photoresist (a) Piranha cleaning (b) SC1 cleaning (c) HF cleaning (d) SC2 cleaning (e) Spin drying (f) HMDS vapor oven baking.

After rinse in DI water and spin dry [Figure 2.3(e)], the surface of the Si wafer is modified by using an adhesion promoter, such as hexamethyldisilazane (HMDS), which enhances the adhesion of the resist to the substrate. The HMDS is introduced as a vapor into a chamber containing wafers and baked for 45 mins to form a monolayer at the Si wafer surface [Figure 2.3(f)].

The photoresist (AZ1512, as an example) is then spin coated onto the Si wafer surface at 4000 rpm, forming a thin uniform resist layer 1.2 μm thick. After the spin coating, the next step is the prebake. The coated Si wafer is placed on the hot plate and baked at 90°C for 30 minutes. The prebake step further evaporates the remaining solvent in the resist from 25% down to 5% of the resist content. It also improves the adhesion of the resist since the heating strengthens the bonds between resist/HDMS and Si wafer. Finally, it helps to relieve the stresses present in the resist as a result of the spinning process through thermal relaxation.

The exposure is performed in the EVG 610 semi-automated mask alignment system, with an UV light source of 450 nm wavelength and power of 500 W for 3.3 seconds. The exposure energy dose is 23 mJ/cm^2, which may vary significantly for different patterns. The experimental exposure process is shown in Figure 2.4.

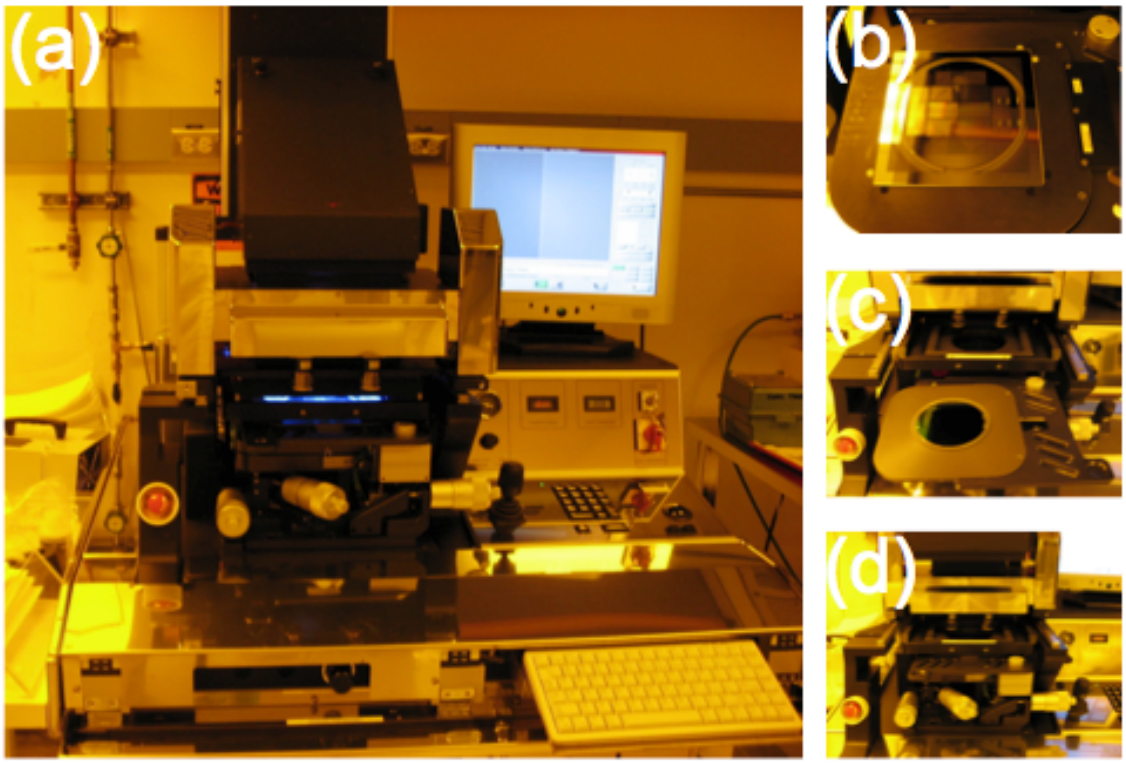

Figure 2.4 (a) The Si wafer coated with resist is exposed to UV light on a EVG 610 aligner; (b) the photomask is held in between the UV light source and the wafer; (b) the wafer is applied close to the mask by vacuum; (d) the position of the mask and the wafer can be precisely tuned by the optical system of the aligner.

After the exposure, the Si wafer is baked again in a step called post-exposure bake (PEB) at 100 °C for 10 minutes. At elevated temperature, the exposed area can diffuse and smear out the wavy shape edges caused by the standing wave along the edge of the resist features.

The final step is the development. The AZ1512 pattern is developed in the 3:1 AZ312 MIF developer: H_2O solution for 60 seconds. It can either be developed manually by immersing the wafer in the solution [Figure 2.5(a)], or it can be developed using the pre-programed spin developer [Figure 2.5 (b)]. The developed feature is rinsed in deionized water for 3 cycles and dried in the spin drier.

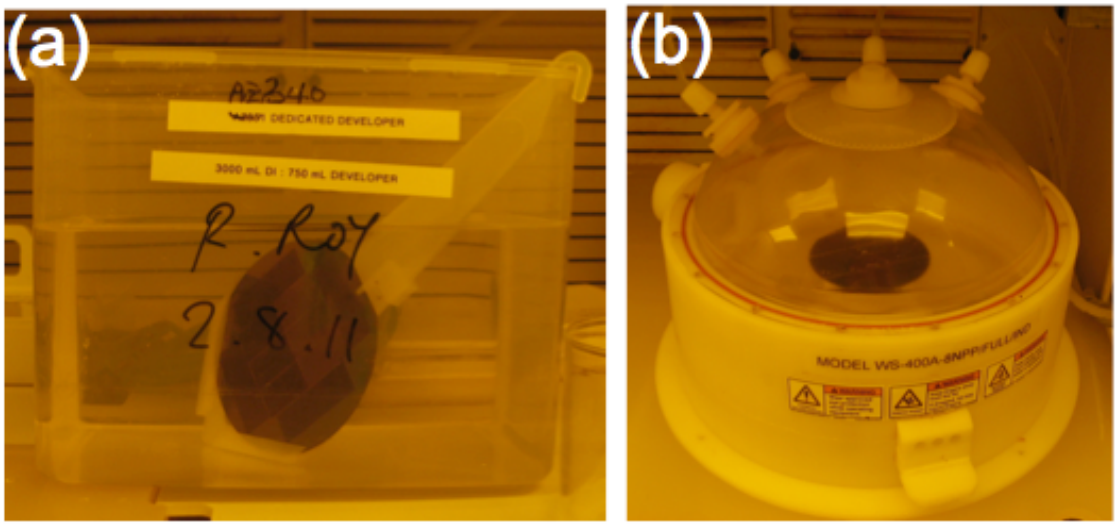

Figure 2.5 Development (a) manually (b) by a pre-programed vacuum spin developer.

The developed photoresist ring-shape pattern of the same photomask is shown in Figure 2.6. Figure 2.6(a) shows the ring shape resist posts created by positive-tone photoresist AZ1512. Figure 2.6(b) shows the ring-shape holes created by negative-tone photoresist NR7-1000PY from the same mask. The two features are just opposite to each other.

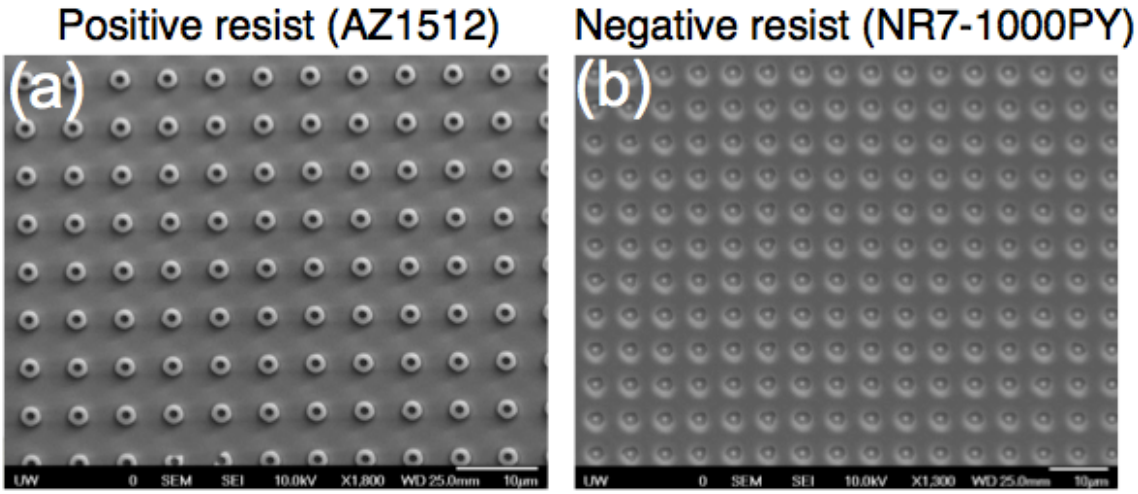

Figure 2.6 Photolithography patterned resist layer of (a) positive-tone resist AZ-1512, showing 2.4 µm diameter ring-shape posts; (b) negative-tone resist NR7-1000PY, showing ring-shape holes of the same size.

Although photolithography has many advantages such as high throughput, its resolution is severely limited by the wavelength of the UV light source used for exposure. Since electron beam has smaller wavelength and a well-controlled probe size, electron beam lithography (EBL) can provide excellent resolution for features in the nanometer scale. However, since the writing process of the feature is done point by point, the throughput of the EBL is very low compared to parallel patterning methods such as photolithography.

In electron beam lithography, material sensitive to the electrons, such as poly (methyl methacrylate) (PMMA), is used as the resist. PMMA can differ in its molecular weight (495K or 950K) in either anisole or chlorobenze. For our samples, we use PMMA 950 A3 resist, with molecular weight of 950K, diluted in 3 % anisole (A3). The PMMA resist is spin coated on 4-inch Si wafer at 3000 rpm for 45 s to form a uniform thin film of 100 nm thickness. The resist is soft baked on hot plate at 180 °C for 90 s. The writing is carried out at University of Washington Nano Tech User Facility's (NTUF) FEI XL-30 scanning electron microscope. The 30 keV electron beam is first tuned by focusing the beam within the smallest beam size on a gold nanoparticles calibration standard at ×100,000 magnification. Then this optimized beam is moved onto the PMMA coated substrate for writing patterns in a point-by-point process under the control of the NPGS software and the E-beam writter. The EBL setting is schematically displayed in Figure 2.7.

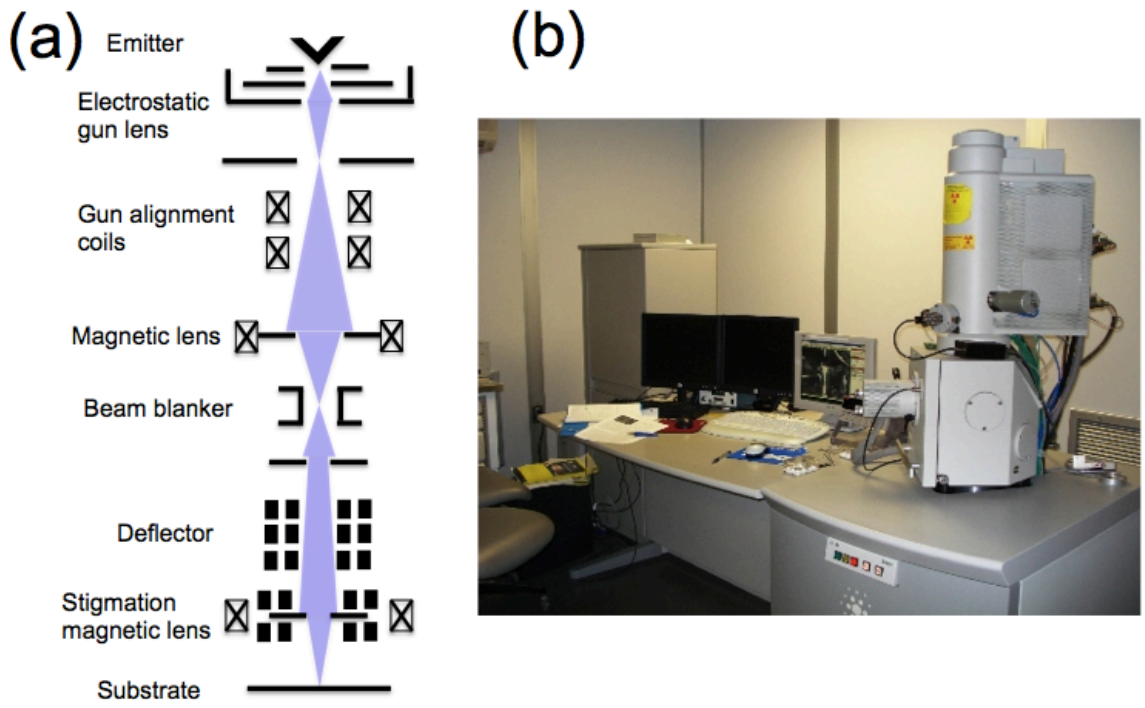

Figure 2.7 (a) Schematic illustration of the electron beam lithography. Electron beam from the emitter are focus precisely in a small spot on the resist layer at the bottom. (b) FEI XL-30 SEM.

The typical exposure dosage for the PMMA layer is between 50 ~ 500 μC/cm^2, however, the dosage of a specific pattern is usually determined by a dosage test in advance.

After writing, the pattern is immersed into the 1:3 MIBK to IPA developer for 70 s and rinsed in IPA solution and blow dry with nitrogen gas.

Magnetic thin films are then sputtered onto the EBL pattern in the ion-beam sputtering chamber. Then the sample is immerged in acetone solution for 24 hours before a 15 s ultrasonic lift-off. The finished sample is shown is Figure 2.8.

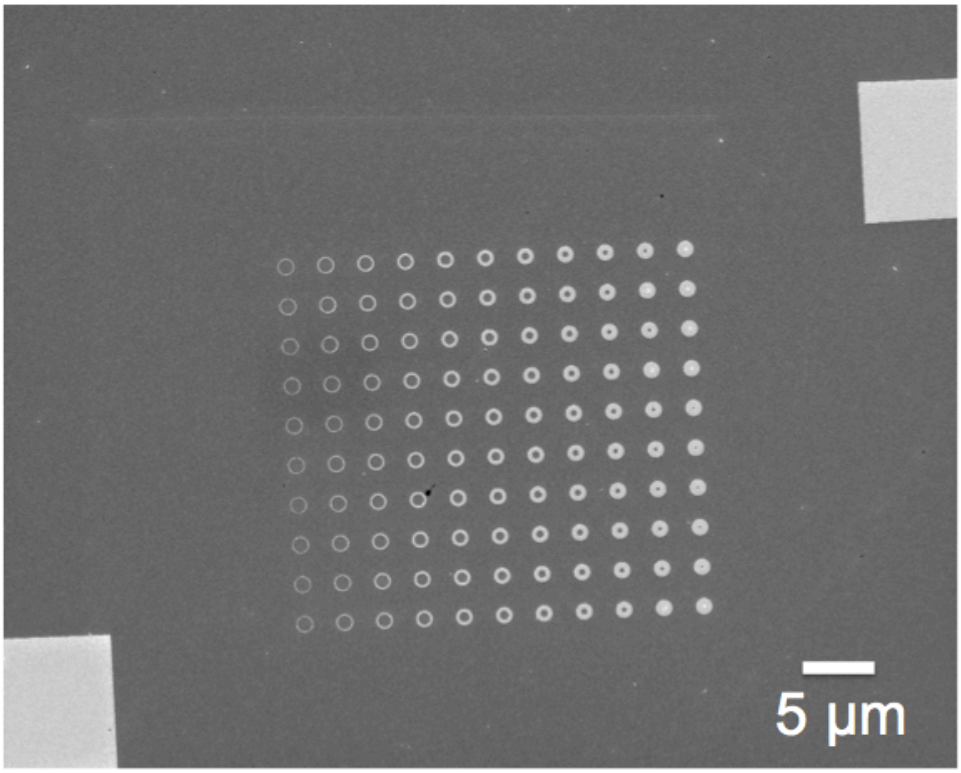

Figure 2.8 In-plane view of EBL patterned 1 µm ring structures with changing D_{in} / D_{out} ratio

2.3 Structural characterization of magnetic thin film: X-ray Diffraction

X-ray diffraction (XRD) is the primary means for determining the crystal structure of bulk materials, and this technique can also be applied to thin films. In addition, the x-ray reflectivity (XRR) technique can be used on thin film materials for extracting information on the layer thickness and free surface and interface roughness. Here, a background on the theory and experiment is presented as a brief overview of the technique. More information about XRD and XRR can be found in published texts. [51, 52,53]

X-rays are electromagnetic radiation generated by either x-ray tubes or synchrotron radiation. In a x-ray tube, which is the primary x-ray source used in laboratory x-ray instruments, x-rays are generated when a focused electron beam is accelerated across a high voltage field to bombards a stationary or rotating solid target. For our Rigaku XRD system, a rotating Cu target is used. When the high-speed electron beam hits the Cu target, it knocks out electrons in an inner shell, normally K shell, and generate a hole. The hole in the K shell is filled by an electron from an outer shell, normally L shell. The energy difference between L and K shells is released as a characteristic x-ray quantum. Common targets used in x-rays tubes include Cu and Mo, which emit 8 keV and 14 keV x-rays with corresponding wavelength of 1.54 Å and 0.8 Å, respectively. Since the wavelength of x-rays is comparable to the inter-atomic distance in crystals, it is ideally suited for probing the structural arrangement of atoms and molecules in a wide range of materials.

In XRD, incident x-rays on a sample are scattered by parallel planes of atoms, where each plane reflects 10^{-5} to 10^{-3} of the incident radiation, depending on the scattering power. Diffraction effects are observed when the distance between the sources (plane of atoms) is comparable to the wavelength of the incident x-rays. The diffracted radiation has a strong angular dependence because it is produced by constructive and destructive interference. Constructive interference occurs when the phases of the scattered waves from atoms in parallel planes differ by an integer number of wavelengths, and a peak in the diffraction pattern is formed. Destructive interference results in low intensity in the diffraction pattern.

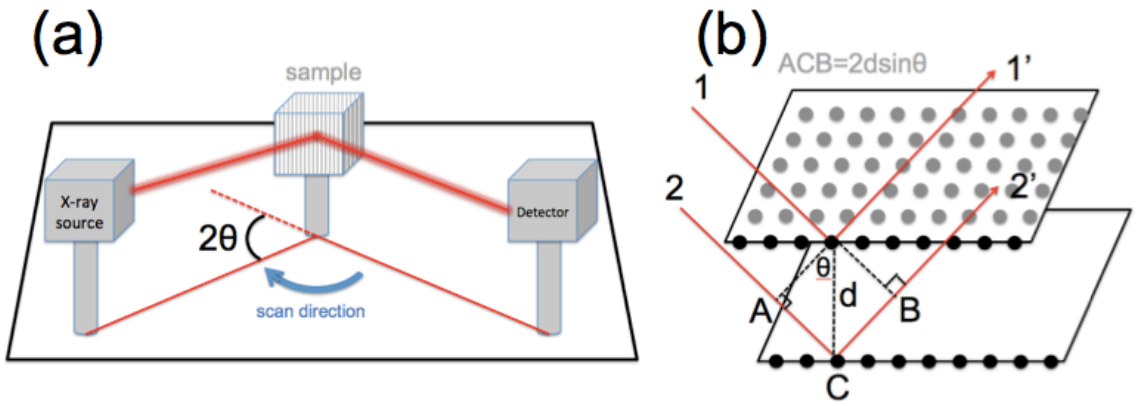

Figure 2.9 XRD θ – 2θ scan geometry and the Bragg's law. 1(1') and 2(2') are two parallel incident beams.

The position and intensities of the peaks are used to identify the underlying structure or phase of the material. For a given set of lattice planes with an inter-plane distance of *d*, the condition for a diffraction peak to occur can be simply written as

$$n\lambda = 2dsin\theta \tag{2.3.1}$$

also known as *Bragg's law*, in which *n* is the order of wavelength. λ is the wavelength of incident beam, which is 1.54 Å for Cu target. *d* is spacing between planes in the atomic lattice. θ is angle of incident beam. Figure 2.9(a) illustrated the set-up of conventional XRD in this *Bragg-Brentano* geometry. The detector is always at the angle of 2θ with respect to the incident beam, which gives the conventional XRD name of θ-2θ scan.

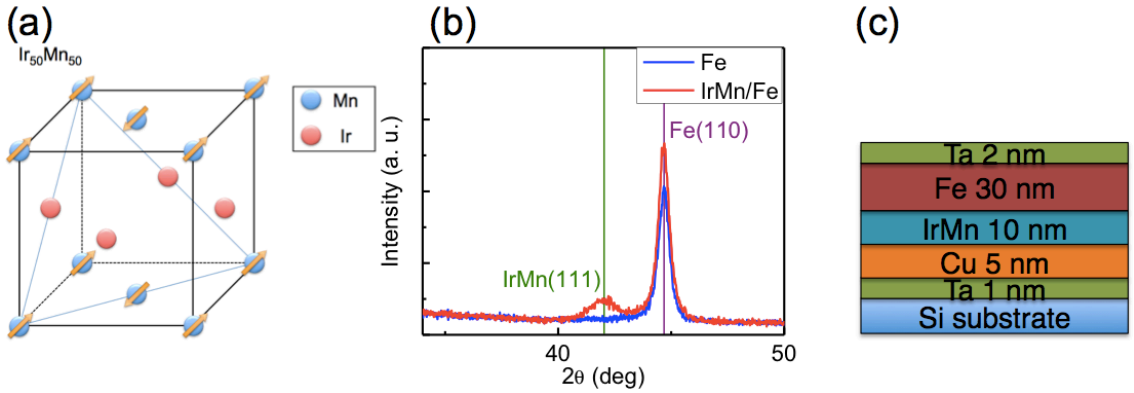

Figure 2.10 (a) Structure of the face-center-cubic $Ir_{50}Mn_{50}$ unit cell, (111) plane is uncompensated. (b) X-ray diffraction of the Ta(1 nm)/Cu(5 nm)/IrMn(10 nm)/Fe(30 nm)/Ta(2 nm) multilayer, and the Ta(1 nm)/Cu(5 nm)/Fe(30 nm)/Ta(2 nm) reference sample. The IrMn has a (111) texture.(c) Structure of the exchange-biased multilayer.

Figure 2.10 shows the θ-2θ scan result of a Ta (1nm)/Cu (5 nm)/IrMn (10 nm)/Fe (30 nm)/Ta (2 nm) exchange biased multilayer. Compared with the reference sample, Ta (1nm)/Cu (5 nm)/Fe (30 nm)/Ta (2 nm), we can see that the IrMn layer has a (111) texture. Figure 2.10(a) shows the spin configuration of the IrMn (111) surface, which is uncompensated and induces the exchange bias interfacial coupling in IrMn/Fe.

The scattering geometry of XRR is the same as the conventional XRD, except that the x-rays strike the thin film surface at very small glancing angle, typically less than 5 degree. As a comparison, XRR is dependent on the interference of the reflected x-rays at different interfaces, due to different electron densities between different layers, while XRD is dependent on the interference of the diffracted x-rays from periodic lattice points in planes of the crystal. XRR still satisfy the Bragg's Law $n\lambda = 2dsin\theta$, but now d is the thickness of the thin film or superlattice.

XRR takes advantage of this effect by measuring the intensity of x-rays reflected from a surface as a function of the incident angle to provide information on the thickness, roughness and density of thin films on a surface, as shown in Figure 2.11 (a).[53] The intensity scattered by a sample is proportional to the square of modulus of the Fourier transform of the electron density. Thus the electron density profile can be deduced from the measured intensity pattern, and subsequently the vertical properties (layer thickness) and the lateral properties (interface roughness) characterizing multilayers can be determined.

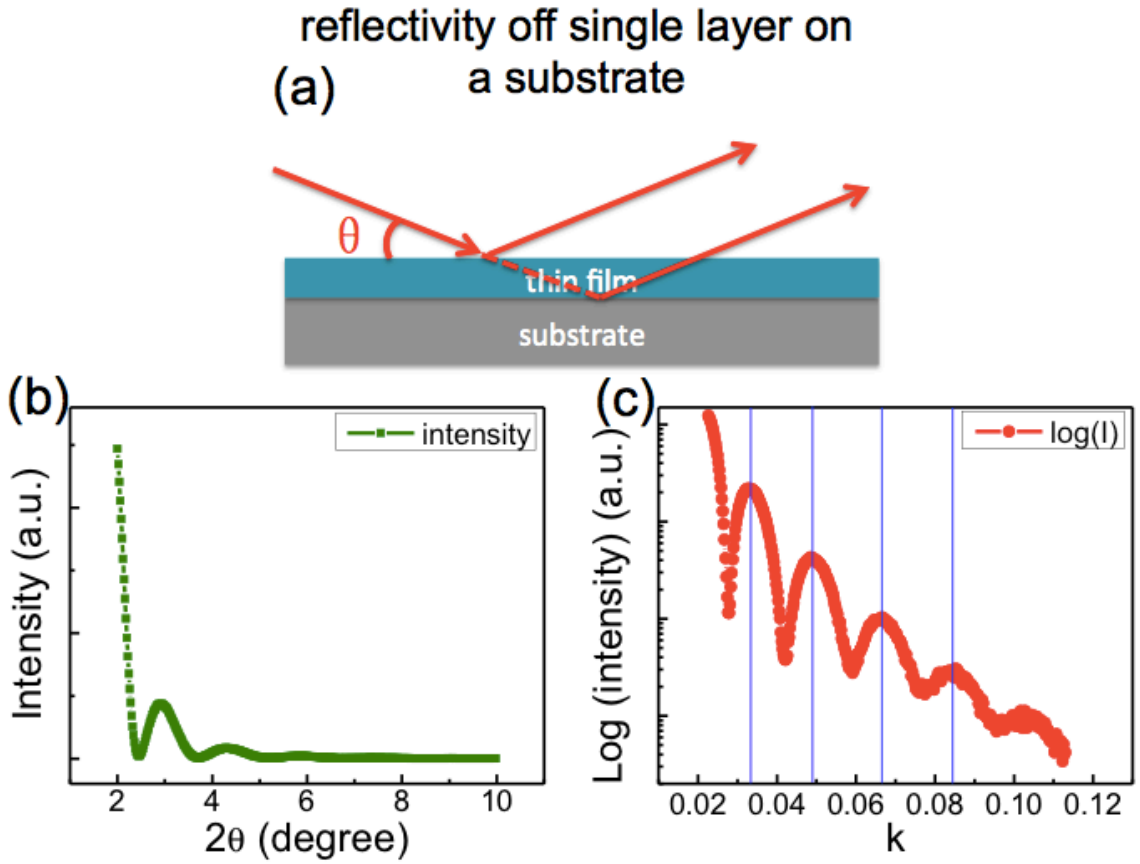

Figure 2.11 (a) XRR geometry. (b) XRR intensity plot with respect to *2θ*. (3) Log of intensity plot with respect to *k*.

For example, the XRR of a single Au layers on Si substrate, shown in Figure 2.11(b) can be used to calculate the Au film thickness. Here Figure 2.11(b) shows the original XRR data of the intensity plotted with respect to 2θ. Then we change the plot from I-2θ (Figure 2.11(b)) to I-k plot (Figure 2.11(c)):

$$k = 2\sin(\theta)/\lambda \tag{2.3.2}$$

where λ is 1.54 Å. We choose two peaks next to each other from I-k, measure distance of the two peaks in x axis as *d*. The film thickness *t=1/d*.

For *2n* continuous peaks in the I-k curve, average of the peak-to-peak distance is

$$d = \frac{1}{n^2}\left(\sum_{n+1}^{2n} k_i - \sum_{1}^{n} k_i\right) \tag{2.3.3}$$

For the film shown in Figure 2.11, *d*=0.0172 $Å^{-1}$. The film thickness *t* =58.2 Å.

2.4 Characterization: magneto-optical Kerr effect (MOKE)

The magneto-optical Kerr effect (MOKE) or surface magneto-optical Kerr effect (SMOKE) is a magneto-optical effect discovered by John Kerr in 1877 that can be used to measure the magnetic properties of thin films or surface magnetic properties. A linearly polarized light becomes elliptically polarized upon reflection from a surface of finite magnetization and its polarization axis also rotates in this process. [54, 55] The rotation of polarization is known to be proportional to the magnetization of the sample surface, so the magnetization of the sample can be detected by measuring the Kerr rotation.

In our experimental MOKE setup, a He-Ne laser beam with wavelength of 633 nm is used as the light source. One set of electromagnets is used to generate the magnetic field, between ±2000 Oe. Linearly polarized laser is first generated by a polarizer before shooting onto the magnetic sample surface. Polarization axis rotation of the reflected light is detected by a second polarizer (analyzer) and a photodiode detector with a lock-in amplifier. Our MOKE system is equipped with a 360-degree rotation sample stage so that the magnetic field can be applied at any arbitrary direction in the sample surface plane.

Depending on the direction of the magnetization vector with respect to the reflecting surface and the plane of incidence, MOKE can be categorized into 3 different modes, i.e., polar, longitudinal, and transverse. Polar mode measures the magnetization component perpendicular to the sample plane. It is often used for samples with perpendicular magnetic anisotropy such as Co/Pt multilayers, or thin film with L_{10} symmetry, such as FePt.

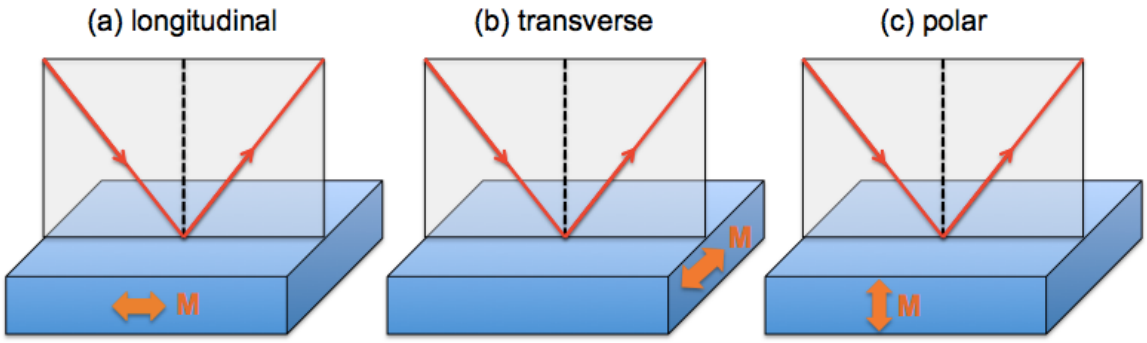

Figure 2.12 Illustration of three different modes of MOKE (a) longitudinal (b) transverse (c) polar. The longitudinal mode measures the *M* component in the sample plane and parallel to the light beam plane; the transverse mode measures the *M* component in the sample plane but perpendicular to the light beam plane; the polar mode measures the *M* component perpendicular to the sample plane.

Longitudinal mode measures the magnetization component in the sample plane and

parallel to the light beam plane. Transverse mode measures the component in the sample plane but perpendicular to the light beam plane. These two modes are widely applied in most thin film samples as the magnetization normally lies in the plane due to the shape anisotropy. With the three different measuring modes, MOKE measurement provides a convenient way to map the 3D magnetization of a sample.

In this thesis, MOKE is used to detect the magnetic hysteresis behavior of lithographically patterned magnetic nanostructures. Compared to continuous film samples, the ratio of surface covered by magnetic material is significantly smaller in these patterns, which gives a weak and noisy signal. To obtain a stable signal from the sample, the hysteresis loop is averaged over multiple times, as shown in Figure 2.13.

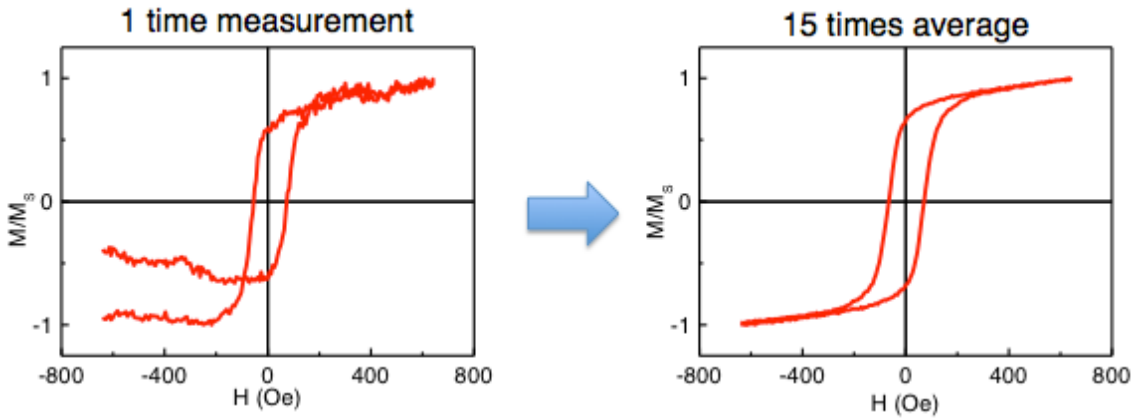

Figure 2.13 Single time measured and 15 times averaged MOKE hysteresis loop of the D_{out}=*2.4 μm*, t_{Fe}=*10 nm* ring structure.

A typical hysteresis loop measured by MOKE is plotted with the Kerr signal (Kerr rotation) as a function of the applied magnetic field. However, the magnitude of this signal is not the magnetization itself but proportional to the magnetization by a factor. For the absolute quantitative determination of magnetization, a vibrating sample

magnetometer (VSM) measurement is required.

2.5 Magnetic characterization: magnetic force microscopy (MFM)

Scanning probe microscopy (SPM) is a class of microscopies that obtains images of a surface by using physical probes that scan the specimen surface.

Figure 2.14 is a schematic diagram showing the major components of a typical scanning probe microscope. A cantilever supporting a very fine tip with a typical end radius of several nanometers is used as a probe to investigate the surface properties of a sample by scanning over it. The cantilever is held by a piezoelectric transducer (PZT). Columnized light from a super-luminescent diode (SLD) is reflected from the back of the cantilever onto a position sensitive quadrant photocell. As the cantilever and tip are scanned over the sample surface, the cantilever bends and the light beam reflected is deviated by the bending, hence its position on the quadrant photocell changes. The signals from the photocell are used as input to a servo system that controls the PZT moving the cantilever to maintain a constant bending of the cantilever and thus return the reflected beam's point of incidence on the quadrant photocell to the center. This ensures that the force exerted by the tip on the surface remains constant and that the tip follows the surface topography. A measure of changes in the servo signal gives an indication of the surface topography.

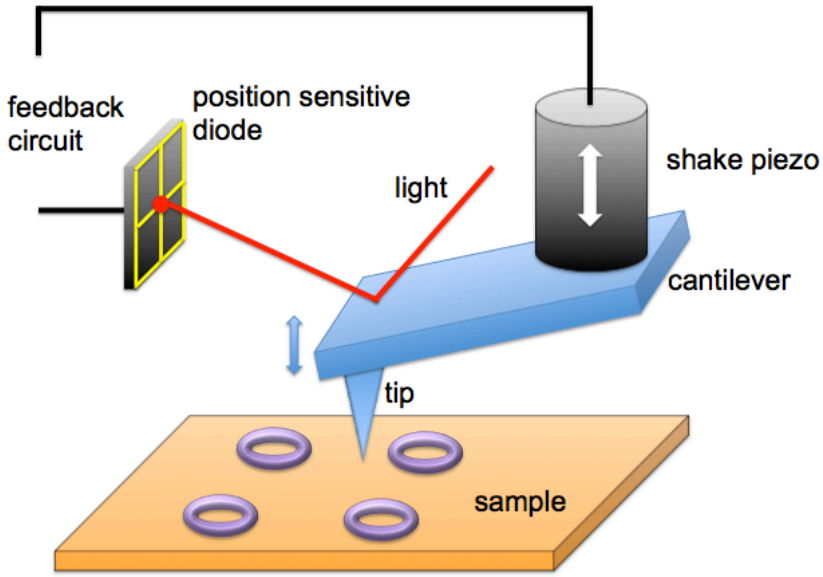

Figure. 2.14 Schematic illustration of the feedback-control system of the MFP-3D AFM

There are two basic operating modes of the SPM, the first is the static or contact mode, in which the probe is in direct contact with the sample surface during the scan. The other mode is the dynamic or tapping mode, in which the cantilever oscillates above the surface during the scan. If the tip is far from the surface, the magnitude of the vibration is its free air magnitude. However, as the tip approaches the surface, it starts to feel the force from the surface acting on it, which can be either attractive or repulsive, depending on the distance. The vibration magnitude changes from the free air value. If we can control the servo to maintain the vibration magnitude of the tip at a certain setting value, the distance between the tip and the surface is fixed. In the tapping mode, by carefully maintaining the vibration magnitude of the tip, we maintain a constant distance between the tip and the sample during the scanning and obtain the surface morphology, as shown in Figure 2.15.

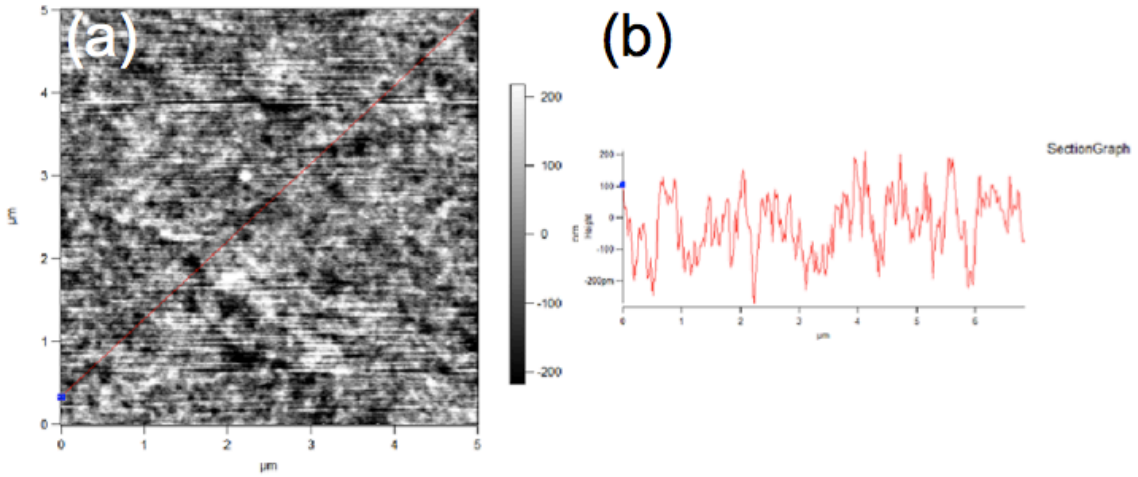

Figure 2.15 (a) AFM image of the surface topography of 30 nm thick Fe film (b) the variation in the *z* direction along the marked diagonal line in (a), showing the roughness is smaller than 0.2 nm.

In magnetic force microscopy (MFM), the tip is coated with a thin layer of magnetic material such as Co and CoPtCr. To isolate the magnetic signal of the sample surface from other signals, the tip scans over the surface of the sample twice, which is call "lift-mode" or "nap mode". Compared to other tip-surface interactions such as van der Waals and capillary wetting interactions, magnetic interaction is long range and falls off much more slowly and can be detected when the tip is lifted up at certain distance (delta height, which varies from sample to sample). Therefore, the key of the MFM is to separate the short range topographical interactions from the long rang magnetic interactions by scanning the tip over the sample surface at different height for two separate times.

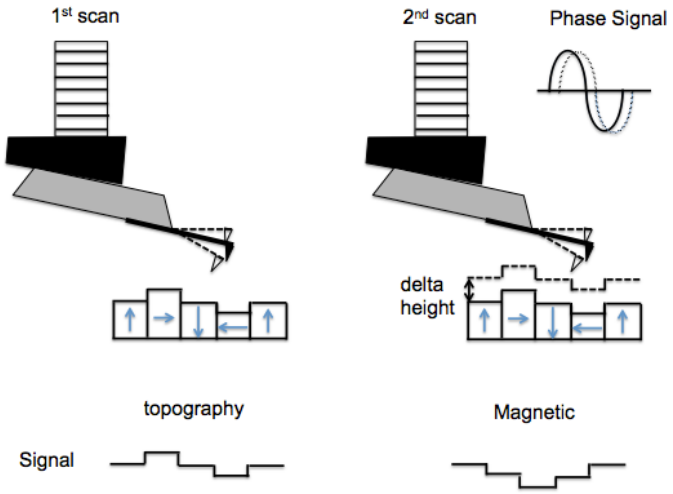

Figure 2.16 Schematic illustration of the nap mode MFM: the tip scans the surface twice, first time scans the topography, second time the tip is lifted up to detect the phase shift caused by the magnetic interaction.

As shown in Figure 2.16, in MFM, the tip first scans over the sample surface in normal tapping mode, which collects the short-range interactions and obtains the topography information of the sample surface. Then, the tip is lifted up from the sample surface by the PZT for several nanometers (called the delta height) and scans following the previous path again. This time it follows the topography template it records from previous scan in the z direction and thus the tip-surface distance is maintained as a constant. Since the second path is far away from the surface, the short-range interactions are diminished, while the long-range magnetic interaction dominates the signal and can be detected by the magnetized tip.

Since the MFM tip can be viewed as a small magnetic dipole, the MFM measures the gradient of the magnetic field in the perpendicular direction normal to the surface. As the tip scan over the sample surface, wherever it encounters a non-uniform stray field, a force

is exerted on the tip:

$$\vec{F} = \mu_0(\vec{m} \cdot \nabla)\vec{H} \tag{2.5.1}$$

where $\vec{m}$ is the magnetic moment of the tip (approximately as point dipole), $\vec{H}$ the magnetic stray field from the sample surface, and μ_0 the magnetic permeability of free space.

Figure 2.17 showed the MFM domain image of the 2 micron wide wires and dots.

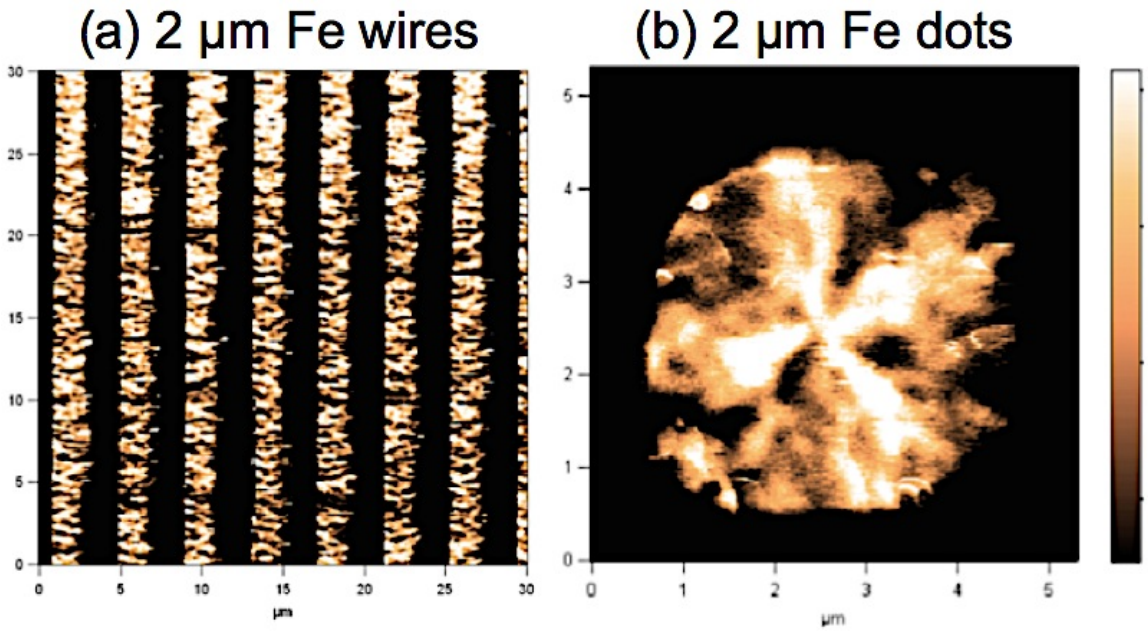

Figure 2.17 MFM domain image of (a) 2 micron wide Fe wires (b) 2 micron sized Fe dots. Both of them are broken into multi-domain state.

Since the MFM uses a magnetized tip to detect the magnetic signal from the sample, its spatial resolution is limited by the tip diameter. Most of the MFM tips are fabricated by sputtering a magnetic film (such as CoCr or CoPt) onto the regular AFM tips. For the Olympus TM MFM tips

we use in our lab, the AFM tip has a tip diameter of 28 nm. [56] Low-moment MFM tip is coated with a 15 nm CoCr layer and thus has a total size of 40 nm. [56] High-moment MFM tip is coated with a 100 nm CoCr layer and thus has a total size of 168 nm. [56] The high-coercivity MFM tip is coated with a 45 nm CoPt/FePt layer and thus has a total size of 86 nm. [56]

2.6 Magnetic modeling: LLG micromagnetic simulation

Micromagnetic simulation is a very powerful tool to calculate the magnetic domain configuration and magnetic reversal process in the micron and nanometer scale. However, the simulation itself is nothing more than solving for the magnetization, *M,* as a function of position (x,y) with static energy minimum or the dynamic LLG differential equation with initial state and boundary conditions. In this section, we discuss the working principle of the micromagnetic simulation.

(i) Continuum hypothesis

Micromagnetic modeling can be applied to magnetic phenomena over a wide spatial scale: from a few nanometers to a few microns. [57, 58] In this size range, there exists both short-range interaction such as exchange interaction among magnetic moments, and long-range interactions like magnetostatic dipole-dipole interaction. The magnetic structure of a given material depends on the detailed balance between these interactions. As it is not possible to add the magnetostatic and anisotropy term as a perturbation to the exchange energy term and use a quantum mechanical solution of this problem, [59] currently the only

realistic approach is to ignore the atomic nature of matter, to neglect quantum effects, and to use classical physics in a continuum description of a magnetic material. [58, 59]

Essentially, we assume the magnetization to be a continuous vector field $M(\vec{r})$, with $\vec{\boldsymbol{r}}$ the position vector inside the material. Thus we can write:

$$\vec{M}(\vec{r}) = M_s \vec{m}(\vec{r}) \tag{2.6.1}$$

$$\vec{m} \cdot \vec{m} = 1 \tag{2.6.2}$$

where M_s is the saturation magnetization of the material. The basic micromagnetic approach is to formulate the energy in terms of a continuous magnetization vector field and to minimize this energy in order to determine static magnetic configurations. The energy terms are formulated as follows.

(1) Exchange energy

To evaluate the exchange term in energy, we use a microscopic model. The exchange interaction is essentially short ranged and exists between nearest neighbors. We write for the exchange energy of two nearest-neighbor spins as:

$$W_{ij} = -2J\vec{S}_1 \cdot \vec{S}_2 \tag{2.6.3}$$

where J is the exchange integral and $S_i\hbar$ is the spin angular momentum of spin i. We assume that the angle θ_{ij} between spins S_i and S_j is very small. Then

$$\overrightarrow{S_i} \cdot \overrightarrow{S_j} = S^2 cos\theta_{ij} = S^2\left[1 - \tfrac{1}{2}\theta_{ij}^2\right] = S^2\left\{1 - \tfrac{1}{2}\left|\vec{m}_i - \vec{m}_j\right|^2\right\} \tag{2.6.4}$$

where $\vec{m}_i$ is the unit vector along $-\vec{S_i}$ and therefore along the associated magnetic moment, and where $S = \left|\vec{S}_i\right| = \left|\vec{S}_j\right|$. In the continuum hypothesis, we assumed that $\vec{m}_i$ may be approximated sufficiently with a continuous function $\vec{m}(r)$ of position:

$$\vec{m} = \alpha\hat{i} + \beta\hat{j} + \gamma\hat{k} \tag{2.6.5}$$

If $\vec{s_i}$ is the position vector of spin *j* with respect to spin *i*,

$$\left|\vec{m}_i - \vec{m}_j\right| = \left|\left(\vec{s}_j \cdot \nabla\right)\vec{m}_i\right| \tag{2.6.6}$$

The excess exchange energy due to the nonparallelism of $\vec{S_i}$ and $\vec{S_j}$ is

$$W_{ij} = JS^2\left|\vec{m}_i - \vec{m}_j\right|^2 = JS^2\left[\left(\vec{s}_j \cdot \nabla\right)\vec{m}_i\right]^2 \tag{2.6.7}$$

If there are *n* spins per unit volume, the density of the excess exchange energy w_e is:

$$w_e = \frac{1}{2}nJS^2\sum_{\vec{s}_j}\left[\left(\vec{s}_j \cdot \nabla\right)\vec{m}_i\right]^2 \tag{2.6.8}$$

where the sum is over nearest neighbors.

For cubic crystal, this gives:

$$w_e = \frac{1}{2}C\left(\nabla\vec{m}\right)^2 \tag{2.6.9}$$

with

$$C = \frac{1}{3}nJS^2\sum_j s_j^2 = \frac{2JS^2c}{a} \tag{2.6.10}$$

where *a* is the length of the edge of the unit cell, and where *c=1, 2* and *4* for simple-cubic (sc), body-center-cubic (BCC) and face-center cubic (FCC) lattices, respectively.

For a hexagonal crystal,

$$w_e = \frac{1}{2}\left\{C_1\left[\left(\frac{\partial \vec{m}}{\partial x}\right)^2 + \left(\frac{\partial \vec{m}}{\partial y}\right)^2\right] + C_2\left(\frac{\partial \vec{m}}{\partial z}\right)^2\right\} \tag{2.6.11}$$

with

$$C_1 = \frac{1}{2} nJS^2 \sum_j \rho_j^2 , \tag{2.6.12}$$

$$C_2 = nJS^2 \sum_j z_j^2 , \tag{2.6.13}$$

ρ_j is the projection of s_j in the basal plane, and z_j is its projection along the hexagonal axis. For ideal close packing, as in cobalt, this reduces to

$$C = 4nJS^2a^2 = 4\sqrt{2}JS^2 / a \tag{2.6.14}$$

and *a* is the distance between nearest neighbors.

This is the energy density due to exchange interaction. For a defined magnetic object, the exchange energy term is an integrated over the whole body:

$$E_{exch} = \int_V w_e \, dV \tag{2.6.15}$$

$$w_e = A\left(\nabla \vec{m}\right)^2 \tag{2.6.16}$$

where

$$(\nabla \vec{m})^2 = (\nabla \alpha)^2 + (\nabla \beta)^2 + (\nabla \gamma)^2 \tag{2.6.17}$$

and $A = \frac{JS^2 c}{a}$ (2.6.18)

is the exchange-stiffness constant.

(2) Magnetocrystalline anisotropy energy

To evaluate the magnetocrystalline anisotropy energy term, we use phenomenological methods. We assume a power series in α, β, and γ, use the crystal symmetry to decrease the number of coefficients, and truncate the series after the first two nonconstant terms. This gives for cubic crystals an anisotropy energy density

$$w_a = K_1\left(\alpha^2\beta^2 + \beta^2\gamma^2 + \gamma^2\alpha^2\right) + K_2\alpha^2\beta^2\gamma^2 , \tag{2.6.19}$$

where the cubic axes are chosen as coordinate axes. α, β, and γ *are the directional cosines of vector M with respect to the three principle axes.* For hexagonal crystals:

$$w_a = K_1\left(1-\gamma^2\right) + K_2\left(1-\gamma^2\right)^2 , \tag{2.6.20}$$

where the hexagonal axis is chosen as the z axis. The constants K_i are functions of temperature.

For a magnetic object with well-defined shape, the magnetocrystalline energy term is an integral over the whole body:

$$E_{anis} = \int_V w_a \, dV \tag{2.6.21}$$

(3) Magnetostatic energy

For the magnetostatic energy term, we consider only the magnetostatic field arising from the magnetization distribution itself and not any externally applied field (that is calculated in the Zeeman energy term). The magnetostatic or demagnetizing field H_d is governed by [60]

$$\nabla \times \vec{H}_d = 0 \tag{2.6.22}$$

$$\nabla \cdot \vec{B} = \nabla \cdot \left(\vec{H}_d + \vec{M} \right) = 0 \tag{2.6.23}$$

where

$$\vec{B} = \mu_0 \left(\vec{H}_d + \vec{M} \right) \tag{2.6.24}$$

Since the curl of $\overrightarrow{H_d}$ is zero, the demagnetizing field can be derived from a scalar potential,

$$\vec{H}_d = -\nabla \phi \tag{2.6.25}$$

substitution of Eqn. (2.6.25) into Eqn. (2.6.23) yields

$$\nabla^2 \phi = \nabla \cdot \vec{M} \tag{2.6.26}$$

inside the ferromagnetic object. Outside the object, the magnetization M always equals zero. The stray field $\vec{B} = \overrightarrow{H_d}$, so

$$\nabla^2 \phi = 0 \tag{2.6.27}$$

Thus we can solve for the magnetostatic field by solving for the potential using Eqn. (2.6.27) subject to boundary conditions required by Maxwell's equations: the normal component of the induction $\vec{B}$ and the tangential component of field $\overrightarrow{H_d}$ must be continuous at the boundary:

$$\hat{n}\cdot\left(\vec{B}_{ext}-\vec{B}_{\text{int}}\right)=0 \tag{2.6.28}$$

$$\hat{n}\times\left(\vec{H}_{d,ext}-\vec{H}_{d,\text{int}}\right)=0 \tag{2.6.29}$$

where $\hat{n}$ is a unit vector pointing outward at every point of the surface.

In terms of the scalar potential, the equivalent conditions are

$$\phi_{ext}=\phi_{in} \tag{2.6.30}$$

$$\frac{\partial\phi}{\partial n}\Big|_{ext}-\frac{\partial\phi}{\partial n}\Big|_{\text{int}}=\vec{M}\cdot\hat{n} \tag{2.6.31}$$

Thus the surface of a bulk-magnetized body determines the overall response of a phenomenon having its origin at the atomic level. Solving the differential equation, we can write expression for the potential and demagnetizing field as:

$$\phi(r)=\frac{1}{4\pi}\left[-\int_V\frac{\nabla\cdot M(r')}{|r-r'|}dV'+\int_S\frac{\hat{n}\cdot M(r')}{|r-r'|}dS'\right] \tag{2.6.32}$$

$$H_d(r)=\frac{1}{4\pi}\left[-\int_V\frac{(r-r')\nabla'\cdot M(r')}{|r-r'|^3}dV'+\int_S\frac{(r-r')\hat{n}\cdot M(r')}{|r-r'|^3}dS'\right] \tag{2.6.33}$$

the magnetostatic energy is given by

$$E_{ms} = -\frac{\mu_0}{2}\int_V \vec{M}\cdot\vec{H}_d\, dV \tag{2.6.34}$$

From the above equation, we can see that magnetostatic energy expresses a nonlocal interaction, because the magnetostatic field functionally depends, through the boundary value problem, on the whole magnetization vector field.

(4) Zeeman Energy

The Zeeman Energy term can be seen as the potential energy of a continuous magnetic moments distribution subject to external field H_a:

$$E_{zeeman} = -\mu_0\int_V \vec{M}\cdot\vec{H}_a \tag{2.6.35}$$

(5) The free energy function

Now we are able to write the complete expression for the free energy of the ferromagnetic body by collecting all the energy terms:

$$E_{tot} = \int_V \left[A(\nabla\vec{m})^2 + w_a - \tfrac{1}{2}\mu_0\vec{M}\cdot\overrightarrow{H_d} - \mu_0\vec{M}\cdot\overrightarrow{H_a}\right] dV \tag{2.6.36}$$

(ii) Static micromagnetic equilibrium

At constant external field and temperature, the equilibrium states (or metastable states) are given by the minima of the free energy. Since $\overrightarrow{\boldsymbol{M}} = M_S \, \overrightarrow{\boldsymbol{m}}$, the unknown is the magnetization unit vector field $\overrightarrow{\boldsymbol{m}}$.

Here we impose that the first-order variation δE_{tot} vanishes for any variation $\delta\overrightarrow{\boldsymbol{m}}$ of the vector field $\overrightarrow{\boldsymbol{m}}$, with the constraint

$$|\vec{m} + \delta\vec{m}| = 1 \tag{2.6.37}$$

The derivation of the approach based on standard variational principles can be found in Ref. (11). Essentially, setting the first variation of the total energy to zero leads to two equations. The first one is a volume equation:

$$\vec{m} \times \left[\frac{2A}{M_s} \nabla^2 \vec{m} + \mu_0 \left(H_a + H_d - \frac{1}{\mu_0 M_s} \frac{\partial E_{anis}}{\partial \vec{m}} \right) \right] = 0 \tag{2.6.38}$$

If we define the last term of the above equation as the anisotropy field $\overrightarrow{H_K}$:

$$\vec{H}_K = -\frac{1}{\mu_0 M_s} \frac{\partial E_{anis}}{\partial \vec{m}} \tag{2.6.39}$$

then the total effective field can be defined as

$$\vec{H}_{eff} = \frac{2A}{\mu_0 M_s} \nabla^2 \vec{m} + \left(\vec{H}_a + \vec{H}_d + \vec{H}_K \right) \tag{2.6.40}$$

Eqn. (2.6.38) can be written as

$$\vec{m} \times \vec{H}_{eff} = 0 \tag{2.6.41}$$

with the boundary condition on the surface given by:

$$2A \frac{\partial \vec{m}}{\partial \hat{n}} \times \vec{m} = 0 \tag{2.6.42}$$

where $\hat{\boldsymbol{n}}$ is the surface outward normal vector. If there is no surface anisotropy, with $|\vec{m}| = 1$, and

$$\vec{m} \cdot \frac{\partial \vec{m}}{\partial \hat{n}} = 0 \tag{2.6.43}$$

we have the Brown's equation

$$\frac{\partial \vec{m}}{\partial \hat{n}} = 0 \tag{2.6.44}$$

which allows us to find the equilibrium configuration of the magnetization within the body. Equation (2.6.41) states that the torque exerted on the magnetization by the effective field must vanish at equilibrium. Thus solving the differential equation with boundary condition can give us the static equilibrium magnetization states. However, as is shown above, Brown's equations are nonlinear differential equations, with the effective field having a functional dependence on the whole vector field $\vec{\boldsymbol{m}}(\vec{\boldsymbol{r}})$. The existence of exact analytical solutions is hard to find. Thus, in practice, computation is carried out by iterations starting from an arbitrary given initial magnetic conditions. The system energies of each iteration step are calculated and compared with the presses step to determine the evolution direction of the system. This process usually requires a lot of memory spaces and calculation time. Therefore, numerical solution of Brown's equation

is usually calculated only for magnetic objects below 100 nm on desktop workstations used in labs.

(7) Dynamic problem: the LLG equation

Brown's equation describes the static equilibrium configurations of a magnetized body, regardless of how the magnetization reaches its equilibrium during the time. However, magnetization reversal is intrinsically a dynamic phenomenon and in order to predict magnetization states correctly during and after reversal we should in principle take account of the dynamic behavior of the system. Since Victora (1987) first used a dynamic approach in studies of longitudinal thins films, [61] most of the dynamic models are based on the Landau-Lifshitz Gilbert (LLG) equation. [60]

From quantum mechanics, there is a proportionality relationship between the magnetic spin moment μ and the angular momentum L of the electrons.

$$\vec{\mu} = -\gamma \vec{L} \tag{2.6.45}$$

where $\gamma=2.21\times10^5$ $mA^{-1}s^{-1}$ is the absolute value of the gyromagnetic ratio

$$\gamma = \frac{g|e|}{2m_e c} \tag{2.6.46}$$

By applying the momentum theorem one can relate the rate of change of the angular momentum to the torque exerted on the particle by the magnetic field $\vec{H}$:

$$\frac{d\vec{L}}{dt} = \vec{\mu} \times \vec{H} \tag{2.6.47}$$

applying this equation to Eqn. (2.6.45):

$$\frac{d\vec{\mu}}{dt} = -\gamma\vec{\mu} \times \vec{H} \tag{2.6.48}$$

This can be written for each spin magnetic moment in volume dV:

$$\frac{d\vec{\mu}_j}{dt} = -\gamma\vec{\mu}_j \times \vec{H} \tag{2.6.49}$$

The magnetic field $\vec{H}$ should be locally spatially uniform. Now taking the volume average spin momentum:

$$\frac{1}{dV}\frac{d\sum_j \vec{\mu}_j}{dt} = -\gamma\frac{\sum_j \vec{\mu}_j}{dV} \times \vec{H} \tag{2.6.50}$$

The magnetization, $\vec{M} = \frac{\sum_j \vec{\mu_j}}{dV}$, we end up with the following continuum gyromagnetic precession model:

$$\frac{\partial\vec{M}}{\partial t} = -\gamma\vec{M} \times \vec{H} \tag{2.6.51}$$

for magnetic moments inside a magnetic object, the field $\vec{H}$ should be equal to the effective field $\vec{H}_{eff}$, then the *Landau-Lifshitz equation* gives:

$$\frac{\partial\vec{M}}{\partial t} = -\gamma\vec{M} \times \vec{H}_{eff} \tag{2.6.52}$$

Thus, if the magnetization rate of change vanishes, the LL equation expresses the equilibrium condition given by Brown's 1st equation (Equation 2.6.41). In addition, LL equation is an integral-partial differential equation. The Neumann boundary condition given by the Brown's 2nd equation (Equation 2.6.44) is used.

Nevertheless, dissipative processes take place within dynamic magnetization processes, which is still missing from the LL equation. The microscopic nature of this dissipation is still not clear and is currently the focus of considerable research.[62] Gilbert (1955) introduced an additional torque term, whose components are proportional to the time derivative of the generalized coordinates.[63] It gives the *Landau-Lifshitz-Gilbert (LLG) Equation*:

$$\frac{\partial \vec{M}}{\partial t} = -\gamma \vec{M} \times \vec{H}_{eff} + \frac{\alpha}{M_s} \vec{M} \times \frac{\partial \vec{M}}{\partial t} \tag{2.6.53}$$

where $\alpha>0$ is the Gilbert damping constant, depending on the material (typical values are in the range between 0.001 to 0.1). We can see that, because the LLG equation is again a non-linear differential equation, finding an exact analytical solution is very difficult. In practice, people again use discrete numerical methods such as *Fast Fourier Transformation* (FFT) to calculate the solution for the magnetization configuration.

In LLG micromagnetic simulator,[64] before any calculations are carried out, the magnetic object is first discretized into many small cubes, called *cells*. The size of the cell must be small enough so that the magnetization gradient is small enough within each cell so that M can be viewed as uniform. Usually, the cell size should be comparable to the exchange length [65]

$$l_{ex} = \sqrt{\frac{2A}{\mu_0 M_s^2}} \tag{2.6.54}$$

The exchange length gives an estimation of the characteristic dimension on which the exchange interaction is prevalent. For typical magnetic recording materials, it is of the order of 5 nm to 10 nm.

Here, in Figure 2.18, we showed the effect of cell size on the simulation results:

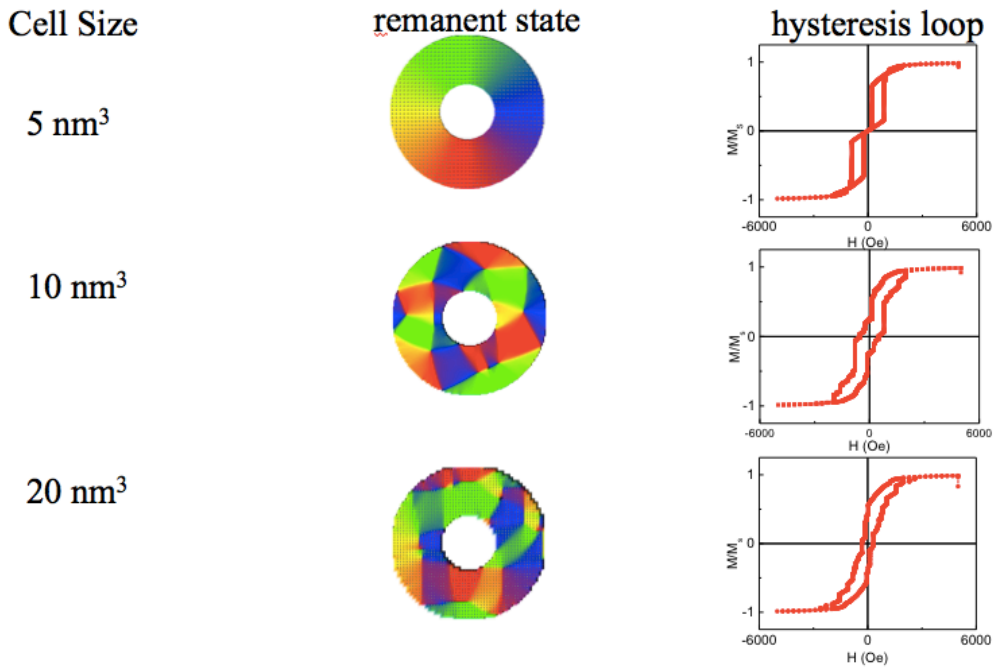

Figure 2.18. Micromagnetic simulation of 1 μm×1 μm×50 nm Fe ring structure, the remanent state and the hysteresis loop. Simulation with 5 nm^3 cell size should be most close to real situation, while simulations with 10 nm^3 and 20 nm^3 fail because the cell sizes are too large compared with the exchange length of Fe.

As can be seen in Figure 2.18, as the cell size increase from 5 nm to 20 nm, the remanent states and hysteresis loops of the ring have changed from vortex state and double-step loop to multi-domain state and single-step loop. This is because the larger

cell size created a rougher edge of the ring and the cell size has reached the limit of the exchange-dominated hypothesis.

The choice of material parameters such as the saturation magnetization M_s, exchange integral J, the magnetocrystalline anisotropy constant K, temperature T and Gilbert damping constant α can also affect the results of the simulation.

The choice of boundary condition also has an important effect on the simulation, especially when you are simulating 1-D long magnetic nano-wire or 2-D continuous magnetic thin film. Without setting the correct periodic boundary condition (PBC), the simulator views the object as a micron-sized pillar or bar instead of film or wire. Here in Figure 2.19, we show the simulation of a continuous 2-D epitaxial Co film with perpendicular anisotropy:

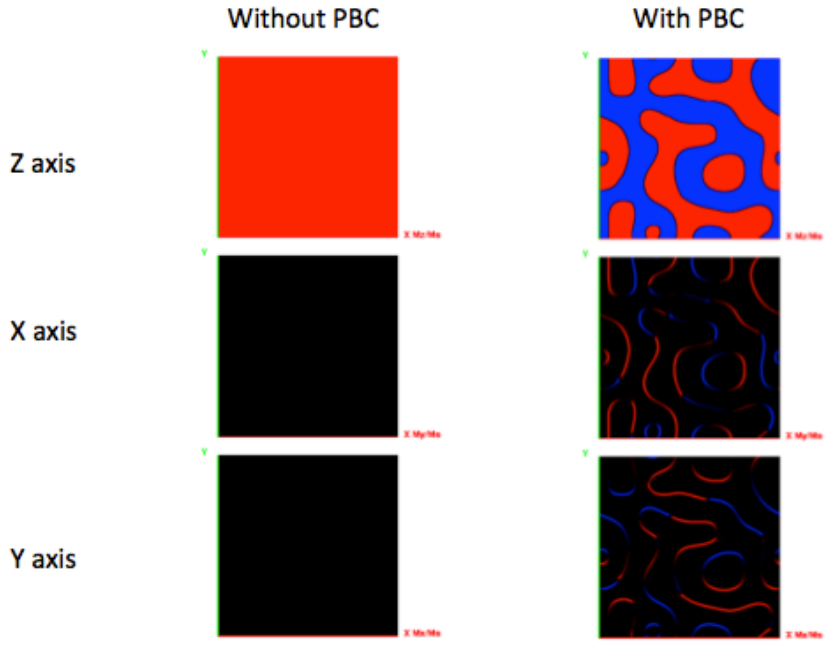

Figure 2.19 Micromagnetic simulation of a 2 μm × 2 μm × 20 nm epitaxial Co film with perpendicular (z axis) anisotropy, without (left) and with (right) periodic boundary condition.

As we can see in Figure 2.19, without PBC, the object is calculated as a Co post with easy axis in the z axis, thus the magnetization is pointing perpendicular in the out-of plane direction. With PBC, however, the simulation shows that it breaks into maze-like multi-domain state, very similar to those found by MFM in real 2-D thin films.

Two kinds of relaxation methods of magnetization are calculated by the LLG simulator. The first is the energy path, which is based on Brown's Equations. In the energy path, the simulator calculates the demagnetization field in a point-by-point method, then the magnetization direction is relaxed to the effective field direction. After each iteration, the local effective field and the total energy of the system is updated. The simulator keeps record of the residual torque of the local effective field exerted on M, if it is smaller than a preset value, the calculation is automatically stopped there.

Another relaxation path is the time path, which is built on solving the LLG equation. The relaxation is based on a given fixed time step. During each step, the magnetization of each cell is allowed to relax over a small time interval, obeying the LLG equation. The total energy of the system is calculated and recorded for this iteration. Then, another step of relaxation after the time interval is calculated. This iteration repeats until the subsequent changes in the time interval leads to a change in the total energy less than a prescribed value. Then, the calculation is stop. The dynamic calculations of the demagnetization field usually use the FFT methods, which means the calculation size scales up as $Nln(N)$. This is smaller than the point-by-point method, scaling as N^2. Thus, for micron sized magnetic pattern, the time relaxation method usually gives a much quicker result.

The existence of defects also plays a very important role in the micromagnetic simulations. Voids (M_s=0) and pinning sites (pinning fields=infinity) usually act as nucleation centers during reversal, which greatly decreases the coercive field H_c value. In Figure 2.20, we show the simulation result of the hysteresis loop of a continuous Fe film:

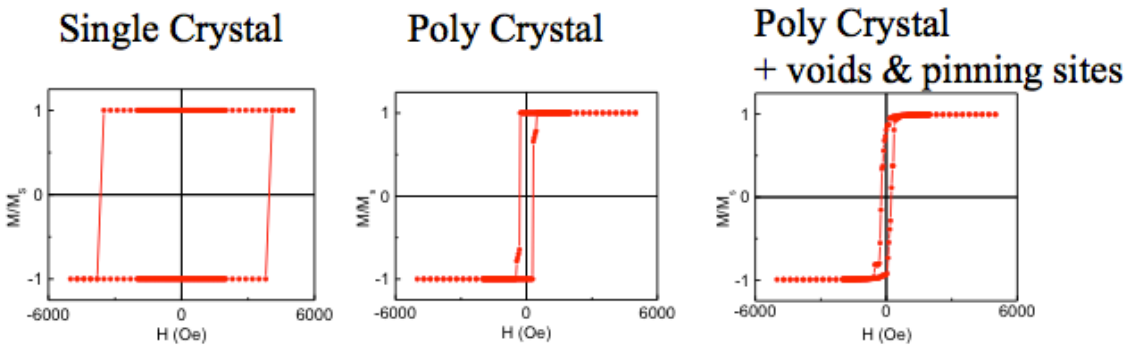

Figure 2.20. Micromagnetic simulation of hysteresis loops of a 2-D continuous Fe film.

As can be seen in Figure 2.20, in perfect single-crystal Fe film, due to lack of nucleation sites, the coercive field is very large, which is not observed in real Fe film samples. However, if we introduce a small distribution of easy axis, or 0.2% of voids/pinning sites into the system, the coercivity is greatly reduced.

The effect of the temperature (thermal motions) can be treated numerically by adding a random thermal field to the effective field in the LLG equation. This leads to the *Langevin* equation: [66]

$$\frac{\partial \vec{M}}{\partial t} = -\gamma \vec{M} \times \left(\vec{H}_{eff} + \vec{H}_{thermo} \right) + \frac{\alpha}{M_S} \vec{M} \times \frac{\partial \vec{M}}{\partial t} \qquad (2.6.55)$$

The random field, $\vec{H}_{thermo}$, describes the coupling of the magnetic system with a heat bath. It accounts for the interaction of the magnetic polarization with the microscopic degrees of freedom that causes the fluctuation of the magnetization distribution. In LLG micromagnetic solver, a random thermo induced effective field $\vec{H}_{thermo}$ obeying the *Gauss* distribution is assigned to each cell by the simulator during the simulation if the simulation temperature is larger than 0 K. [64]

To sum up this chapter, in order to study the magnetic properties of the thin-film ring structures, we use series of fabrication techniques including thin film deposition and lithography patterning. Different characterization methods, such as X-ray diffraction (XRD), magneto-optical Kerr effect (MOKE) and magnetic force microscopy (MFM) are applied to study the magnetic behaviors of these nanoring patterns. Micromagnetic simulation is used to model and explain the behaviors observed.

Chapter 3

MAGNETIC PROPERTIES OF FE RING STRUCTURES WITH DIFFERENT THICKNESS*

3.1 Introductions

After discussion of the fabrication, characterization and modeling tools, we start the systematic investigation of the magnetic properties of the thin film ferromagnetic ring structures by studying the evolution of the magnetic properties with its geometric parameters: thickness, outer diameter and inner-to-outer diameter ratio. Starting in this chapter, we discuss the effect of the thickness variation. [67]

The evolution of magnetic switching mechanism is investigated for micron-scale polycrystalline Fe ring arrays with Fe layer thickness, t_{Fe}, varying from 10 nm to 50 nm (which shows the evolution of the hysteresis behavior within the reach of photolithography). Single-step and double-step switching are observed for the 10 nm and 50 nm rings, with 30 nm sample showing a transition behavior. As thickness increases, the first-step switching field, H_{c1}, increases, while the second-step switching field, H_{c2} and remanence magnetization, M_r decreases. Magnetic force microscopy imaging and micromagnetic simulations reveal that in the reversal process, H_{c1} and H_{c2} respectively corresponds to the switching fields of two distinct halves of the ring (separated equally along the field direction). The relative separation between these two fields decides the switching behavior of the ring.

* The content of this chapter has been published as
Yu-Feng, Hou and K. M. Krishnan, "Thickness-dependent evolution of magnetization reversal in micron-scale polycrystalline Fe rings", *J. Appl. Phys.* **111**, 033910 (2012).

3.2 Fabrication of D_{out}=2.4 μm Fe ring structures with different thickness

A series of Fe ring arrays with outer/inner diameter D_{in}/D_{out} =0.8 μm/2.4 μm and thickness, t_{Fe} , varying from 10 nm to 50 nm are fabricated on Si/SiO_2 substrate via a mask-transfer lithographic process described below.

First, Si wafers are cleaned in the cleanroom with a standard three-step RCA cleaning process. Then positive-tone photoresist AZ-1512 is spin-coated on the wafer at 3000 rpm. The wafers are then prebaked on a hotplate at 110 °C for 90 s. Then the UV exposure is carried out on an EVG aligner, with an exposure time of 3.3 seconds. The photo mask is provided by Nano Tech User Facility (NTUF) at University of Washington. After manually developing the pattern in a mixture of H_2O: AZ 300 MIF Developer = 3:1 for 45 s, the pattern is rinsed in DI water, followed by spin-drying and post-bake at 90 °C for one hour. The final resist ring array is shown in Figure 3.1 (a).

In order to transfer the resist ring patterns into ferromagnetic thin-film patterns, a mask transfer process is carried out in our sputtering lab. [68, 69] First, a 170 nm thick Mo sacrificial layer is deposited on top of the AZ-1512 resist ring structures in our ion-beam sputtering (IBS) system [Figure 3.1 (b)] with a beam voltage of 500 V. Then, the AZ-1512 resist is lifted-off in an ultra sonication assisted acetone bath for 3 mins, leaving a 170 nm Mo thin film with ring-shape holes on a Si wafer [Figure 3.1 (c)]. Then, multilayer of Ta (1 nm)/Cu (5 nm)/Fe (t_{Fe} nm)/Ta (3 nm), with thickness, t_{Fe} , varying from 10 nm to 50 nm is then sputtered into these ring-shape holes [Figure 3.1 (d)]. Finally, the Mo is chemically etched away in 37% hydrogen peroxide solution at room

temperature, leaving magnetic ring structures with the exact same ring shape as the AZ-1512 resist [Figure 3.1 (e)].

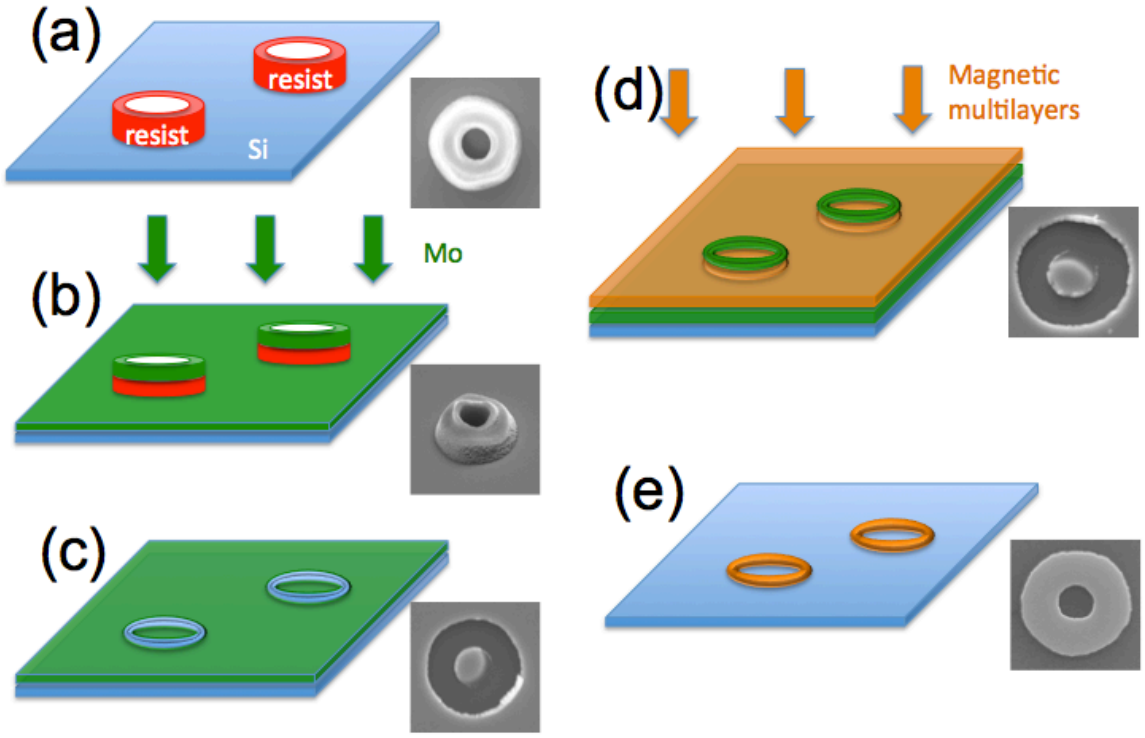

Figure 3.1 Schematic fabrication steps of Fe ring structures, the SEM images at the right corner shows the sample at the corresponding step: (a) AZ-1512 photoresist ring structure (b) Deposition of 170 nm thick Mo sacrificial layer (c) Lift-off of the photoresist, creation of ring shape holes in Mo layer (d) Deposition of Ta/Cu/Fe/Ta magnetic thin films (e) Chemical etching away the Mo sacrificial layer, completion of the pattern transfer.

The structures of the final ferromagnetic ring samples are shown in Figure 3.2 (a), the bottom Ta (1 nm)/Cu (5 nm) serves as a seed layer [70] and the top Ta (3 nm) is deposited as a capping layer to prevent the whole structure from oxidation. The SEM image of the ferromagnetic ring array is shown in Figure 3.2(b). The outer/inner diameter of the ring structure is fixed at D_{in}/D_{out} =0.8 μm/2.4 μm, while the thickness of the Fe layer varies from 5 nm to 50 nm. The edge-to-edge distance between rings is 3 μm, which minimizes of the cross talk between different rings. [71]

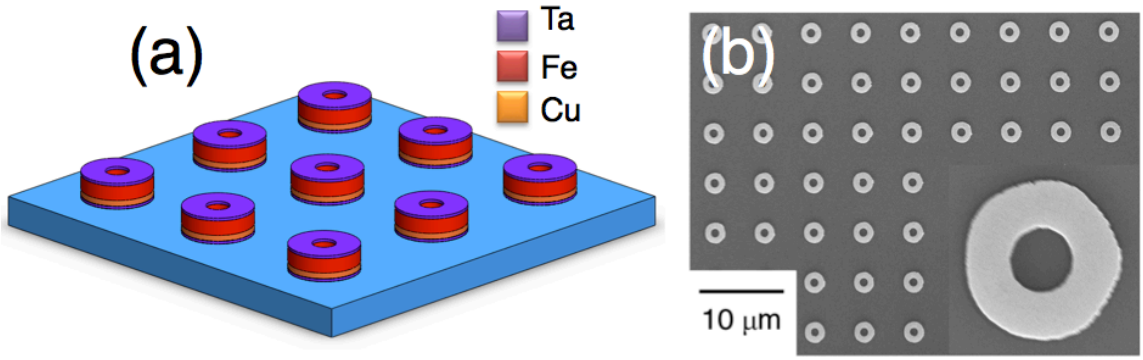

Figure 3.2 Schematic structure of the ferromagnetic ring array on Si wafer (a) and SEM image of the sample (b).

3.3 Evolution of magnetic hysteresis behavior in Fe ring structures as size increases

M-H hysteresis loops of the polycrystalline Fe rings are measured using a magneto-optical Kerr effect (MOKE) setup with external field applied in a longitudinal geometry at room temperature. To improve the signal-to-noise ratio, each loop is obtained by averaging the measured results over 20 times. Hysteresis loops of the 5 nm, [Figure 3.3 (a)], 10 nm [Figure 3.3(b)], 20 nm [Figure 3.3(c)], 30 nm [Figure 3.3(d)], 40 nm [Figure 3.3(e)] and 50 nm [Figure 3.3(f)] thick Fe ring samples are chosen to show the continuous complete evolution process of hysteresis behavior with thickness. The red and blue curves, respectively, represent the descending and the ascending branches of the loop. The first order derivative of magnetization with respect to the field, *dM/dH*, of the descending branch (red branch) is also plotted in the inset box at the right bottom corner of each figure. As shown in Figure 3.3(a) and 3.3(b), 5 nm and 10 nm thick Fe ring show a single-step transition from positive saturation to negative saturation, at the measured coercivity of -32 Oe for 5 nm sample and -75 Oe for 10 nm sample. The distribution of the switching field is presented by the inset *dM/dH* curve, which shows one sharp peak at

the coercive field, indicating the magnetization reversal is completed in one-step. The 50 nm Fe ring [Figure 3.3(f)] clearly shows a constricted shape with a two-step transition during magnetic reversal and a remanence state with no net magnetization, which is typical for the magnetic vortex state. The corresponding *dM/dH* plot shows two well-separated peaks. The first switching field H_{c1}= *96 Oe*, corresponds to the switching from the positive saturated state to the vortex state. The second switching field H_{c2}= *-262 Oe*, corresponds to the switching from vortex state to the reversed saturated state in the negative direction. In between these two switching steps, the vortex state is stable from -28 Oe to -152 Oe. The representative behavior between these two limiting cases of 10 nm and 50 nm is shown for 20 nm [Figure 3.3(c)], 30 nm [Figure 3.3(d)] and 40 nm ring structures [Figure 3.3(e)]. The *dM/dH* curve of the descending branch show two distinct peaks, yet these two peaks partially overlap, which indicates that the second reversal step initiates before the completion of the first step, without a stable vortex state formed in between.

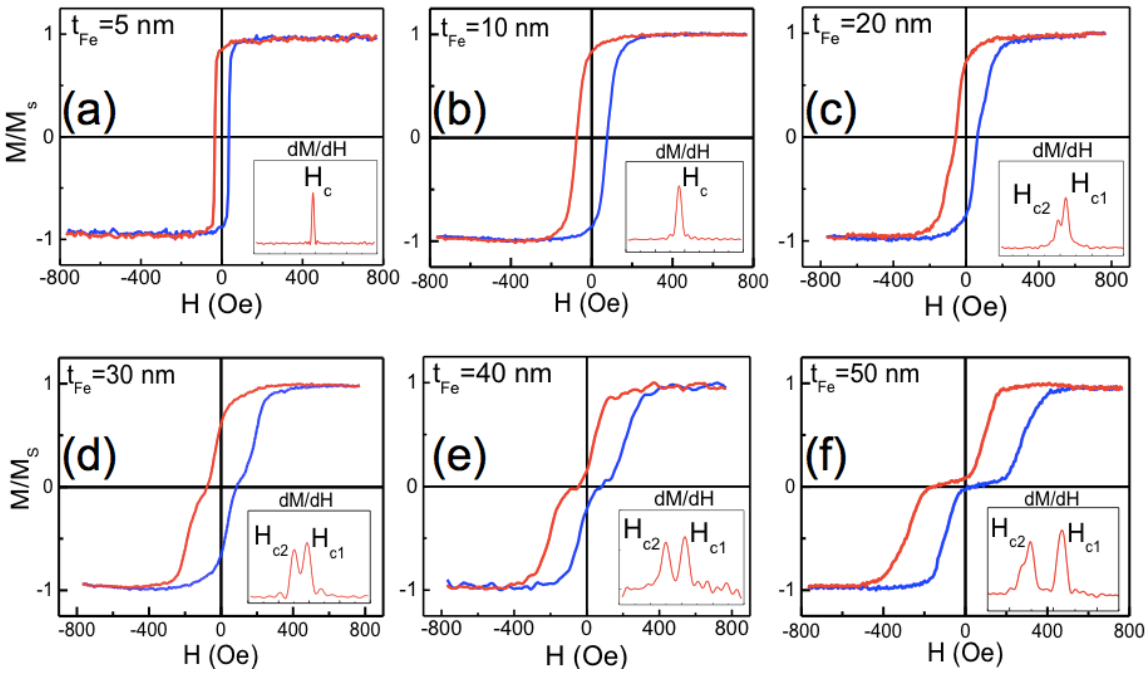

Figure 3.3 *M-H* hysteresis loops of (a) the 5 nm, (b) 10 nm (c) 20 nm, (d) 30 nm (e) 40 nm (e) 50 nm thick polycrystalline Fe ring arrays; the first order derivative, *dM/dH*, of the loop's descending branch (red) is plotted in the inset box located at the right bottom corner of each loop.

The variation of the remanent magnetization M_r/M_s and the values of the first and second switching fields as functions of the thickness for polycrystalline Fe rings are summarized in Figure 3.4. The remanence ratio of the ring reduces from 0.88 for 10 nm to 0.02 for 50 nm, which shows a transition in magnetic state from the high magnetization quasi-uniform state to flux-closure vortex state. The first switching field H_{c1}, which corresponds to the break of the positive saturated state, monotonically increases. This indicates that with the increase of thickness, the quasi-uniform state is increasingly unstable at remanence. The field-separation between the first and second step switching, H_{c1}-H_{c2}, is increasing with thickness, which finally leads to the formation of the vortex state.

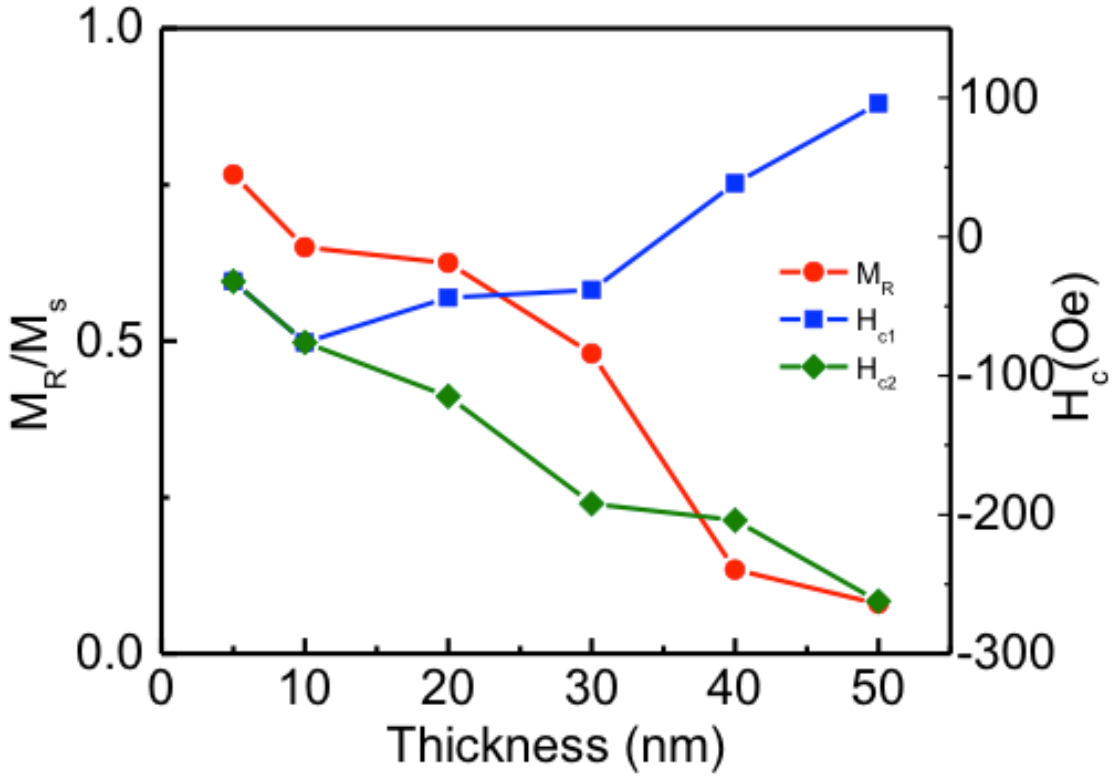

Figure 3.4 The remanence magnetization M_r, first-step switching field H_{c1}, and second step switching field H_{c2} as a function of the ring thickness.

3.4 Evolution of magnetic states during switching

The magnetic reversal process of the Fe rings are further investigated by MFM with the magnetic field applied parallel to the sample surface during scanning, and using 45 nm CoPt/FePt coated high coercivity probes with a lift height of 30 nm. Figure 3.5 shows MFM images of the 10 nm, 30 nm and 50 nm ring samples measured at the nominal values of magnetic fields as marked at the top of the images. As no significant difference in the magnetization reversal is observed with increasing or decreasing fields, we only display the images at different points of the descending branch. Figure 3.5(a) shows the MFM images of the 10 nm Fe rings varying from positive to negative saturation, corresponding to the descending branch in Figure 3.5(a). In Figure 3.5(a1), the applied

field is +400 Oe, the ring is saturated in the positive direction, and black and white areas with dipolar contrast are observed at the edge of the ring along the external field direction, indicating the formation of the magnetic poles of opposite polarity in the saturated state. Figure 3.5(a2-a5) correspond to the applied field value of +200 Oe, 0 Oe, -200 Oe and –400 Oe. As the field magnitude decreases, the spins start to relax to the local edge direction of the ring, causing the area of the dipolar contrast to shrink in size, as shown in Figure 3.5(a2). At the remanent state [Figure 3.5(a3)], the ring still remains in the quasi-uniform state in the positive direction. It is after the field has changed its direction and surpasses H_{c1} that the dipolar contrast suddenly switches its direction, and the reversal is finished in one step [Figure 3.5(a4)]. At -400 Oe [Figure 3.5(a5)], the ring is saturated in the negative direction.

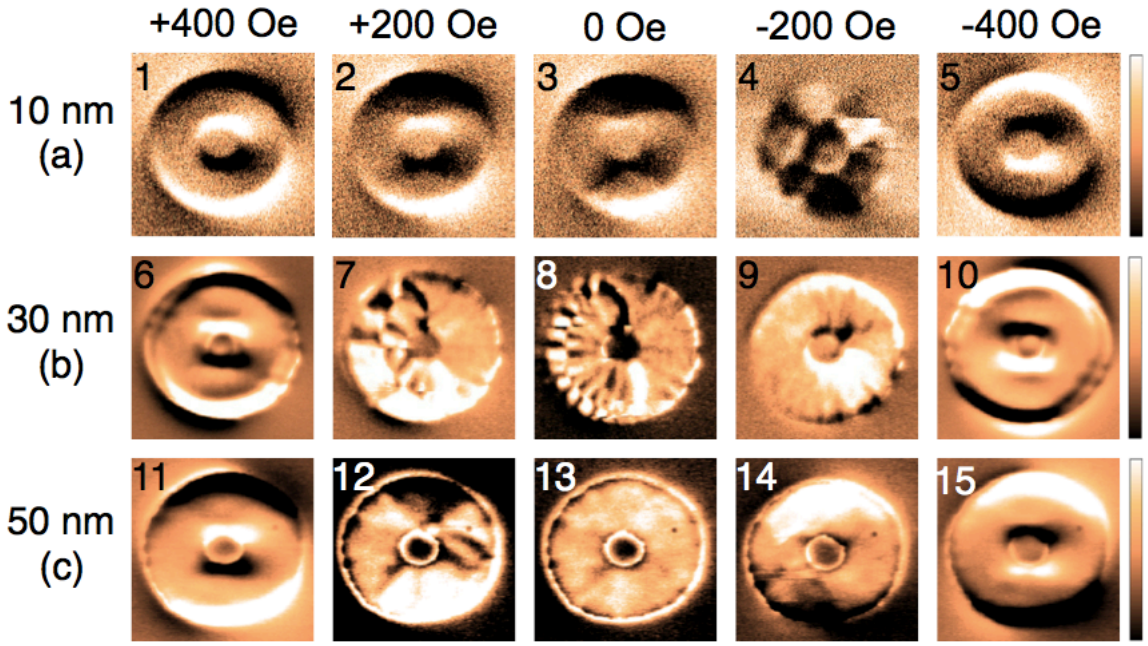

Figure 3.5 Selected MFM images showing the magnetic reversal process for (a) [(1)-(5)] the 10 nm thick polycrystalline Fe ring (b) [(6)-(10)] 30 nm thick polycrystalline Fe ring and (c) [(11)-(15)] 50 nm thick polycrystalline Fe ring. All the MFM images are taken under the applied magnetic fields as marked on hysteresis loops in Figure 3.3.

For the 30 nm Fe ring, the ring has the same saturated magnetic domain configuration at +400 Oe [Figure 3.5(b6)]. When the magnitude of the field decreases to H_{c1}, the first step of switching is initiated, as areas of black and white contrast are observed on the left half of the ring [Figure 3.5(b7)]. However, no obvious contrast is observed on the right half of the ring, indicating that the magnetization direction remains in the circumferential direction. At remanence, as shown in Figure 3.5(b8), while the magnetization in the right half of the ring is retained in its original circumferential direction, the left-half of the ring, divided by two domains walls from the right half, starts to show the presence of vortex-antivortex chains in the form of alternating black-white contrast. This is consistent with earlier reports [72] where they are also observed in the transient state from the saturated state to the formation of the vortex state. However, on further decreasing the field to -200 Oe, the vortex is not observed; instead, contrast starts to show on one half (right) of the ring [Figure 3.5(b9)], indicating the onset of the second switching step and the reversal of the magnetization on the right half of the ring via nucleation. Finally, as the field reached -400 Oe, the ring gets saturated in the negative direction [Figure 3.5(b10)]. Thus, H_{c1} and H_{c2} respectively correspond to the reversal of the left half and right half of the ring. However, between H_{c1} and H_{c2}, no stable vortex state is observed.

For the 50 nm ring, from the saturation state in the positive direction [Figure 3.5(c11)], the first switching step takes place on one half (right) of the ring via domain nucleation [Figure 3.5(c12)]. After the first step switching is completed, the magnetization direction of the right half is reversed to the circumferentially down direction and the ring forms the vortex state [Figure 3.5(c13)], as no magnetic contrast is observed. When the external field changes direction and reaches -200 Oe, the flux-closure state collapses and the

magnetization of the other half (left) of the ring switches via nucleation [Figure 3.5(c14)]; when this nucleation is completed, the ring now gets saturated in the negative direction [Figure 3.5(c15)].

3.5 Micromagnetic simulation of the switching process

Micromagnetic simulations of the magnetic reversal process of 10 nm, 30 nm and 50 nm Fe rings are performed using a Landau-Lifshitz-Gilbert micromagnetic solver. 64 The saturation magnetization and the exchange stiffness constant are set at the value of bulk Fe: M_s=1714 emu/cm^3 and A=12 μerg/cm. The cell size is set to be 5×5×5 nm^3. [73] The cubic magnetocrystalline anisotropy with randomly distributed easy axes is assigned to each of the 5×5×5 nm^3 cells of Fe due to the polycrystalline structure of Fe ring layer.

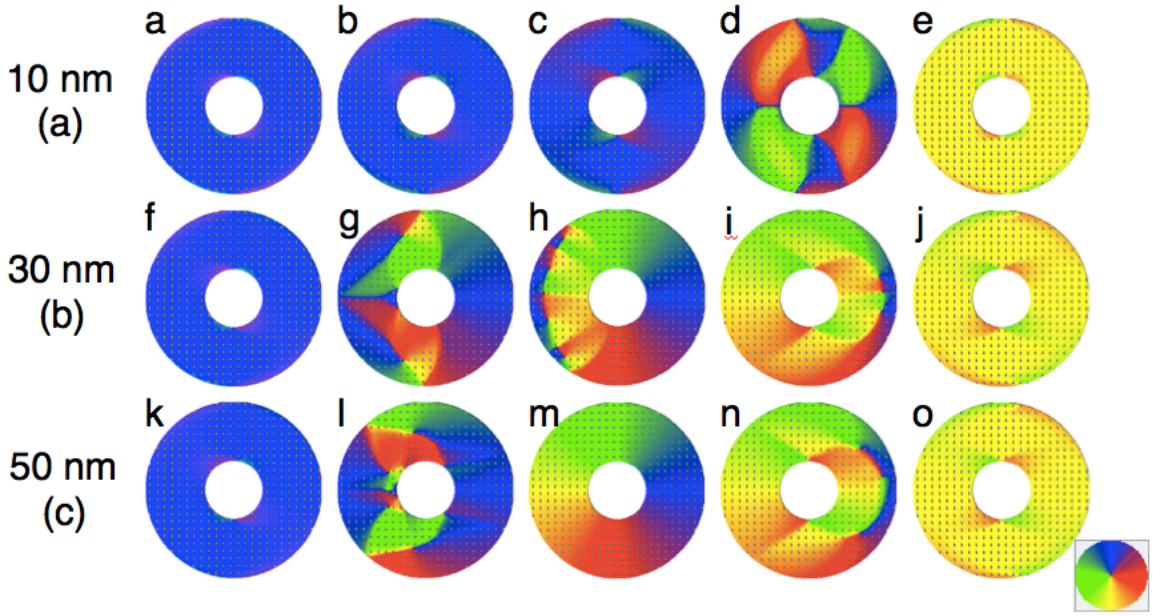

Figure 3.6 Micromagnetic simulated spin configurations of the 10 nm thick Fe ring in the magnetic reversal process (a)–(e), and the corresponding process for the 30 nm Fe ring (f)–(j) and 50 nm Fe ring (k)–(o). The magnetization direction is indicated by the color wheel or overlaid arrows.

In Figure 3.6, the first row shows the simulated magnetization reversal process of the 10 nm sample, while the second and third row shows the results of the 30 nm and 50 nm sample, respectively. In Figure 3.6(a), the 10 nm ring is magnetically saturated in the positive direction. As the magnitude of the field decreases, the spins at the edge of the ring starts to relax to the edge direction to minimize the stray field, as shown by the red and green regions at the edge of the ring in Figure 3.6(b). At the remanence state, the ring still remains in the high remanent quasi-uniform state [Figure 3.6(c)]. As the field changes direction and surpasses the coercivity, yellow-colored domains magnetized in the negative direction start to nucleate and grow [Figure 3.6(d)] and finally, the ring saturates in the negative direction [Figure 3.6(e)]. For the 30 nm rings, the initial state of the ring is also saturated in the positive direction [Figure 3.6(f)]. As the magnitude of the field decreases, domains start to nucleate and grow on only one half (left) of the ring [Figure 3.6(g)]. At remanence, the nucleation on the left half of the ring is not completed and the left-half ring breaks into multi-domain state; however, the spins on the right half of the ring almost remain unchanged. Further decreasing the field, the second step nucleation on the other half (right) of the ring starts while the nucleation on the left half is complete [Figure 3.6(i)]. When the nucleation on the right half of the ring is also completed, the ring is saturated in the negative direction [Figure 3.6(j)]. For the 50 nm ring, starting from the same saturated state in the positive direction [Figure 3.6(k)], when the field decreases, the first step nucleation occurs on the left half of the ring and breaks it into a multi-domain state [Figure 3.6(l)]. When the first step nucleation is completed, the magnetic spins on left half of the ring are aligned circumferentially in the negative direction, while the spins on the right half are aligned circumferentially in the positive

direction and the ring forms a perfect vortex state [Figure 3.6(m)]. As the field decreases and reaches H_{c2}, the second step nucleation starts on the right half ring [Figure 3.6(n)]. When the second step nucleation is finished, the ring forms a saturated state in the negative direction.

To qualitatively interpret the evolution of magnetization reversal process with thickness, H_{c1} and H_{c2} can be viewed as the switching fields for the two separate half-rings during the reversal process. As the external field is decreased from positive saturation, the first step switching is initiated and the magnetization of one half of the ring via domain nucleation (which half is decided by factors like edge roughness, defects etc.) is reversed. When the first switching step is finished, the ring will form the vortex state. Further decreasing the field will trigger the second step switching, which reverses the magnetization of the other half of the ring. When the second step switching is completed, the ring will get saturated in the negative direction. As the thickness of the ring, t_{Fe}, becomes smaller, the separation between the two switching field, H_{c1}-H_{c2}, monotonically decreases [Figure 3.4], until there is no vortex state formation between these two steps (30 nm). For ultra-thin 10 nm samples, H_{c1}-H_{c2} has been reduced to zero and thus only one step switching is observed.

3.6 Analytical model to explain the evolution trend as thickness changes

In order to interpret the evolution of hysteresis behavior and magnetic states, we calculate the energy of forming different magnetic states at remanence. Although complex magnetic configurations have been observed in magnetic ring structures at

remanent state, such as onion state and twisted state, here in our model, we only consider three simple magnetic states: vortex, single domain and axial, as shown in Figure 3.7(a)-3.7(c).

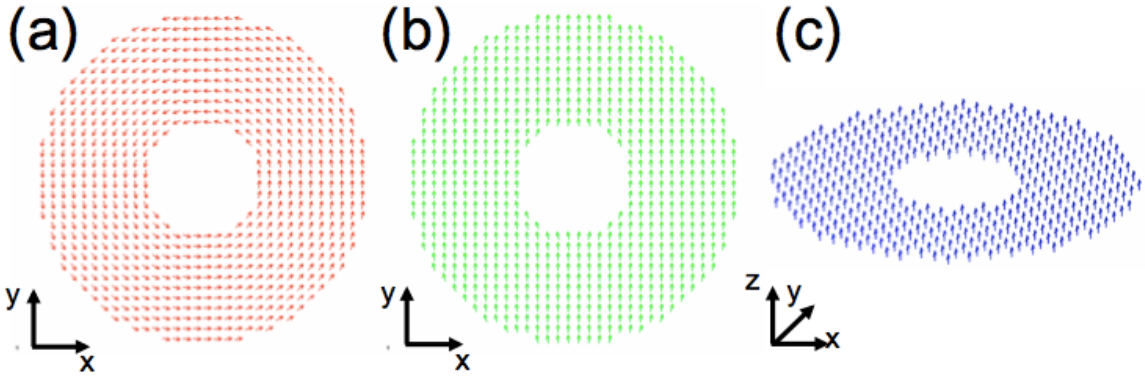

Figure 3.7 Three simplified remanence states of the ring structure (a) vortex state (b) single domain state and (c) axial state.

In the magnetic vortex state [Figure 3.7(a)], the spins are aligned in plane in the azimuthal angle direction. Since there are no magnetic poles formed throughout the ring structure, the energy of the vortex state mainly comes from the exchange interaction among neighboring spins. In the single domain state [Figure 3.7(b)], all the spins are aligned in plane in one direction. For axial state [Figure 3.7(c)], all the spins are also aligned in one direction, but now perpendicular to the ring plane.

Figure 3.8 show the evolution of energy density as a function of ring thickness for Fe rings with different outer diameter values. The energy density of the three different remanence states described in Figure 3.7 for ring structure with outer diameter of 100 nm, 300 nm, 1000 nm, 2400 nm are presented in Figure 3.7(a)-3.7(d). For these four sizes, the evolution trends of the three energy density curves are very similar: as thickness

increases, the energy density of the vortex state stays constant, the energy density of the single domain state monotonically increases while the energy density for the axial state monotonically decrease. For D_{out}=*2400 nm* sample we discuss in this chapter, the magnetic vortex state is the energy minimum in these three states. However, as the thickness value increases, the energy difference between the single domain state and the vortex state increases. This indicates that in thicker rings, the vortex state is energetically more stable compared to their thinner counterparts. This is why as the thickness t_{Fe} increases, the double-step switching with vortex state at remanence become dominance.

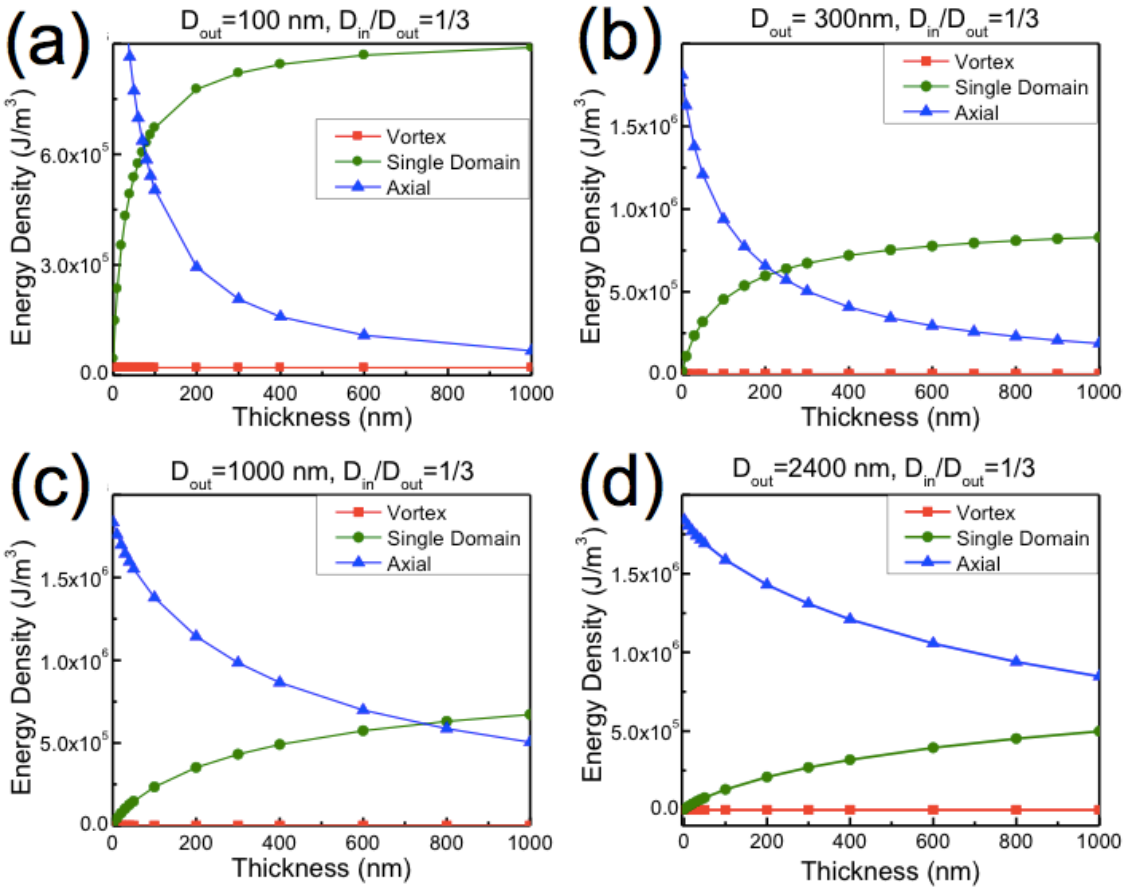

Figure 3.8 Micromagnetic simulated energy density of the vortex state, single domain state and axial state formed at remanence for Fe ring structures of (a) 100 nm (b) 300 nm (c) 1000 nm and (d) 2400 nm in diameter.

For the thin $t_{Fe}=10\ nm$ ring, the micromagnetic simulation results show that the vortex state is the energy minimum state, however, in experiments, they show one-step hysteresis behavior with high-remanence quasi-saturate state formed at remanence. In order to explain this phenomena, we use micromagnetic simulation to calculate the energy density change during such a designed process: first Fe ring structures with thickness of 10 nm, 30 nm and 50 nm are initially set to be in the magnetic vortex state, then an increasing external magnetic field is applied to the ring, force it to saturate into the single domain state, and then, the external magnetic field is removed, and let the rings relax back to their remanence states. The change in magnetization and energy density of the ring are recorded during this process.

Figure 3.9 shows the result of the micromagnetic simulation. The first row shows the change of magnetization M of the ring in this process, while the second row shows the change of energy density, which equals the sum of exchange energy density and magnetostatic energy density. The magnetization change [Figures 3.9(a)-3.9(c)] show the same result as we observe in experiment: the 10 nm ring relax to the single domain state with large magnetization residue, while 50 nm ring relax back to the vortex state with zero magnetization. The 30 nm ring shows intermediate property and relaxes half way back.

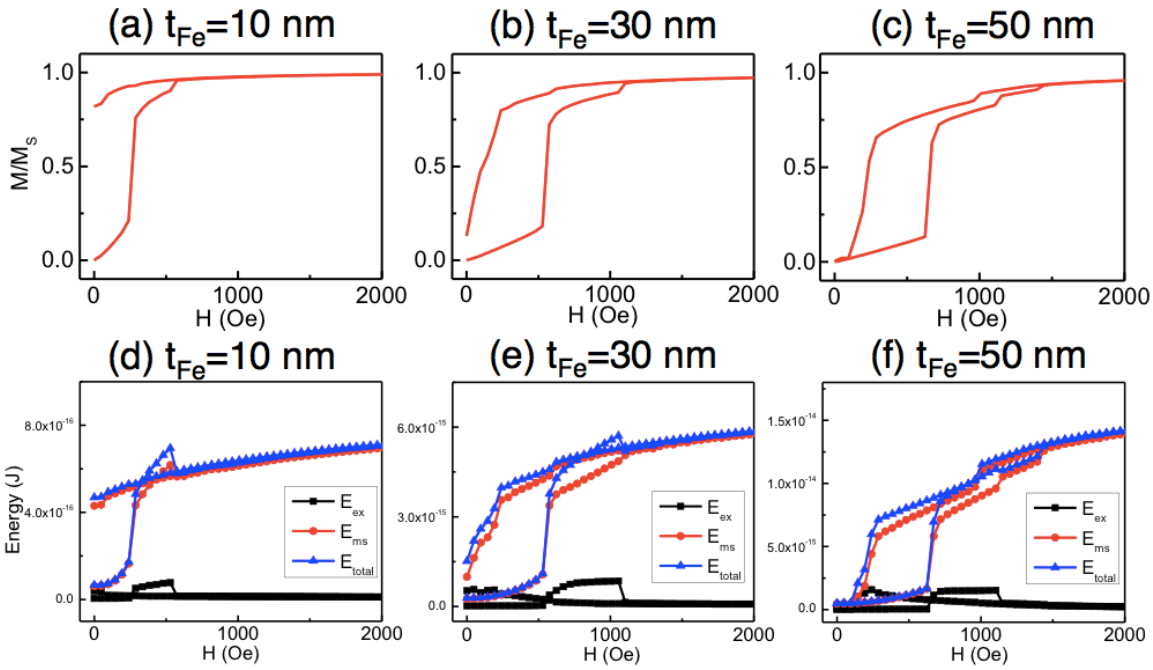

Figure 3.9 Micromagnetic simulation shows the change of magnetization *M*, exchange energy and magnetostatic energy when the ring structure initially at vortex state is saturated and relaxes back.

The energy density terms [Figures 3.9(d)-3.9(f)] show that from the initial vortex state to the single-domains state, the rings need to overcome an energy barrier of domain nucleation. When it relaxes back from the single domain state to the vortex state, it needs to overcome the same energy barrier. The remanence state of the ring is largely determined by this nucleation step: if the nucleation is not initiated, the ring remains in the single domain state; if the nucleation is completed, the ring forms the vortex state; If the nucleation is half-way done, the ring forms an intermediate state. This exactly coincide with the MFM images we observed in Figure 3.5.

Since the energy difference between the single domain state and vortex state is thickness-dependent: the thicker ring has higher single-domain state energy density, thus has smaller energy barrier to overcome during domain nucleation from single-domain

state to vortex state. As the external field magnitude decrease, the single domain state collapses first in the thicker ring sample. The domain nucleation starts at a relative large field and is able to complete as the external field decreases to zero, as in the 50 nm thick ring sample. For thinner ring, the energy difference between single domain state and vortex state is not that large, thus the nucleation is blocked by the nucleation energy barrier (which is determined by the increase in exchange energy and domain wall energy during nucleation) and does not start even when the external field decreased to zero, the ring still remains in the single domain state, as we observe on the $t_{Fe}=10\ nm$ ring sample. In ring structures with thickness values between these two cases, the remanence state of the ring shows some intermediate property, as we observe on 30 nm thick ring sample. This is the reason why the thin 10 nm ring shows single-step switching with single domain remanent state. As thickness increases, the hysteresis behavior of the ring evolves to double-step switching with vortex state at remanence.

3.7 Conclusion

We investigate the evolution of magnetic properties of the $D_{out}=2.4\ \mu m$ ring structures as the thickness of the ring, t_{Fe}, changes. We observe that as the thickness of the ring increases, the magnetic hysteresis behavior of the ring evolves from single-step to double-step, and the remanence state of the ring evolves from single domain state to vortex state. This is explained by the increasing energy difference between vortex state and single domain state as thickness increases.

Chapter 4

EFFECT OF LATERAL SIZE (D_{out}) ON THE MAGNETIC PROPERTIES OF THE RING STRUCTURES †

4.1 Introductions

In the previous chapter, the effect of the thickness on the magnetic properties of the Fe ring structure is discussed. Another very important geometric parameter that can affect the magnetic properties of the ring structure is the outer diameter or lateral size of the ring. As the size of the ring decreases from micron to nanometer, the originally dominant long-range magnetostatic interaction will gradually be overtaken by the short-range exchange interaction, which will lead to changes in the magnetic configurations of the ring structure. [74] This is because as the size decreases, the curvature of the ring will increase, resulting in larger angle between neighboring spins and thus higher exchange energy. [75] This indicates that the energetically stable state of the ring structures slowly evolves into the single domain state as the size of the ring decreases. This collapse of the vortex state has been experimentally observed in lithographically fabricated Permalloy disks in the sub 100 nm size range. [76] However, due to the removal of the high-energy vortex core, the vortex state in a magnetic ring structure is much more stable than the vortex state in a disk. Although theoretical calculations predict that the vortex state of the ring structure will collapse and evolve to single-domain state below 15 nm, [77, 78] this transition, however, has never been experimentally observed. So far, the smallest ring

† The content of this chapter has been summarized and written ito manuscript for later publication:
Y.-F. Hou and K. M. Krishnan, "Size-dependent magnetic switching and vortex state stability in Fe nanorings", (manuscript in preparation).

structure ever patterned by lithographic methods is 100 nm, [79] and yet the vortex state is still stable in that size. [79]

In this chapter, we observe the opposite trend, that is, for Fe ring structure in the mesoscopic size range, as size decreases, the ramanent state evolves from quasi-saturated single domain state to vortex state, and the stability of the vortex state is increasing. This abnormal behavior is explained by the evolution of energy difference between vortex state and single domains state with ring size.

4.2 Fabrication of Fe ring structures with different size

A series of Fe ring arrays with fixed inner-to-outer diameter ratio $D_{in}/D_{out}=1/3$, outer diameter D_{out} varying between 300 nm and 2.4 μm, thickness t_{Fe}=10 nm, are patterned on SiO_2/Si substrates by electron beam lithography using a FEI XL-30 scanning electron microscope (SEM). To align the pattern with the laser spot manually in the subsequent magneto-optical Kerr effect (MOKE) measurement, each array of rings of a certain specific size covers an area of 500 μm^2.

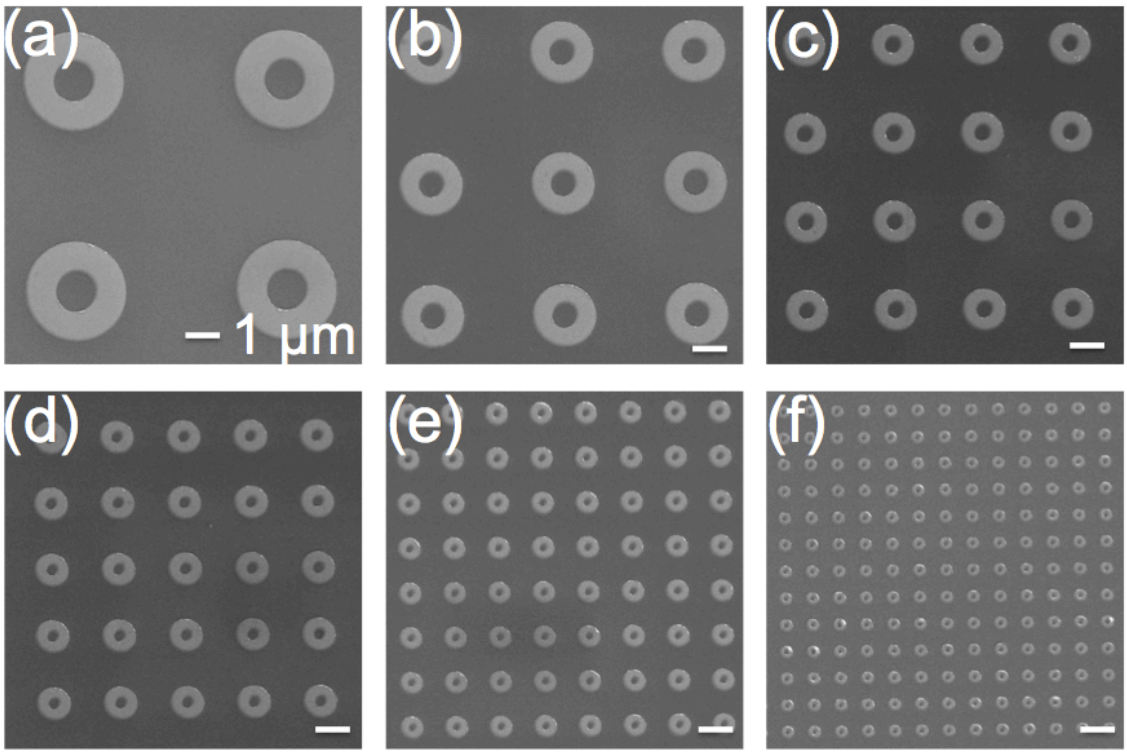

Figure 4.1 Scanning electron micrographs of arrays of Fe rings with fixed inner-to-outer diameter ratio $D_{in}/D_{out}=1/3$ and outer diameter of (a) 2.4 μm, (b) 1.5 μm, (c) 1 μm, (d) 750 nm, (e) 500 nm, and (f) 300 nm. For ease of comparison in size, the magnification is fixed at ×9000 and a 1μm scale bar is include at the bottom right corner of each image.

Magnetic multilayers composed of Ta (1 nm)/Fe (10 nm)/Ta (2 nm) are sputtered onto the pre-patterned resist layer at room temperature in an ion beam sputtering chamber at 0.1 mTorr with a base pressure of 10^{-8} torr. After deposition, the lift-off procedure is carried out by submerging the sample in acetone, followed by ultrasonic bath. Then the samples are examined under SEM. Figure 4.1(a)-(f) show the SEM images of Fe ring arrays with outer diameter D_{out}=2.4 μm, 1.5 μm, 1 μm, 750 nm, 500nm and 300 nm, respectively. For ease of comparison in size, the magnification is fixed at ×9000 and a 1μm scale bar is include at the bottom right corner of each image. To minimize the cross talk between the rings, the edge-to-edge distance is kept the same as the ring diameter.[80]

4.3 M-H hysteresis loops of Fe ring structures with different sizes

The collective magnetic hysteresis behaviors of ring arrays are characterized by magneto-optical Kerr effect (MOKE). The MOKE is set up in the longitudinal mode to detect the magnetization component along the field direction in the optical plane of incidence. *M-H* hysteresis loops of the ring arrays with varying diameter are shown in Figure 4.2(a)-(f), respectively. The red and blue colors in the hysteresis loops correspond to the descending and ascending branches of the curves. In order to show the switching field distribution of the ring arrays, the first order derivative of the magnetization with respect to external field, d*M*/d*H* of the descending branches (red) are plotted at the right bottom corners of each loop. Hysteresis loops along different directions of the sample are also measured and no differences is observed, which indicates that the intrinsic magnetocrystalline anisotropy of Fe and the dipolar interactions among the polycrystalline Fe rings are negligible.

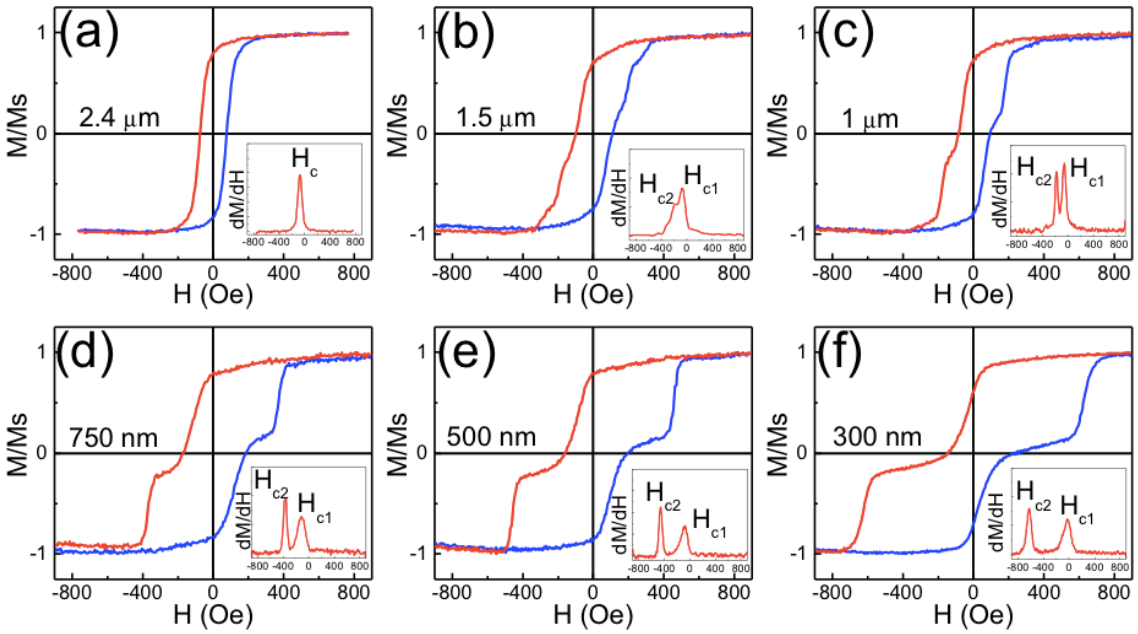

Figure 4.2 *M-H* hysteresis loops of lithographically patterned Fe ring arrays with different sizes (a) 2.4 μm, (b) 1.5 μm, (c) 1 μm, (d) 750 nm (e) 500 nm, and (f) 300 nm. The first order derivative, d*M*/d*H*, of the descending branches (red) are plotted in the inset box located at the right bottom corner of each loop. T_{Fe}=10 nm for all samples.

Figure 4.2(a)-(f) shows the complete evolution of magnetic hysteresis behavior with decreasing ring size. In Figure 4.2(a), the 2.4 μm ring shows a one-step hysteresis loop, the corresponding d*M*/d*H* plot has a single peak at the switching field H_c= *-75 Oe*. As the size of the ring decreases to 1.5 μm [Figure 4.2(b)] and 1 μm [Figure 4.2(c)], while the first switching slightly increases to -70 Oe, a distinct second peak in the d*M*/d*H* plot starts to appear on the left side of the first peak, which creates a small kink in the hysteresis loop during switching. The existence of the second switching field indicates that the switching had two independent steps. Although the separation between H_{c1} and H_{c2} increases as the ring size decreases from 1.5 μm to 1 μm, the two switching fields are still partially overlapping. On further decreasing the size of the ring to 750 nm [Figure 4.2(d)], 500 nm [Figure 4.2(e)], and 300 nm [Figure 4.2(f)], the separation between the first and

second switching fields, $|H_{c1} - H_{c2}|$, increases even further so that they became fully separated on the dM/dH curve. Between the two switching fields, in the kinked region of the hysteresis loop, the stable magnetic vortex state is observed. [81] As ring size decreases, the field range of the kink in hysteresis loop also increases, indicating that the stability of the vortex state is also increasing.

The evolution of the two switching fields, H_{c1} and H_{c2} is summarized in Figure 4.3. The experimentally measured data are plotted as scattered points while the micromagnetic simulation [64] results are plotted as continuous lines. The first-switching-filed H_{c1}, which corresponds to the nucleation field of the saturated state in the positive direction, decreases slightly in magnitude with decreasing ring size. However, the second-switching-field H_{c2}, which corresponds to the collapse of the intermediate vortex state, increases monotonically in magnitude as the ring size decreases. Compared with H_{c1}, the changing magnitude of H_{c2} is almost 7 times larger, indicating that the collapsing field of the vortex state is more sensitive to the size change. It also shows that the stability of the magnetic vortex state in smaller rings is much higher so that a large external field (H_{c2}) is needed to destroy it.

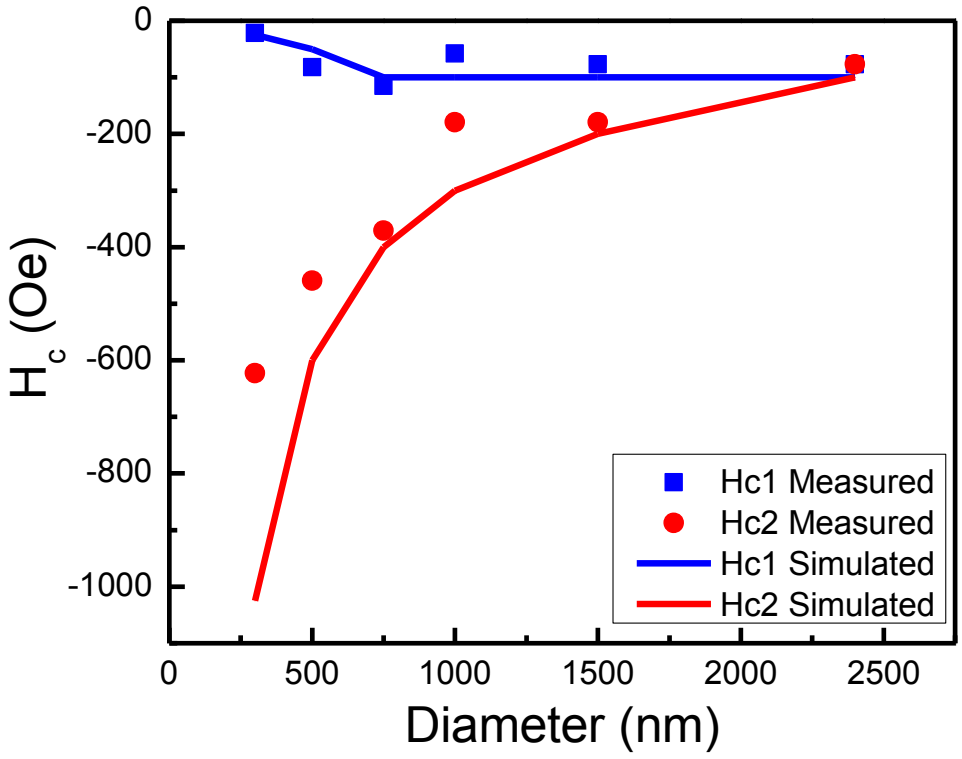

Figure 4.3 Summary of the first switching field H_{c1} and second switching field H_{c2}, as a function of the ring size. The scattered points are measured from the EBL samples while the curve is calculated by micromagnetic simulation.

4.4 Magnetic domain configurations of Fe ring structures of different sizes during switching

The magnetic domain configurations of the ring structures during switching are investigated by magnetic force microscopy (MFM). Images of the rings are taken on an Asylum Research MFP-3D SA scanning probe microscope with a variable field module (VFM) sample stage that can apply an in-plane DC field to the sample during imaging. To avoid artifacts from the high external fields applied during scanning, commercial high coercivity MFM probes with 45 nm CoPt/FePt coating is used. To minimize the effects

from the stray field of the tip, the sample-tip distance is kept at 80 nm while imaging. The images are obtained by scanning in the vibrating-lift mode, detecting the phase shift of the tip caused by magnetic interactions. Figure 4.4 shows selected domain images of the rings along the descending branches of the hysteresis curves for typical one-step switching process (D_{out}=*2.4 μm*) [Figure 4.4(a)] and double-step switching (D_{out} =*300 nm*) [Figure 4.4(b)].

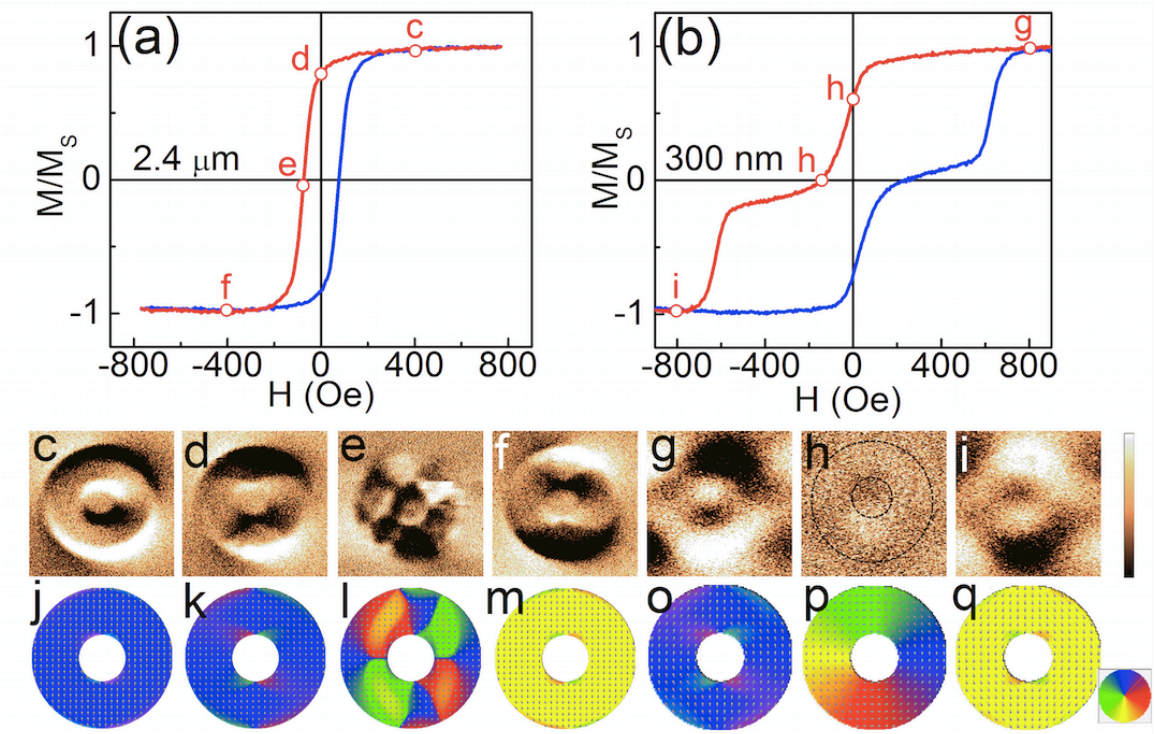

Figure 4.4 Selected MFM images of the Fe rings during switching for (a) single-step switching (b) double-step switching along the descending branch of the hysteresis loop. Micromagnetic simulation images of the corresponding states are shown below the MFM images.

As shown in Figure 4.4(c), when the external applied field is +400 Oe, the 2.4 μm ring is in the magnetic saturated state with its spins aligned to the positive direction. In the MFM image, alternating black and white contrast can be observed at the ring edge along the field direction, indicating the formation of magnetic "poles" in those regions. As the

magnitude of the applied field decreases to zero, [Figure 4.4(d)], the magnetization of the 2.4 μm is still in the positive direction in saturated state; while most of its spins still point in the positive direction, spins near the edge of the ring start to relax. Further reversing the field in the negative direction leads to a single-step switching at the coercivity field [Figure 4.4(e)]. Domains with black or white contrast can be seen all over the ring surface, showing that the ring is in multi-domain state during reversal. As the field further decreases to -400 Oe [Figure 4.4(f)], the switching is completed and the ring forms a reversed saturated state in the negative direction. Figure 4.4(c)-4.4(f) show that for large rings with single-step switching, the ring remains in the saturated state at remanence and reverses via one-step domain nucleation and growth.

For 300 nm rings, as shown in Figure 4.4(g), at +800 Oe, the ring is positively saturated with the spins aligned in the field direction. As the field decreases to 0 Oe, the MFM image shows that the ring at first keeps its magnetic contrast in the positive direction. However, during the scanning the magnetic contrast of the ring suddenly disappears [Figure 4.4(h)], which indicates that the magnetic state of the ring switches from the saturated state to a flux-closure magnetic vortex state during scanning with no intermediate metastable state observed. Further decreasing the field to -142 Oe [Figure 4.4(h)], the vortex state is still stable. As the field increases in the negative direction to -750 Oe, the vortex state collapses and the saturated state in the reverse direction is observed [Figure 4.4(i)]. Figures 4.4(g)-4.4(i) show that for small rings with double-step switching, the ring forms vortex state near remanence between the two steps. The major difference between the two switching modes is whether the ring forms a vortex or a quasi-saturated state during switching.

4.5 An energy-based analytical model given by micromagnetic simulations

To explain the evolution from a single-step to double-step switching as the ring size decreases, micromagnetic simulations via using the LLG micromagnetic simulator [错误！未定义书签。] are used to calculate the energy densities of different remanence states. Bulk values of the saturation magnetization (M_s=*1714 emu/cm*^{3}) and the exchange stiffness constant (A=*2.1 μerg/cm*) of the Fe layer [82] are used in the simulation and the cell size fixed at 5 nm^3.

As shown in Figure 3.7(a)-(c), three typical remanence states are included: (a) vortex state, in which all the spins point in the circumferential direction of the ring (b) single domain state, in which all the spins are aligned to one direction in the ring plane (c) axial state, in which all the spins are aligned in a direction perpendicular to the ring plane. For ring structures with fixed inner-to-outer diameter ratio D_{in}/D_{out}=*1/3* and thickness t_{Fe}=*10 nm*, Figure 4.5 shows the evolution of the energy density as a function of the ring outer diameter. Starting from D_{out}=*3 μm*, among the three remanence states, the energy density of the vortex state is the lowest, then the single domain state and finally, the axial state. As the diameter of the ring decreases from 3 μm, the energy density of the vortex state and single domain state both increase, while the energy density of the axial state decreases. However, from the plot, the rate of increase for the single domain state is faster than that of the vortex state, which leads to an increasing energy gap between these two states as the size is decreased. Moreover, the vortex state becomes energetically more and more favorable compared to the single domain state in smaller ring structures. As a result, smaller rings form stable vortex states during the double step switching and the

stability of the vortex state increases with decreasing size of the rings. Also, the plots indicates that the energy density of the vortex state finally catch up to that of the single domain state if the size of the ring is to decrease below 20 nm; a critical size where those two energy curves intersect. The energy density of the axial state also decreases with size and intersects the single domain state at 13.5 nm. Thus, for $D_{out} < 20\ nm$, the magnetic states of the ring theoretically will evolve from vortex state to saturated state, and finally, for $D_{out} < 13.5\ nm$, to the axial state.

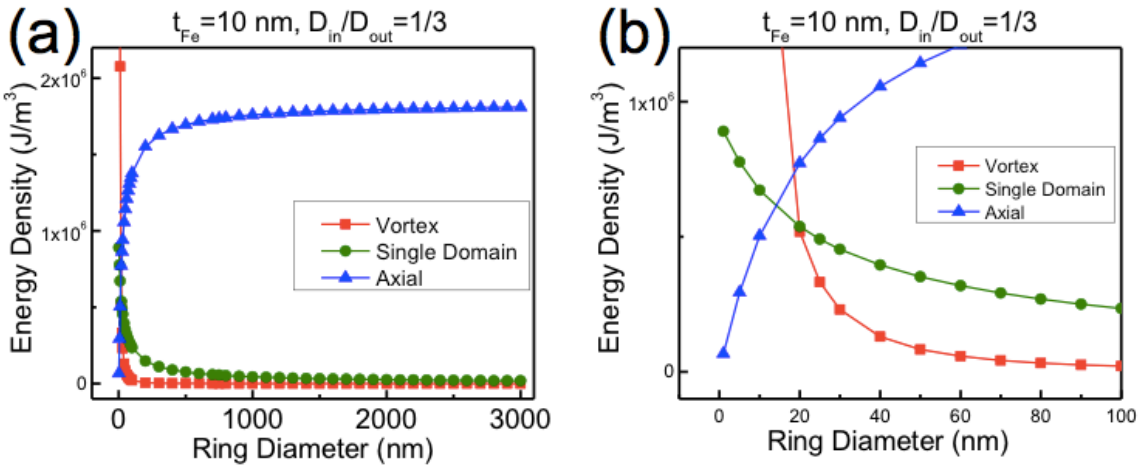

Figure 4.5 Variation of energy density of three different remanence states with respect to the outer diameter of the ring at $t_{Fe}=10\ nm$.

4.6 Conclusion

In conclusion, for lithographically patterned Fe ring array, we observe an evolution of hysteresis behavior from single-step switching to double-step switching as the size decreases from 2.4 μm to 300 nm. MFM images show that the major difference between these two switching modes is the formation of a vortex state during the switching process for double-step switching but not for the single-step switching. The reason for this evolution is investigated by micromagnetic simulation and successfully explained by the

increasing energy density difference between the single domain state and the vortex state as the size of the ring decreases.

Chapter 5

EFFECT OF WIDTH (D_{in}/D_{out}) ON THE MAGNETIC PROPERTIES OF THE RING STRUCTURES ‡

5.1 Introductions

In Chapter 3 and Chapter 4, the effects of ring thickness and size on the magnetic properties of lithographically patterned Fe ring structures are discussed. The last geometric parameter that defines the shape of a ring is the ring width, or inner-to-outer diameter ratio, D_{in}/D_{out}. As the inner-to-outer diameter ratio of the ring increases, the shape of the ring becomes narrower. The magnetic properties of the ring evolves from disk-like ($D_{in}/D_{out} \rightarrow 0$), where the magnetic reversal is dominated by domain nucleation and growth, to line-like ($D_{in}/D_{out} \rightarrow 0$), where the domain wall propagation plays an important role. [83, 84, 85]

In this chapter, we investigate the evolution of the magnetic reversal behavior of lithographically patterned Fe ring as inner-to-outer diameter ratio, D_{in}/D_{out}, changes. The hysteresis loop evolves from double-step to single-step with the decrease of D_{in}/D_{out} (ring becomes wider). Magnetic domain configurations of the narrow ring and wide ring are characterized by magnetic force microscopy (MFM) and simulated by LLG micromagnetic solver. [64] The evolution trend of the hysteresis behavior and remanence

‡ The content of this chapter has been summarized and written into manuscript for later publication:
Y.-F. Hou and K. M. Krishnan, "Width-dependent magnetic switching and vortex state stability in Fe rings", (manuscript in preparation).

state is explained by calculating the energy density difference between vortex state and single-domain state as D_{in}/D_{out} decreases.

5.2 Fabrication of Fe ring structures with different width

A series of Fe ring arrays with fixed outer diameter $D_{out}=2.4\ \mu m$, thickness $t_{Fe}=10\ nm$, inner-to-outer diameter ratio, D_{in}/D_{out} varying from 11/12 to 1/12 are fabricated on Si/SiO_2 substrates by a top-down technique combining electron beam lithography and subsequent deposition and lift-off process. The ring arrays are patterned using a FEI XL-30 scanning electron microscope (SEM) operated at 30keV beam energy on a 100 nm thick poly-methyl methacrylate (PMMA) resist. To manually align the pattern with the laser spot of the succeeding magneto-optical Kerr effect (MOKE) measurement, each ring array of a specific D_{in}/D_{out} value covers a square area of 500 μm^2. Then, multilayers of Fe (10 nm)/Ta (2 nm) are deposited onto the pre-patterned resist layer at room temperature in an ion beam sputtering chamber at 0.1 mTorr with a base pressure of 10^{-8} torr. After deposition, the lift-off is carried out by submerging the sample in acetone for 24 hours, followed by 10 s ultrasonic bath. Figure 5.1 shows the SEM images of Fe ring arrays with outer diameter $D_{out}=2.4\ \mu m$, inner-to-outer ratio D_{in}/D_{out} varying from 11/12 [Figure 5.1(a)], to 8/12 [Figure 5.1(b)], 4/12[Figure 5.1(c)], and 1/12 [Figure 5.1(d)]. To minimize the cross talk between neighboring rings, the edge-to-edge distance is kept the same as the ring diameter.

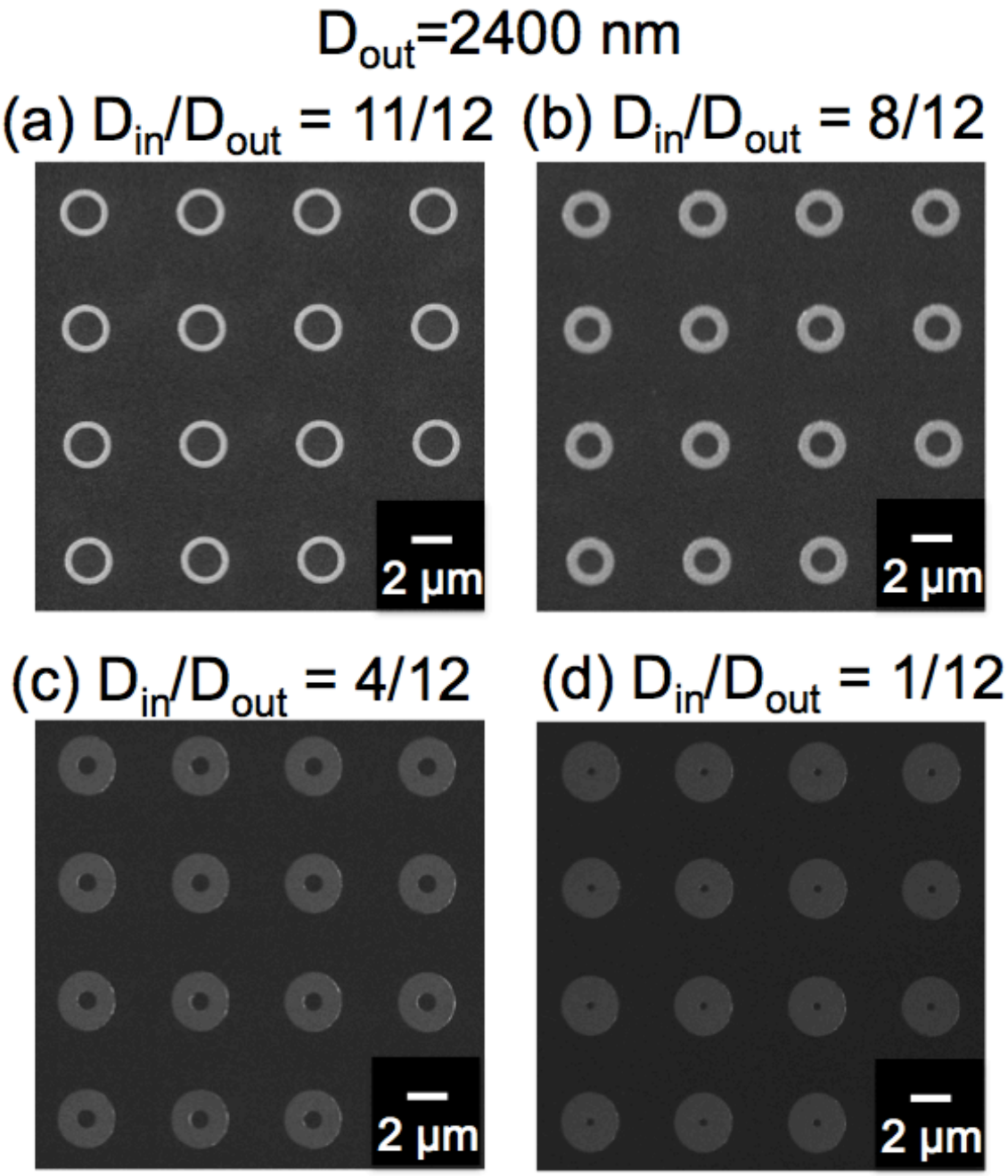

Figure 5.1 Scanning electron microscopy images of Fe ring arrays with fixed outer diameter D_{out}=*2.4 μm*, thickness t_{Fe}=10 nm and inner-to-outer diameter ratio D_{in}/D_{out} of (a) 11/12, (b) 8/12, (c) 4/12, and (d) 1/12.

5.3 M-H hysteresis loops of Fe ring structures with different width

The collective magnetic switching behavior of Fe ring arrays is characterized at room temperature by MOKE in a longitudinal geometry. For some of our narrow ring arrays, the sample/surface ratio is very low. To improve the signal-to-noise ratio of the MOKE measurement, each hysteresis loop is obtained by averaging the measured results over 20 times. The hysteresis loops of D_{out}=*2.4 μm* Fe ring arrays with inner-to-outer diameter ratio D_{in}/D_{out} varying from 11/12 to 1/12 are shown in Figure 5.2. The red and blue colors represent the descending and ascending branches of the loop, respectively. The first order derivative of the magnetization, *dM/dH*, of the descending branch (red) is plotted at the right-bottom corner of each loop.

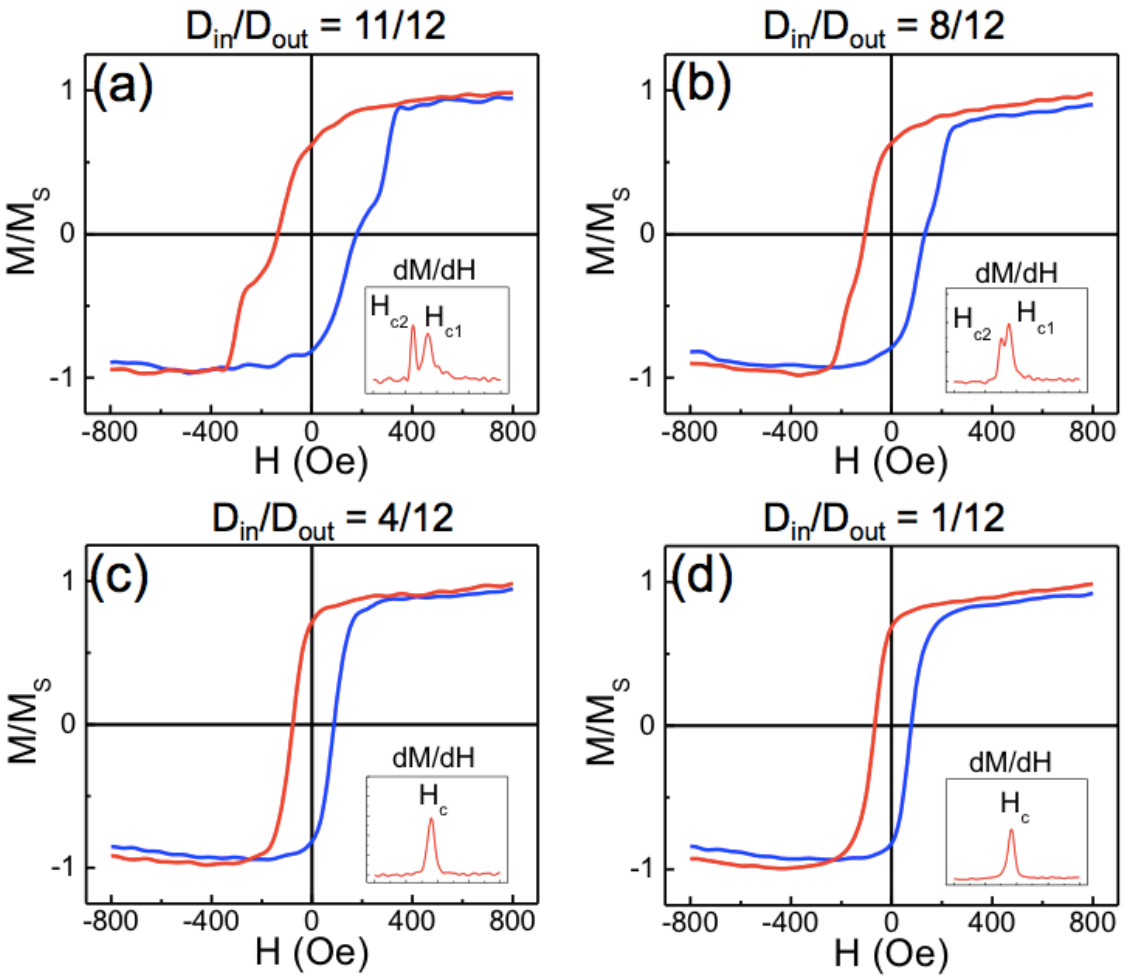

Figure 5.2 M-H hysteresis loops of Fe ring arrays with different inner-to-outer diameter ratio D_{in}/D_{out} of (a) 11/12, (b) 8/12, (c) 4/12, and (d) 1/12. The first order derivative, *dM/dH* of the descending branch (red) of the hysteresis loops are plotted at the right bottom corner of the curves.

The narrow ring with D_{in}/D_{out}=*11/12* [Figure 5.2(a)] shows a two-step hysteresis loop with 2 well-separated switching fields H_{c1}= *-115 Oe*, and H_{c2}= *-300 Oe*. In between these two switching fields, the hysteresis loop has a kink region in which the magnetization changes little with external field. For ring array with D_{in}/D_{out}=*8/12* [Figure 5.2(b)], the *dM/dH* curve also shows two distinct peaks at H_{c1} = *-102 Oe*, and H_{c2}= *-192 Oe*. However, the distance between these two switching fields, $|H_{c1} - H_{c2}|$, is decreasing with decreasing D_{in}/D_{out} ratio. As D_{in}/D_{out} decreases to 4/12 [Figure 5.2(c)], on the

dM/dH curve, the two switching fields merge into one single peak at H_c= *-75* Oe, and the hysteresis loop now becomes single-step. The widest ring sample with D_{in}/D_{out}=*1/12* [Figure 5.2(d)], the *dM/dH* curve shows it remains in the single-step switching, with its coercive field further decrease in magnitude, H_c=*-64 Oe*. The evolution of the switching fields with D_{in}/D_{out} ratio is summarized in Figure 5.3. Both H_{c1} and H_{c2} monotonically decrease with D_{in}/D_{out} ratio. However, the decreasing rate of the second switching field, H_{c2}, is much faster than the first switching field, H_{c1}. Therefore, the distance between the two switching fields, $|H_{c1} - H_{c2}|$, increases with D_{in}/D_{out}. Since we don't have the sample with D_{in}/D_{out}=5/12, 6/12 and 7/12, the only conclusion we can draw from the data is that H_{c1} and H_{c2} separate somewhere between D_{in}/D_{out}=4/12 and D_{in}/D_{out}=8/12. As H_{c1} and H_{c2} separate when the ring narrows down from D_{in}/D_{out}=*4/12* to D_{in}/D_{out}=*8/12*, the hysteresis loop evolves from single-step to double-step.

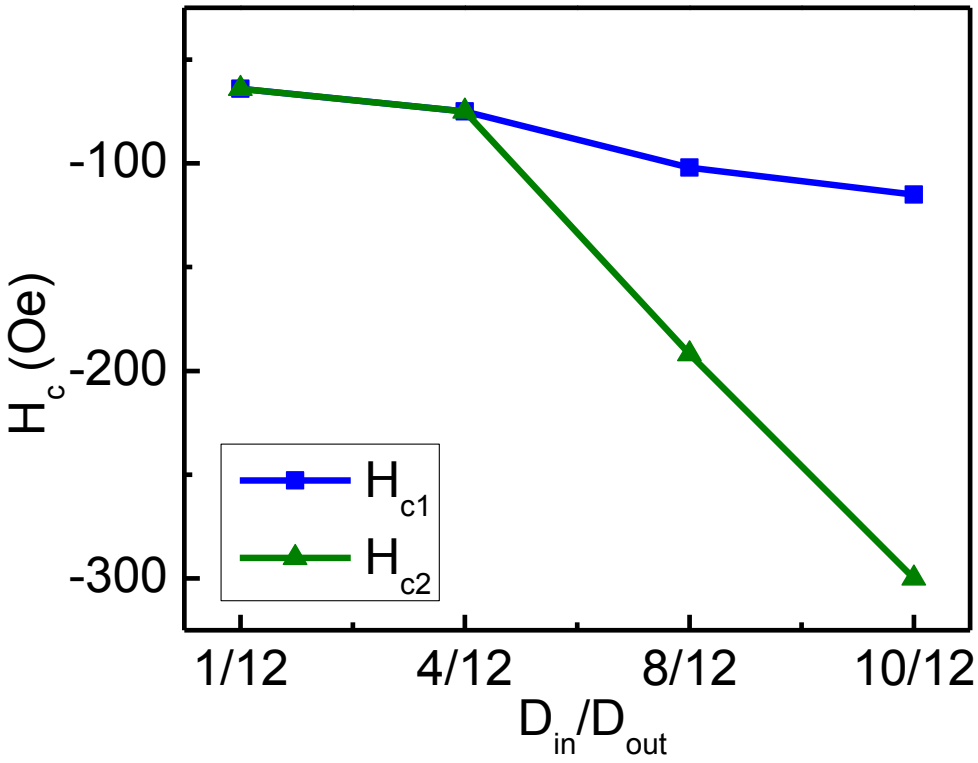

Figure 5.3 Summary of the first switching field H_{c1}, the second switching field H_{c2} as a function of inner-to-outer diameter ratio of the ring D_{in}/D_{out} ratio. H_{c1} and H_{c2} separate somewhere between D_{in}/D_{out} =4/12 and D_{in}/D_{out} =8/12.

5.4 Magnetic domain configurations of Fe rings of different width during switching

The magnetic domain configurations of the Fe rings with different D_{in}/D_{out} ratios during magnetic switching process are investigated by magnetic force microscopy (MFM). While scanning, a DC magnetic field is applied parallel to the sample surface by the variable field module (VFM) sample stage. Commercial Olympus high coercivity probes coated with 45 nm CoPt/FePt are used to detect magnetic signals from the sample surface at a lift-height of 30 nm. [86] Figures 5.4(b1)-5.4(b11) show the MFM images of narrow D_{in}/D_{out}=*11/12* Fe rings measured at the nominal values of magnetic fields as marked in

Figure 5.4(a). In Figure 5.4(b1), the ring is magnetically saturated in the positive direction, as black and white contrast at opposite sides of the ring originating from the two domain walls can be observed along the field direction. Alternating contrast also can be observed at the inner and outer edge of the ring, which is caused by the alignment of the spins to the field direction at full saturation. As the field magnitude decrease, the ring retains its domain configuration until remanence [Figure 5.4(b2)]. However, the magnetic contrast at the edge area of the ring gradually disappears because spins relax parallel to the edge due to the large shape anisotropy. Nevertheless, the two domain walls are still in their original positions. Further decreasing the external field and reverse its direction to -100 Oe, as shown in Figure 5.4(b3), while the domain wall at the bottom disappears, near the top of the ring there exist a complex multi-domain region with alternating black and white contrast. Although our MFM does not have the time resolution (8 min 30 s per frame) to show what happens between Figure 5.4 (b2) and 5.4(b3), judging from the position, it is reasonable to assume that the bottom domain wall moves upwards along the ring and annihilates with the top domain wall [Figure 5.4(b3)]. Further decreasing the field to -200 Oe, all the magnetic contrasts on the ring structure disappear, indicating the ring forms the vortex state [Figure 5.4(b4)]. As the field decreases to -400 Oe, as shown in Figure 5.4(b5), magnetic contrasts reappears on the ring structure with opposite direction, which indicates that the magnetization of the ring is reversed. At -600 Oe, the ring is saturated in the negative direction [Figure 5.4(b6)].

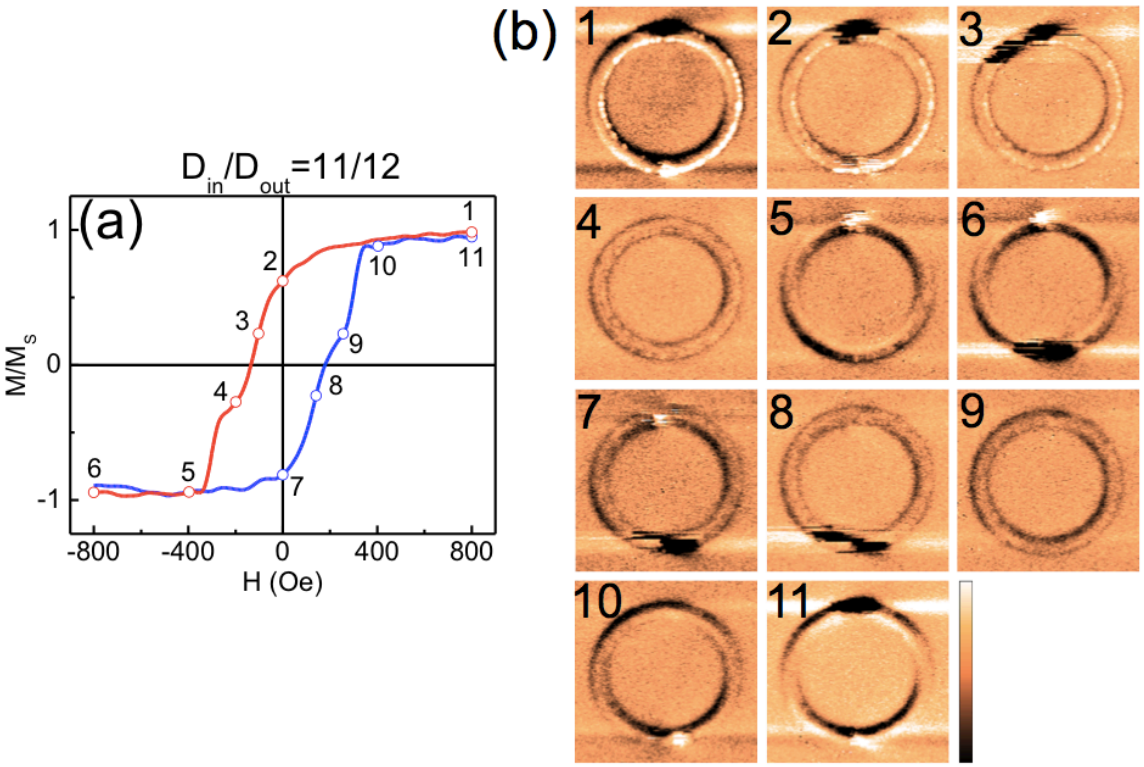

Figure 5.4 Selected MFM images showing the magnetic reversal process for Fe rings with D_{out}=2.4 m, t_{Fe}=10 nm, D_{in}/D_{out}=11/12.

The ascending branch [Figures 5.4(b6)-5.4(b11)] shows similar switching process of the ring. Starting from negative saturation [Figure 5.4(b6)], as the field decreases magnitude in the negative direction, the ring remains its domain configuration at remanence [Figure 5.4(b7)]. At +100 Oe, the top domain wall disappears and a multi-domain region is observed the ring bottom [Figure 5.4(b8)]. After its annihilation, the ring forms the vortex state [Figure 5.4(b9)]. As the field reaches +400 Oe, the magnetization direction of the ring is reversed into the positive direction [Figure 5.4(b10)]. Finally at +800 Oe, the ring is saturated in the positive direction again [Figure 5.4(b11)]. The magnetic reversal of the narrow Fe ring is first dominated by propagation and annihilation of the domain walls to form the vortex state, and then vortex state collapses to form the reversed saturated state.

For wide Fe ring with $D_{in}/D_{out}=1/12$, Figure 5.5 shows its magnetic domain configurations during magnetic switching process. At +800 Oe, as shown in Figure 5.5(b1), the ring is saturated in the positive direction, a black and a white area with dipolar contrast are observed at the edge of the ring along the field direction, indicating the formation of magnetic poles in a saturated single domain state. As the field decreases to +200 Oe, the areas of the dipolar contrast gradually shrink in size, which indicates the spins partially relax compared to the saturation state [Figure 5.5(b2)]. At remanence, as shown in Figure 5.5(b3), although the dipolar contrast still remains in the original positive direction, magnetic black and white contrast can also been observed on the ring structure, indicating the start of domain nucleation. At coercive field [Figure 5.5(b4)], the ring breaks into multi-domain state, as multiple magnetic contrasts are observed all over the ring surface. As the field decreases to -200 Oe, the magnetic contrast on the ring reverses its direction [Figure 5.5(b5)], which means the magnetization direction of the ring is reversed. At -800 Oe, the ring is saturated in the negative direction [Figure 5.5(b6)].

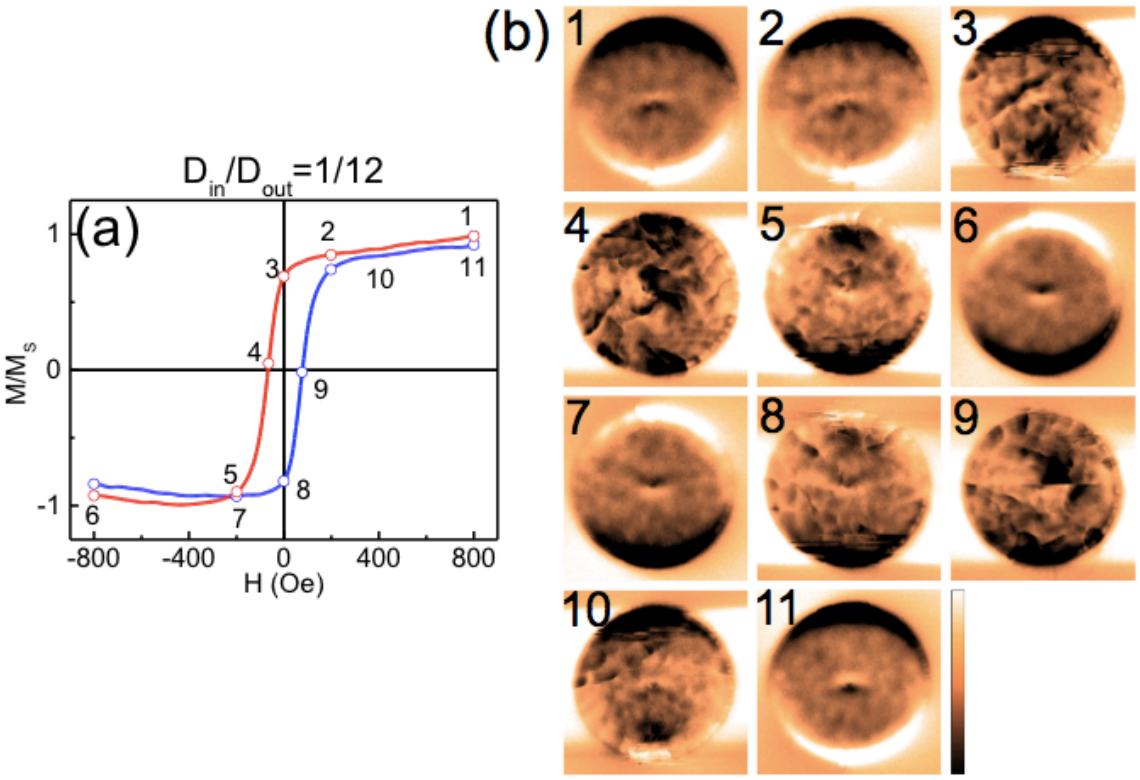

Figure 5.5 Selected MFM images showing the magnetic reversal process for Fe rings with D_{out}=2.4 m, t_{Fe}=10 nm, D_{in}/D_{out}=1/12.

For the ascending branch, the wide ring shows the same switching behavior. Starting from negative saturation [Figure 5.5(b6)], as the field increases to -200 Oe, the ring remains its domain configuration with reduced contrast area [Figure 5.5(b7)]. At remanence [Figure 5.5(b8)], although the magnetization remains in the negative direction, domain nucleation is observed on the ring structure. At the coercive field in the positive direction [Figure 5.5(b9)], the ring breaks into multi domain state during domain nucleation process. At +200 Oe, the magnetic contrast of the ring reverses into the positive direction [Figure 5.5(b10)]. When the field comes back to +800 Oe, the ring is saturated in positive direction again [Figure 5.5(b11)]. Therefore, the magnetic reversal

process of the wide Fe is dominated by one-step domain nucleation and growth, with no intermediate vortex state formed.

5.5 Micromagnetic simulation of the switching process

Micromagnetic simulations of the magnetic reversal process of the narrow D_{in}/D_{out}=10/12 ring and wide D_{in}/D_{out}=1/12 rings are performed using a Landau-Lifshitz-Gilbert micromagnetic solver. [64] The saturation magnetization and the exchange stiffness constant are set at the value of bulk Fe: M_s=*1714 emu/cm*^{3} and A=*12 uerg/cm*. The cell size is set to be 5×5×5 nm^3. [87] Figures 5.6(a)-5.6(d) show the domain configurations of narrow D_{in}/D_{out}=11/12 Fe ring. At positive saturation [Figure 5.6(a)], a head-to-head domain wall is observed at the top of the ring, while a tail-to-tail domain wall is observed at the bottom of the ring. As the field magnitude decreases, the tail-to-tail domain wall at the ring bottom moves up and annihilates with the top head-to-head domain wall [Figure 5.6(b)]. After the annihilation, the ring forms a vortex state [Figure 5.6(c)]. Further decreasing the field leads to the collapse of the vortex state, and the narrow ring forms the saturated state in the negative direction [Figure 5.6(d)]. The magnetization reversal process of the wide D_{in}/D_{out}=1/12 Fe ring is shown in Figures 5.6(e)-5.6(h). At positive saturation, the spins are aligned to the field direction to from the saturated single domain state [Figure 5.6(e)]. As the field decreases to zero, although the net magnetization of the ring is still in the positive direction, domain nucleation process starts, as red and green color domains can be observed to nucleate on the ring [Figure 5.6(f)]. At coercive field

[Figure 5.6(g)], the Fe ring breaks into multi-domain state. After this nucleation step, the Fe is saturated in the negative direction [Figure 5.6(h)].

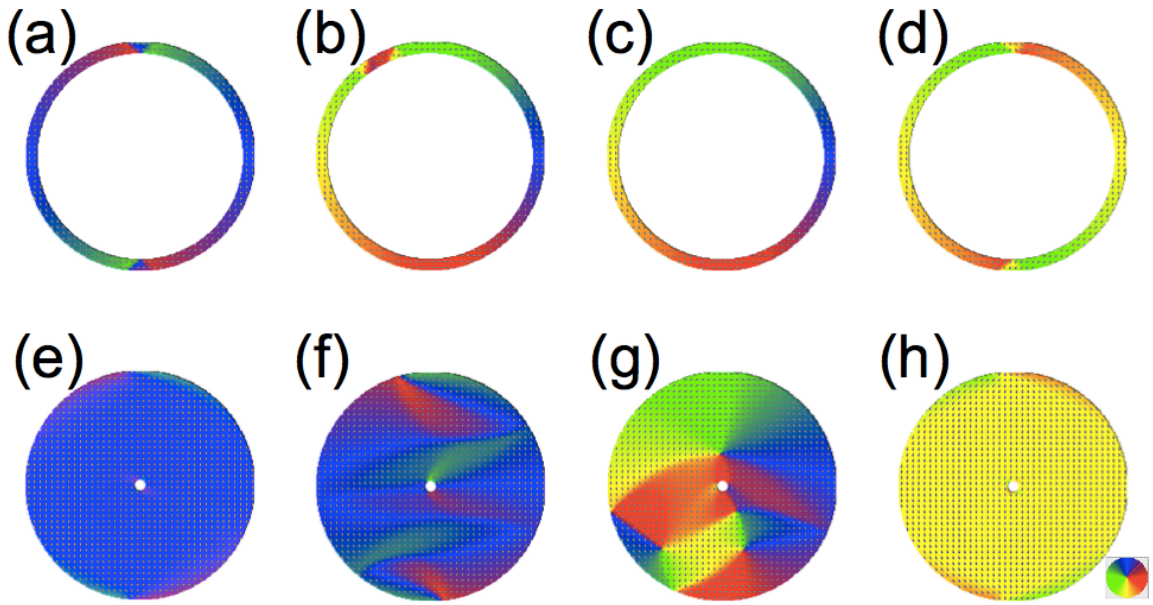

Figure 5.6 Micromagnetic simulated domain configurations of the $D_{in}/D_{out}=11/12$ and $D_{in}/D_{out}=1/12$ Fe ring in the magnetic reversal process. The in-plane magnetization direction is indicated by the color wheel or overlaid arrows.

5.6 Analytical model to explain the evolution trend as D_{in}/D_{out} changes

To explain the evolution from double-step to single-step switching as the D_{in}/D_{out} decreases (as ring widens up), micromagnetic simulations are used to calculate the energy densities of different magnetic remanence states for Fe ring with D_{out}=2400 nm, t_{Fe}=10 nm, while D_{in}/D_{out} increases from 1/12 to 11/12. The evolution of the energy density with D_{in}/D_{out} ratio is plotted in Figure 5.7.

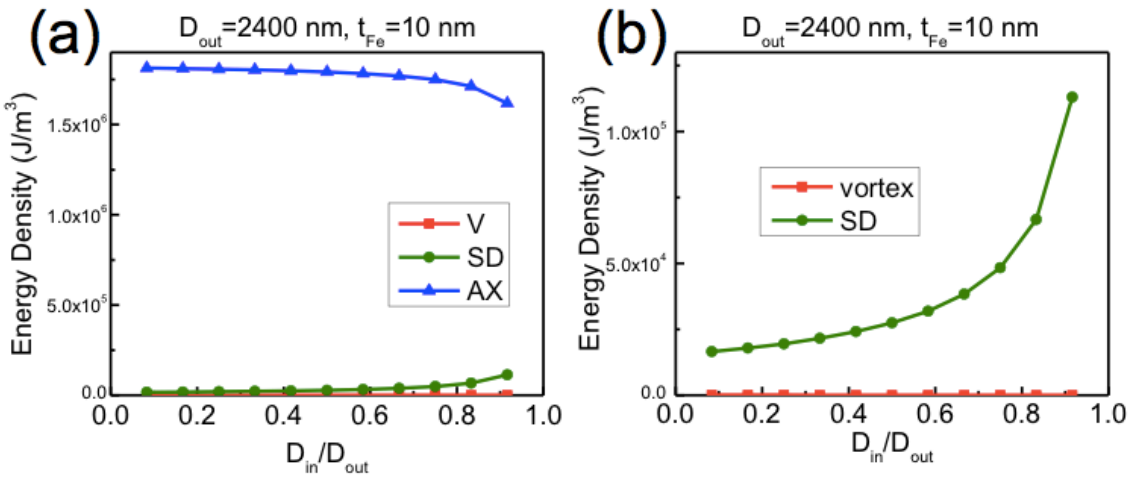

Figure 5.7 Micromagnetic simulated energy density of the vortex state, single domain state and axial state formed at remanence for Fe ring structures of (a) 100 nm (b) 300 nm (c) 1000 nm and (d) 2400 nm in diameter.

As Figure 5.7(a) shows, with the increase of the D_{in}/D_{out} ratio, the energy density of the vortex state slightly decreases, while the energy density of the single domain state increases and the energy density of the axial state decreases. Since the energy density of the axial state is much higher than the single domain state and the vortex state, a more detailed plot of the energy density of the single domain state and vortex state is shown in Figure 5.7(b). Although the energy density of the vortex state is smaller than single domain state, as the D_{in}/D_{out} ratio increases (ring narrows down), the energy gap between the single domain state and vortex state increases. This is why in narrow rings with larger D_{in}/D_{out} ratio, the vortex state is energetically more stable and the magnetic reversal prefers double-step switching.

5.7 Conclusion

We investigate the evolution of magnetic properties of the D_{out}=*2.4 μm*, t_{Fe}=*10 nm* Fe ring structures as the inner-to-outer diameter ratio, D_{in}/D_{out}, changes. We observe that with the D_{in}/D_{out} ratio of the ring decreasing, the magnetic hysteresis behavior of the ring evolves from double-step with vortex state in-between to single-step. This is explained by the increasing energy difference between vortex state and single domain state as D_{in}/D_{out} ratio increases.

5.8 Summary of the effect of geometry (D_{out}, t_{Fe}/D_{out} and D_{in}/D_{out}) on the magnetic properties of Fe rings

After discussing the effect of the thickness (Chapter 3), size (Chapter 4) and width (Chapter 5) on the magnetic behaviors of the lithographically patterned Fe rings, we want to summarize how these 3 geometric parameters in this section of the thesis. As the thickness t_{Fe} increase, or the outer diameter D_{out} decrease, or inner-to-outer diameter ratio D_{in}/D_{out} increase, the *M-H* hysteresis loop of the Fe ring evolve from single-step to double-step, with the remanent magnetic state evolving from quasi-saturated state to vortex state. All these evolution in hysteresis behavior and remanent state can be explained by comparing the energy density of three typical magnetic remanence state as shown in Figure 3.7: (1) vortex state (2) single-domain state and (3) axial state. Here, we again use micromagnetic simulation to reveal how the energy density of these 3 states evolve with the 3 geometric parameters (D_{out}, t_{Fe}/D_{out} and D_{in}/D_{out}), as shown in Figure 5.8:

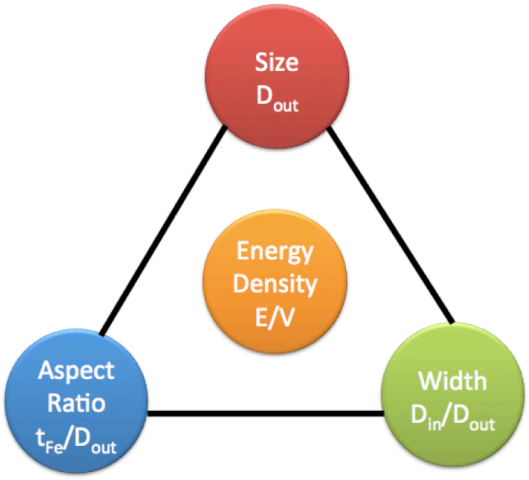

Figure 5.8 Three geometric parameters that determine the energy density (E/V) of a magnetic state in the lithographically patterned Fe rings: the size (D_{out}), aspect ratio (t_{Fe}/D_{out}) and width (D_{in}/D_{out}).

The energy density of the vortex state is dependent on the ring size D_{out} and width (D_{in}/D_{out}), but independent of the aspect ratio (t_{Fe}/D_{out}), as shown in Figure 5.9. In Figure 5.9(a), the energy density of the vortex state monotonically decreases with D_{in}/D_{out}. Figure 5.9(b) shows the energy density of the vortex state also decreases with the ring size (D_{out}).

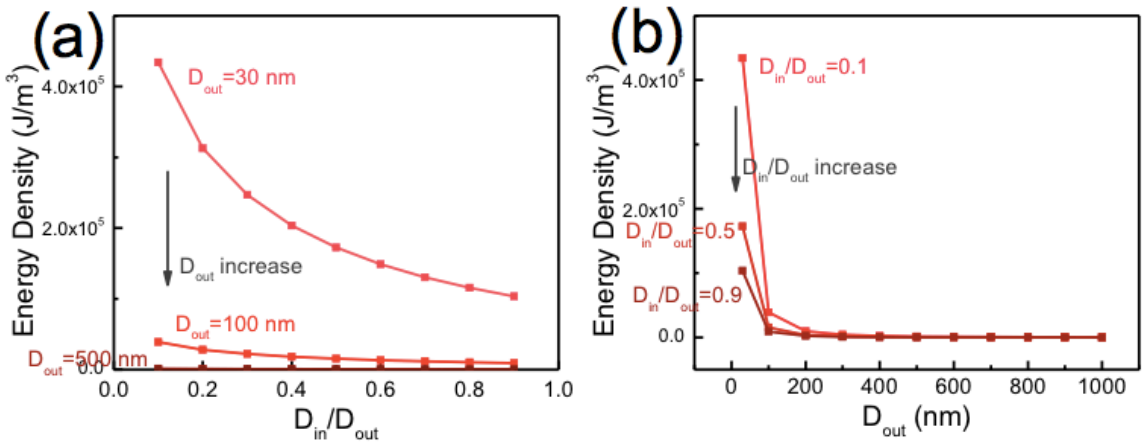

Figure 5.9 (a) Energy density of the vortex state as a function of the D_{in}/D_{out} ratio. The arrow points to the direction that D_{out} increases. (b) Energy density of the vortex state as a function of the D_{out}. The arrow points to the direction that D_{in}/D_{out} increases.

The energy density of the single-domain state and axial state is dependent on the aspect ratio (t_{Fe}/D_{out}) and inner-to-outer diameter ratio (D_{in}/D_{out}) of the ring, but independent of ring size (D_{out}). As shown in Figure 5.10, the energy density of the single domain state increases monotonically with D_{in}/D_{out} [Figure 5.10(a)] and t_{Fe}/D_{out} [Figure 5.10(b)].

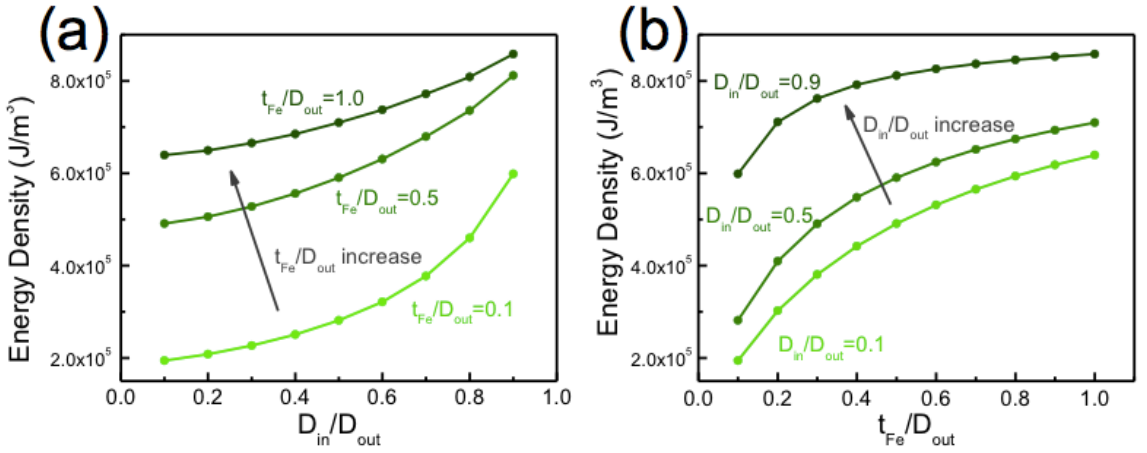

Figure 5.10 (a) Energy density of the single-domain state as a function of the D_{in}/D_{out} ratio. The arrow points to the direction that t_{Fe}/D_{out} increases. (b) Energy density of the single-domain state as a function of the t_{Fe}/D_{out}. The arrow points to the direction that D_{in}/D_{out} increases.

The energy density of the axial state, however, shows the opposite trend as the single-domain state. As shown in Figure 5.11, the energy density of the axial state decreases monotonically with D_{in}/D_{out} [Figure 5.11(a)] and t_{Fe}/D_{out} [Figure 5.11(b)].

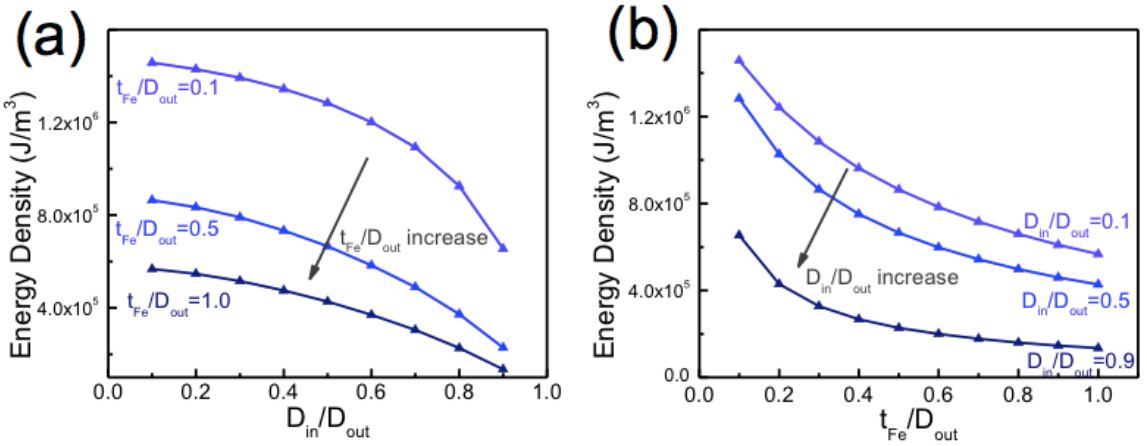

Figure 5.11 (a) Energy density of the axial state as a function of the D_{in}/D_{out} ratio. The arrow points to the direction that t_{Fe}/D_{out} increases. (b) Energy density of the axial state as a function of the t_{Fe}/D_{out}. The arrow points to the direction that D_{in}/D_{out} increases.

Therefore, if we plot the energy density of the vortex state, single-domain state and axial state as a function of the ring size D_{out}, we get Figure 5.12.

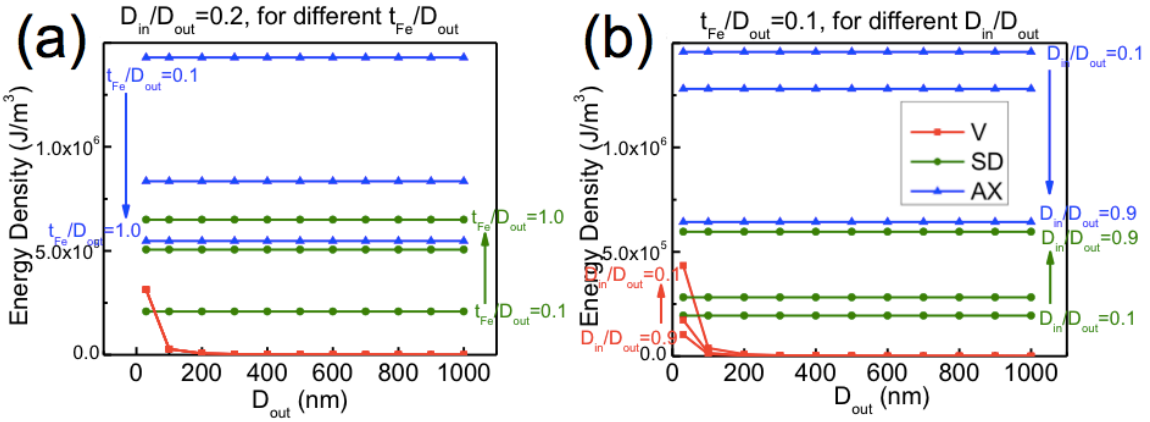

Figure 5.12 (a) Energy density of the remanence states as a function of D_{out} when D_{in}/D_{out}=0.2. The arrow points to the direction that t_{Fe}/D_{out} increases. (b) Energy density of the remanence states as a function of D_{out} when t_{Fe}/D_{out}=0.1. The arrow points to the direction that D_{in}/D_{out} increases.

As shown in Figure 5.12, the energy density of the vortex state decreases with D_{out}, while the energy density single-domain state and axial stay constant as D_{out} changes.

The energy density of the 3 remanence states as a function of the ring width D_{in}/D_{out} is shown in Figure 5.13.

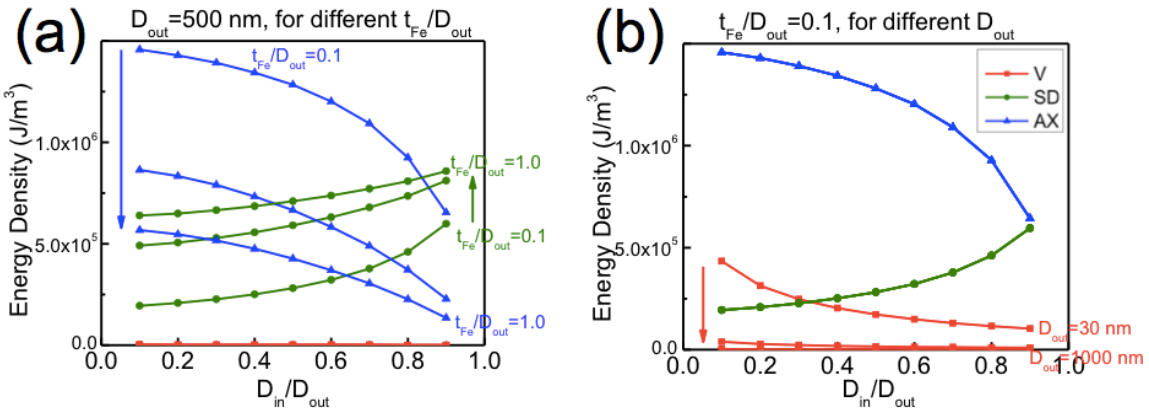

Figure 5.13 (a) Energy density of the remanence states as a function of D_{in}/D_{out} when D_{out}=500 nm. The arrow points to the direction that t_{Fe}/D_{out} increases. (b) Energy density of the remanence states as a function of D_{in}/D_{out}, when t_{Fe}/D_{out}=0.1. The arrow points to the direction that D_{out} increases.

As shown in Figure 5.13, while the energy density of the vortex state and axial state decrease with D_{in}/D_{out}, the energy density of the single domain state increases with D_{in}/D_{out}. Therefore, the narrower ring (larger D_{in}/D_{out}) prefers the formation of the vortex state.

Finally, the energy density of the 3 remanence states as a function of the ring's aspect ratio t_{Fe}/D_{out} is shown in Figure 5.14.

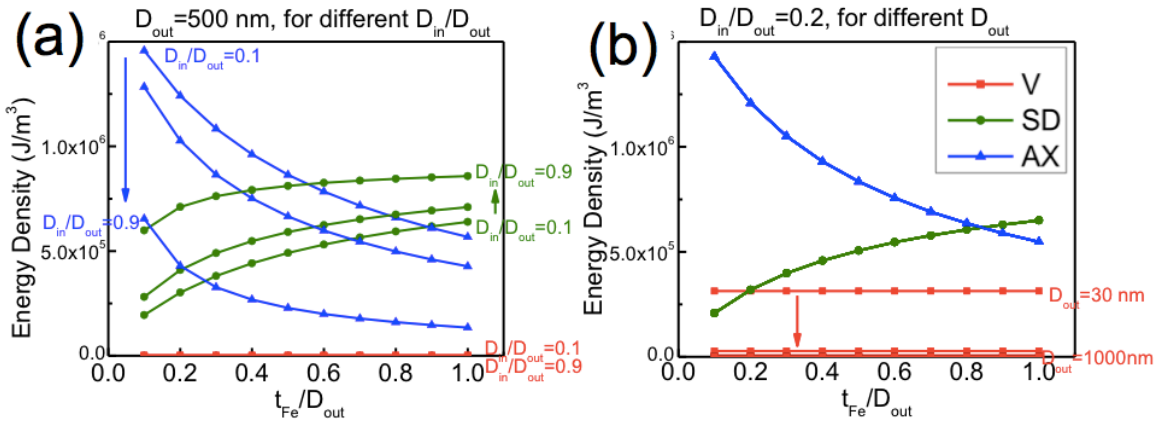

Figure 5.14 (a) Energy density of the remanence states as a function of t_{Fe}/D_{out} when D_{out}=500 nm. The arrow points to the direction that D_{in}/D_{out} increases. (b) Energy density of the remanence states as a function of t_{Fe}/D_{out}, when D_{in}/D_{out}=0.2. The arrow points to the direction that D_{out} increases.

As shown in Figure 5.14, the energy density of the single domain state increases with t_{Fe}/D_{out}, while the energy density of the axial state decrease with t_{Fe}/D_{out}. The energy density of the vortex state, however, remains constant as t_{Fe}/D_{out} changes. Therefore, as the t_{Fe}/D_{out} increase, the energy minimum state evolves from single domain state to vortex state and further to axial state.

The detailed energy density of the vortex state, single-domain state and axial state are discussed in Appendix C.

Chapter 6

MAGNETIC PROPERTIES OF EXCHANGE-BIASED IrMn/Fe RING STRUCTURES[§]

6.1 Anisotropic reversal modes in thin exchange-biased IrMn/Fe(10 nm) ring structures

From Chapter 3 to Chapter 5, we discuss the magnetic properties of the lithographically patterned Fe ring structures. In order to control the magnetic states and the switching process of ring structures, many variations have been made to the ring shapes, for example, by introducing notches or flat edges to the ring [88], decentering the ring [89] or even altering the shape of the rings into triangles or squares [90, 91]. The effect of magnetocrystalline anisotropy on the rings has also been studied in epitaxial ring structures [92]. Alternately, exchange bias (EB), which refers to the shift of the hysteresis loop in the magnetic field direction, can also serve as a tunable source of unidirectional anisotropy to tailor the magnetic properties of rings. So far, very little effort has been devoted to the study of such exchange-biased rings [93,94,95]. Exchange bias induced asymmetric magnetization behavior along the bias direction has been observed in magnetic ring structures [96], but the detailed mechanism of magnetic reversal is not well understood. In this section, magnetization reversal mechanism of $D_{out}=2.4\ \mu m$ exchange biased IrMn/Fe rings is studied using angular dependent magneto-optical Kerr effect (MOKE) magnetometry, magnetic force microscopy (MFM) and micromagnetic

[§] The content of this chapter has been published as
[1] Yu-Feng, Hou and K. M. Krishnan, "Magnetization reversal in exchange biased IrMn/Fe ring arrays ", *Appl. Phys. Lett.* **98**, 042510 (2011).

[2] Yu-Feng, Hou and K. M. Krishnan, "Thickness-dependent magnetization reversal behavior of lithographic IrMn/Fe ring structures", *J. Appl. Phys.* **111**, 07B905 (2012).

simulations. The results are also compared with the unbiased Fe rings. Drastically different magnetic reversal mechanisms are observed in the exchange biased rings when the field is applied either along or perpendicular to the bias direction. Micromagnetic simulations are performed to reveal the spin configurations of the exchange-biased rings during the reversal process for these two field orientations.

Arrays of circular Ta (1 nm)/Cu (5 nm)/IrMn (10 nm)/Fe (10 nm)/Ta (3 nm) multilayer rings with inner and outer diameters D_{in}/D_{out}=*0.8 μm /2.4 μm* and inter-ring distance 3 μm, as schematically displayed in Figure 6.1(a), are fabricated on Si/SiO_2 substrates via a mask-transferred lithographic process, described in Chapter 3 in detail [97]. The two bottom layers, Ta (1 nm)/Cu (5 nm), serve as seeding layers to induce the (111) texture growth of IrMn [98]. A 3 nm thick Ta capping layer is deposited on the top to protect the whole structure from oxidation. Figure 6.1(b) shows scanning electron microscope (SEM) images of the multilayer ring arrays and a detailed view of a single ring.

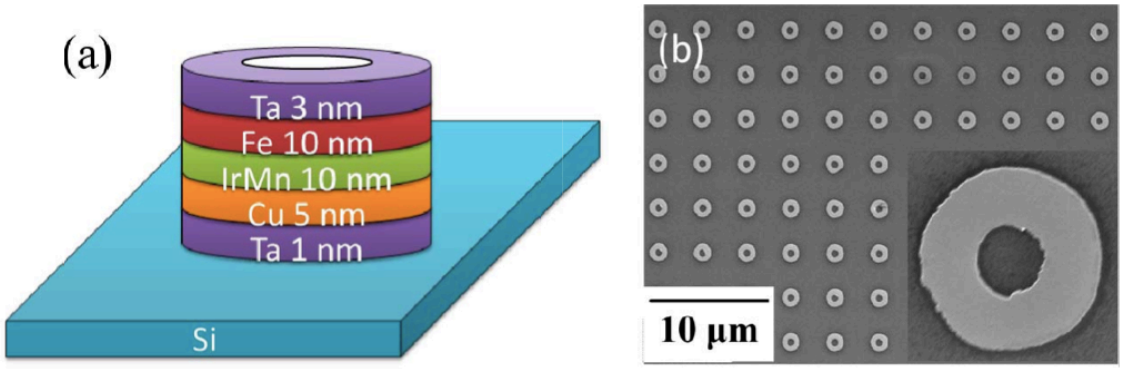

Figure 6.1. (a) Schematic of 2.4 μm Ta (1 nm)/Cu (5 nm)/IrMn (10 nm)/Fe (10 nm)/Ta (2 nm) ring arrays. (b) A scanning electron micrograph (SEM) of the sample. The outer and inner diameters of the ring are 2.4 μm and 0.8 μm, respectively, with an inter-ring distance of 3 μm.

In order to introduce an exchange bias, the as-prepared sample is heated to 600 K in vacuum and then cooled to room temperature under an external field of 200 Oe applied in the surface plane of the sample. To facilitate the understanding of the effect of exchange bias, another reference sample without the antiferromagnetic layer, i.e., Ta (1 nm)/Cu (5 nm)/Fe (10 nm)/Ta (3 nm), is also prepared in the same process.

Magnetic Hysteresis Behavior of IrMn/Fe(10 nm) EB ring structures

M-H hysteresis loops of both exchange-biased and unbiased ring samples are subsequently measured at room temperature with an in-plane applied magnetic field, using a longitudinal MOKE setup. To improve the signal-to-noise ratio, each loop is obtained by averaging the measured results over 20 times. The hysteresis loop of the unbiased Fe rings is shown in Figure 6.2(a). The red and the blue curves represent the descending and the ascending branches of the loop, respectively. No significant differences in the shape of the hysteresis loop are observed when measuring along different directions of the sample, indicating that the intrinsic magnetocrystalline anisotropy of Fe and the dipolar interactions among rings are negligible. The experimentally measured coercivity of the unbiased ring is 75 Oe. For exchange-biased rings, the hysteresis behavior is measured with the magnetic field applied at different angles, θ, with respect to the bias direction. Figures 6.2(b) and 6.2(c) are the hysteresis loops of IrMn/Fe exchange biased rings measured along $\theta = 0°$ and $90°$, respectively.

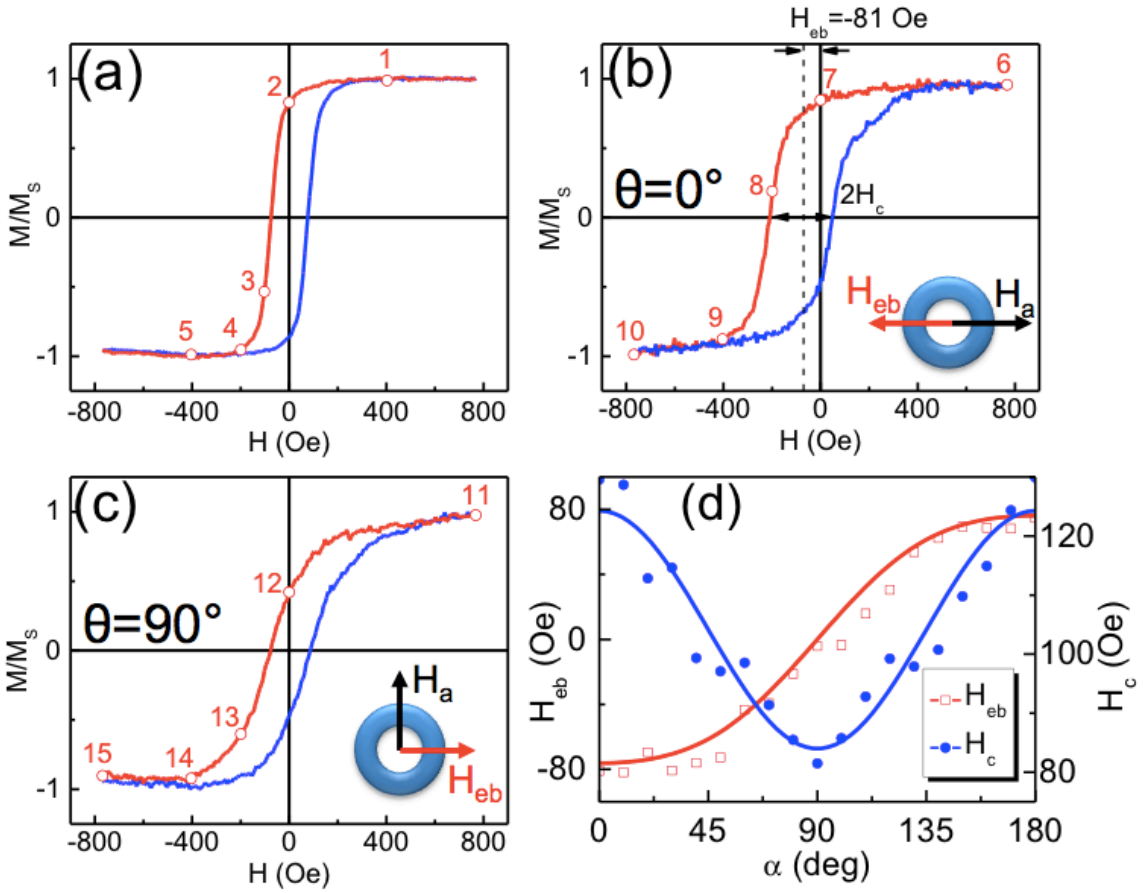

Figure 6.2 *M-H* hysteresis loops of (a) the unbiased Fe ring arrays, and the exchange biased ring arrays with the field applied (b) along and (c) perpendicular to the bias direction. (d) The exchange bias H_{eb} and the coercivity H_c of exchange-biased rings as a function of the field orientation θ.

When the field is applied along the bias direction (i.e., $\theta = 0°$), the hysteresis loop possesses a similar shape as that of the unbiased Fe rings, with a higher coercive field ($H_c = 130$ *Oe*) and a shift ($H_{eb} = -81$ *Oe*) of the loop in the negative field direction due to the interfacial exchange coupling between Fe and IrMn layers. The hysteresis loop measured perpendicular to the bias direction (i.e., $\theta = 90°$), exhibits a coercivity of 81 Oe but no exchange bias. This indicates that during the field cooling procedure, the interfacial uncompensated spins of the antiferromagnetic layer are effectively aligned in the field direction, thus exerting a unidirectional anisotropy on the ferromagnetic layer due to the

interfacial exchange coupling. The angular dependence of both the exchange bias $H_{eb}(\theta)$ and the coercivity $H_c(\theta)$ on this field orientation, θ, is studied via a series of measurements varying θ from 0° to 180° in steps of 10°. The values of $H_{eb}(\theta)$ and $H_c(\theta)$ are obtained at each θ value and the results are shown in Figure 6.2(d). $H_{eb}(\theta)$ shows a unidirectional symmetry about the bias direction, i.e., $H_{eb}(\pi+\theta)= -H_{eb}(\theta)$. However, $H_c(\theta)$ exhibits a two-fold uniaxial symmetry about the bias axis, i.e., $H_c(\pi+\theta)=H_c(\theta)$. Considering the symmetry of the magnetic anisotropy energy [99], the value of $H_{eb}(\theta)$ and $H_c(\theta)$ can be described by Fourier cosine series with odd and even terms, respectively. That is, $H_{eb}(\theta)=H_{eb}(0)\Sigma_{n=odd}b_n cos(n\theta)$ and $H_c(\theta)=H_c(0)\Sigma_{n=even}b_n cos(n\theta)$. For our samples, the numerical fitting results show the exchange bias follows the simple cosine relation: $H_{eb}(\theta)= -81\ Oe\ cos(\theta)$, which results directly from the unidirectional anisotropy caused by exchange bias, and the coercivity follows the relation: $H_c=104\ Oe\ [1+ 0.2cos(2\theta)]$, which indicates that the exchange bias induces a collinear uniaxial anisotropy as well

Magnetic reversal process of the 10 nm EB & NB ring structures:

The magnetic domain configurations of the samples are investigated by MFM with magnetic field applied parallel to the sample surface, using 45 nm CoPt/FePt coated high coercivity probes with a lift height of 30 nm. Figures 6.3(a)-6.3(c) shows selected MFM images measured at the nominal values of magnetic fields as marked in Figures 6.2(a)-6.2(c). Since no significant asymmetry in the magnetization reversal is observed with increasing or decreasing field, we only display the images at different points of the ascending branch. Figure 6.3(a) shows the MFM images for the unbiased Fe rings vary

from the negative to positive saturation, corresponding to the ascending branch in Figure 6.2(a). For Figure 6.3(a1), the applied field is -400 Oe and the ring is negatively saturated. A black and a white area with dipolar contrast are observed at the edge of the ring along the field direction, indicating the formation of magnetic poles in a saturated single domain state. Figures 6.3(a2)-3(a5) correspond to the applied field value of 0 Oe, 100 Oe, 200 Oe, and 400 Oe, respectively. As the field increases, the areas of the dipolar contrast gradually shrink in size, which indicates the elimination of the ferromagnetic domain in the negative field direction and the creation of the domain aligned along the positive direction, until the field reverses its direction to positive. After the field exceeds the coercivity and reaches 200 Oe, the dipolar contrast on the ring is suddenly reversed in the direction with much weaker strength [Figure 6.3(a4)]. Upon further increasing the field in the positive direction, the reversed dipolar contrast is strengthened and saturated at 400 Oe [Figure 6.3(a5)]. The series of images in Figure 6.3(a) indicates that the magnetization reversal of the unbiased ring is dominated by the nonuniform domain nucleation.

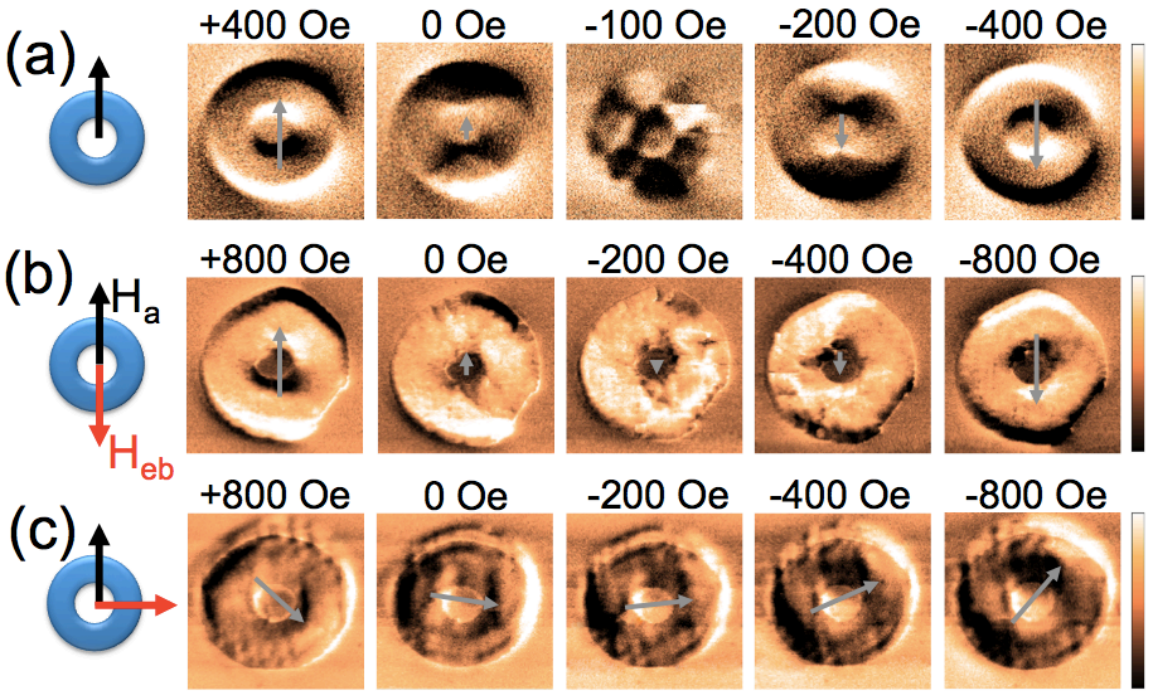

Figure 6.3 Selected MFM images showing the magnetic reversal process for (a) the unbiased Fe rings at marked field values. Magnitude and direction of the magnetization is marked by the grey arrows on the ring. For the exchange biased rings (b) along the field cool direction at marked field values. (c) Perpendicular-to-bias direction. The corresponding magnetic field values are the same as in (b). However, the images show that the exchange bias ensures that there is always a significant component of the magnetization along H_{eb}.

Figure 6.3(b) illustrates the magnetic reversal process of the exchange-biased ring when the field is applied along the bias direction, which corresponds to the ascending branch of the hysteresis loop in Figure 6.2(b). In Figures 6.3(b6)-6.3(b10), the applied field is varied from -800 Oe to 800 Oe. Similar to the unbiased ring, the dipolar contrast observed at negative saturation [Figure 3(b6)] fades progressively as the field approaches the coercivity, and abruptly switches its direction at positive 400 Oe [Figure 6.3(b8)], and gets enhanced and positively saturated at 800 Oe [Figure 6.3(b10)]. The MFM results indicate the magnetic reversal mechanism in the exchange-biased ring for the field applied along the field cool direction remains the same as the unbiased Fe ring.

However, Figure 6.3(c) reveals that the magnetic reversal mode, when the applied field is perpendicular to the bias direction (i.e. $\theta=90°$) is drastically different. As the field is increased from the negative saturation and then reversed the magnetization direction as depicted by the axis of the dipolar contrast slowly rotates to the bias direction, and then to the positive saturation, as shown in Figure 6.3(c11)-6.3(c15). The rotation of the dipolar contrast implies that the magnetization of the rings roughly remains in its single domain state but rotates from the negative to the positive saturation with increasing field. That is to say, the magnetic reversal mechanism for the exchange-biased ring measured perpendicular to the bias direction is dominated by coherent rotation, which is significantly different from the measurement along the exchange bias.

Micromagnetic Simulations of the Different Magnetic Reversal Process for the EB Rings

Micromagnetic simulations of the magnetic reversal process of exchange-biased rings are performed both along the bias direction ($\theta=0°$) and perpendicular to the bias direction ($\theta=90°$), using the LLG micromagnetic simulator [64]. The saturation magnetization and the exchange stiffness constant of the Fe layer are set at the value of bulk Fe: $M_s=1714$ *emu/cm*^{3} and $A=12$ μ*erg/cm*. The cubic magnetocrystalline anisotropy with randomly distributed easy axes is assigned to each of the 5×5×5 nm^3 cells of Fe due to the polycrystalline structure of Fe ring layer. The exchange bias field arising from the interface exchange coupling between IrMn and Fe layers is simulated as an additional static field of magnitude H_{eb} = *-81 Oe*, applied in the direction of $\theta=0°$. In Figure 6.4, the first row shows the simulated magnetization reversal process for $\theta=0°$, while the second

row shows the case for $\theta=90°$. The magnetization direction is indicated by the color wheel and the overlaid arrows.

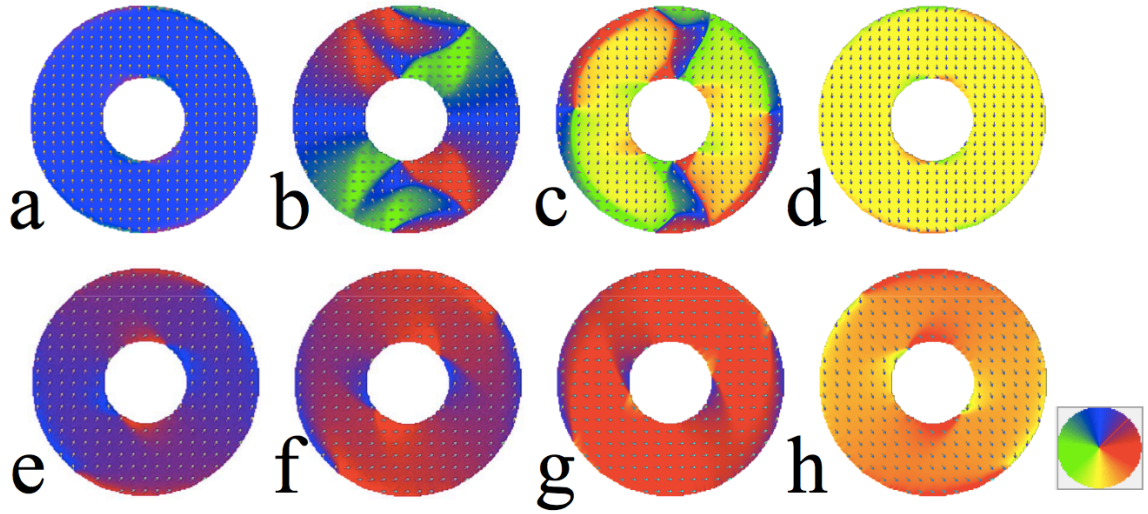

Figure 6.4 Micromagnetic simulated spin configurations of the exchange biased ring in the magnetic reversal process (a)-(d) along the bias direction, and (e)-(h) perpendicular to bias direction. The magnetization direction is indicated by the color wheel or overlaid arrows.

In Figure 6.4(a), the ring is magnetically saturated in the negative field direction. As the field increases, magnetic domains along other directions start to nucleate, as shown by the red and green regions in Figure 6.4(b). Finally, the magnetic domains of the positive direction expand over others [Figure 6.4(c)], and reach the positive saturation in Figure 6.4(d). The simulation results confirm the nucleation and growth observed in MFM imaging. When the external field is perpendicular to the bias direction, as the field increases from negative saturation, the ring remains in its single domain state with the dipole direction gradually rotating from the negative field direction [Figure 6.4(e)] to the bias direction [Figure 6.4(g)], and finally reaches the positive saturation [Figure 6.4(h)].

Effective Field Model

The differences in magnetic reversal modes at different field orientation could be qualitatively explained by an effective field model developed by Beckmann et al [100]. This model considers three contributions to the effective field H_{eff} acting on the ferromagnetic layer during the process of magnetic reversal. They are the unidirectional exchange field, H_E, in the field-cool direction, the external magnetic field, H_a, and the uniaxial anisotropy field, H_U. In the case of $\theta=0°$, the exchange bias field and the anisotropy field are collinear with the applied field, thus the effective field is aligned with the magnetization, which favors the domain nucleation mode for the magnetization reversal. In the case of $\theta=90°$, the external magnetic field, H_a, is perpendicular to the exchange field, H_{eb}, and the anisotropy field, H_u. Thus, the effective field has a large angle with respect to the magnetization, which lies in the easy direction given by H_{eb} and H, leading to a strong torque that favors the coherent rotation mode of magnetic reversal.

6.2 Evolution of Magnetic Properties in EB IrMn/Fe Ring Structures with Fe Layer Thickness

We discuss the effects of the exchange bias interfacial coupling on the magnetic switching behavior of thin IrMn/Fe (10 nm) ring structures in section 6.1. In this section, we investigate the effect of the exchange-bias when the Fe layer thickness, t_{Fe}, increases. $D_{out}=2.4\ \mu m$ EB IrMn/Fe ring structures with systematic thickness variation of the Fe layer are fabricated and the evolution of their magnetization reversal mechanism is studied using magneto-optical Kerr effect (MOKE) magnetometry. We observe that the

magnetization reversal in EB ring structures is significantly modified due to EB. The evolution in EB field, H_{eb}, is also investigated as a function of the Fe layer thickness.

IrMn/Fe exchange biased ring arrays with the thickness for IrMn, t_{IrMn}, fixed at 10 nm and for Fe, t_{Fe}, varying from 10 to 80 nm, are patterned on thermally oxidized Si substrates via a mask-transfer lithographic process. [101] First, 1 μm thick polymer resist ring arrays are fabricated on the substrate by photolithography. Then, a 170 nm thick Mo sacrificial layer is deposited onto the resist ring patterns in an ion beam sputtering system, with a base pressure of 1×10^{-8} torr and followed by ultrasonic assisted chemical lift-off of the resist rings. This step creates Mo anti-ring patterns on the substrate. Finally, multilayers with structure Ta (1 nm)/Cu (5 nm)/IrMn (10 nm)/ Fe (t_{Fe} nm)/Ta (3 nm) are sputtered onto the Mo anti-ring pattern obtained in the previous step, and then Mo is etched away by H_2O_2 solution, leaving only multilayer ring arrays on the substrate, the structure of the EB ring is shown in Figure 6.5(a).

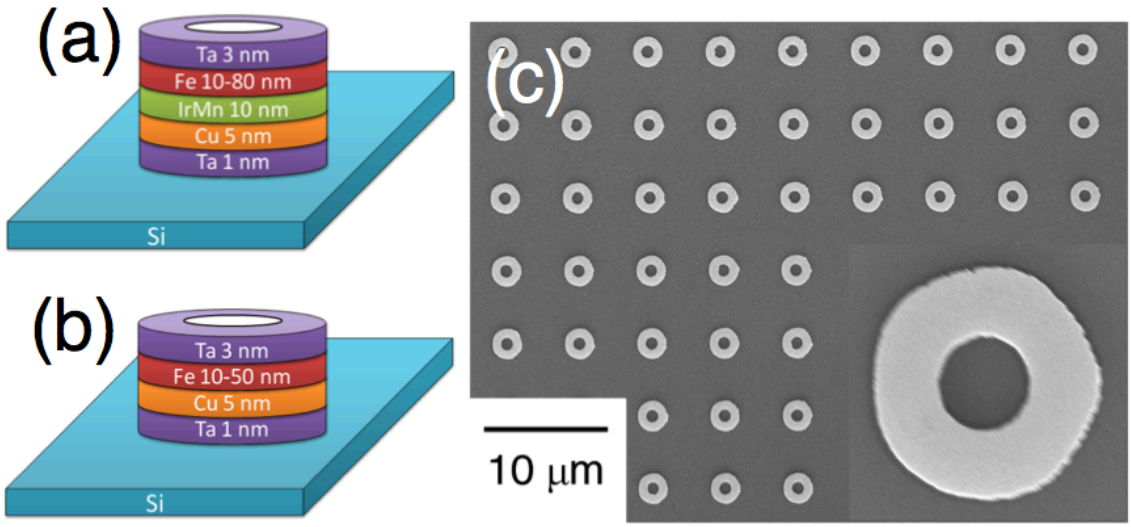

Figure 6.5 (a) Schematic structure of the multilayer EB IrMn/Fe ring arrays. (b) Schematic structure of the multilayer unbiased Fe ring arrays. (c) Scanning electron microscopic images of the sample. A detailed image of one ring is shown on the bottom right corner.

The two bottom layers, Ta (1 nm)/Cu (5 nm), are employed as seed layers to favor [111] texture of IrMn. [98] A 3 nm Ta capping layer is deposited on the top to protect the whole structure from oxidation. In order to introduce an EB, the as-prepared sample is heated to 600 K in vacuum and then cooled to room temperature under an external field of 200 Oe applied in the sample surface plane by a small permanent magnet placed at the back of the sample. To facilitate the understanding of the effect of EB, another set of reference samples without the antiferromagnetic layer, i.e. Ta (1 nm)/Cu (5 nm)/Fe (t_{Fe} nm)/Ta (3 nm), are also prepared in the same process, as shown in Figure 6.5(b). Figure 6.5(c) shows scanning electron microscope images of the multilayer ring arrays and a detailed view of a single ring. Both the exchange biased and unbiased rings show a circular shape with outer/inner diameter D_{in}/D_{out}=*0.8 μm/2.4 μm*, and inter-ring distance of 3 μm, which is large enough to ensure the dipolar interaction among rings are negligible.

M-H hysteresis loops of both exchange biased and unbiased ring samples are subsequently measured at room temperature using a magneto-optical Kerr effect (MOKE) setup with external field applied in a longitudinal geometry. To improve the signal-to-noise ratio, each loop is obtained by averaging the measured results over 20 times.

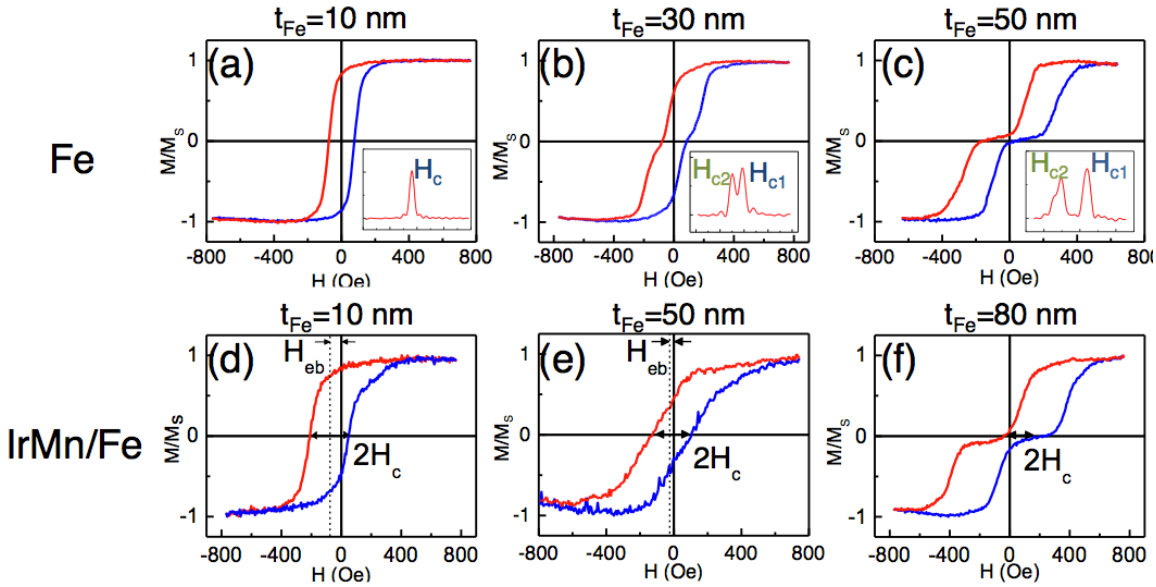

Figure 6.6 M-H hysteresis loops of unbiased Fe ring arrays with Fe layer thickness equals to (a) 10 nm (b) 30 nm and (c) 50 nm. The first order derivative *dM/dH* of the loop's descending branch (red) are plotted in the inset box located at the right bottom corner of each loop. Hysteresis loops of exchange biased IrMn/Fe rings with tFe equals to (d) 10 nm (e) 50 nm and (c) 80 nm are shown in the second row.

Hysteresis loops of the 10 nm [Figure 6.6(a)], 30 nm [Figure 6.6(b)] and 50 nm [Figure 6.6(c)] unbiased ring samples are chosen to show the complete evolution of the hysteresis behavior with thickness in unbiased Fe rings. The red and blue curves respectively represent the descending and ascending branches of the loop. The first order derivative, *dM/dH*, of the descending branch is plotted in the inset at the right bottom corner of each figure. The 10 nm unbiased ring shows a single step transition from positive saturation to negative saturation, at the measured coercivity of H_c = *-75 Oe*. The distribution of the

switching field, presented by the inset *dM/dH* curve, shows one sharp peak at the coercivity field, indicating the magnetization reversal is completed in one-step. The 50 nm biased ring, [Figure 6.6(c)], clearly shows a constricted shape with a two-step transition during magnetization reversal and zero remanence magnetization, which is typical for the vortex state. The corresponding *dM/dH* plots show two well separated peaks. The first switching field H_{c1}= *96 Oe*, corresponds to the switching from the positive saturated state to the vortex state. The second switching field H_{c2}= *-262 Oe*, corresponds to the switching from vortex state to the reversed saturated state in the negative direction. In between these two switching steps, the vortex state is stable from -28 Oe to -152 Oe. The representative behavior between these two limiting cases of 10 nm and 50 nm is shown for 30 nm ring in Figure 6.6(b). The *dM/dH* curve of the descending branch shows two distinct peaks, yet these two peaks are partially overlapping, which indicates that the second reversal step is initiated before the completion of the first step, and without a stable vortex state formed in between. Thus, for the unbiased ring, as the thickness of the Fe layer increases from 10 nm to 50 nm, the hysteresis loop evolves from single-step to double-step, with the transition taking place somewhere between 10 nm to 30 nm.

For exchange biased rings [Figures 6.6(d)-6.6(f)], the ultra thin 10 nm sample [Figure 6.6(d)] also shows a single step transition with a higher coercivity (H_c=*130 Oe*) and a shift of the loop in the negative field direction, H_{eb}=*-81 Oe*, due to the interfacial exchange coupling between Fe and IrMn layer. As the thickness of the Fe layer, t_{Fe}, increases to 50 nm, the hysteresis loop shows a tilted shape with a wide one-step transition centered at, the shift of the loop H_{eb} has decreased to H_{eb}=*-5.2 Oe*. Further

increase of the thickness of the Fe layer to 80 nm, causes the shift of the loop to become too small to be detected and the hysteresis loop evolves into double-step. Thus, compared to the unbiased sample, the hysteresis loops of the exchange biased ring also shows a single-step to double-step transition as t_{Fe} increases, but the transition thickness is shifted higher between 50 nm to 80 nm.

The increase of transition thickness in EB samples could be interpreted by analyzing the magnetic anisotropy induced by the exchange bias on the ring structure. The induced magnetic anisotropy, which consists of a unidirectional component H_E and a collinear uniaxial component H_U, is studied by measuring the angular dependence of the exchange bias field H_{eb} and then numerically fitted with an improved effective field model. In the measurements, the magnetic field is applied at an angle θ, varying from 0° to 360°, at a step size of 10°, with respective to the bias direction ($\theta = 0°$). The exchange bias field H_{eb} is obtained at each θ value and organized and shown in Figure 6.7(a).

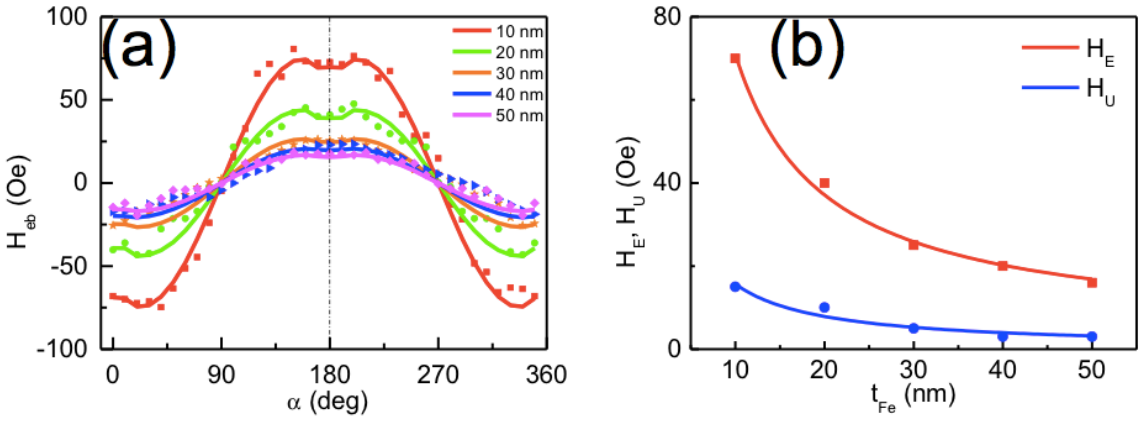

Figure 6.7 (a) Experimental exchange biased field (symbols) as a function of the field orientation θ and the numerical fitting (continuous line). (b) The anisotropy fields H_E and H_U obtained from the fitting for the angular dependence of H_{eb} for EB IrMn/Fe rings with different t_{Fe}.

As shown in this Figure 6.7(a), in EB ring samples, the exchange bias field $H_{eb}(\theta)$ shows a unidirectional symmetry about the bias direction, i.e., $H_{eb}(\pi+\theta) = -H_{eb}(\theta)$, and shows a maximum value away from the exchange bias axis ($\theta=180°$), due to the existence of the collinear uniaxial anisotropy H_U. To reveal the magnitude of the unidirectional anisotropy H_E and uniaxial anisotropy H_U, the angular dependence of the exchange bias field H_{eb} is numerically fitted with an improved effective field model.

For our polycrystalline EB ring sample, the energy per unit volume of the system is given by

$$E = -M_S H cos(\theta - \alpha) - K_E cos\theta - K_U cos^2\theta \quad (6\text{-}1)$$

Where M_S is the saturation magnetization, H is the applied field. θ and α are the angles between the anisotropy direction and the magnetization and the applied field direction, respectively. The parameters K_E and K_U are determined by $K_E = H_E M_S$ and $K_U = \frac{1}{2} H_U M_S$, where H_E and H_U are the unidirectional and uniaxial anisotropy field.

To obtain the equilibrium position of the magnetization, we let $\frac{\partial E}{\partial \theta} = 0$ and $\frac{\partial^2 E}{\partial \theta^2} > 0$, which gives us

$$M_S H sin(\theta - \alpha) + K_E sin\theta + K_U sin2\theta = 0 \quad (6\text{-}2)$$

$$M_S H cos(\theta - \alpha) + K_E cos\theta + 2K_U cos2\theta > 0 \quad (6\text{-}3)$$

Solve (6-2) for H, we get

$$H(\theta) = \frac{K_E sin\theta + K_U sin2\theta}{sin(\alpha - \theta)} \quad (6\text{-}4)$$

The hysteresis loop for a specific α value is thus obtained by plot $H(\theta) \sim M_S cos(\alpha-\theta)$. By letting α varying from 0° to 360°, we are able to calculate the angular dependence behavior of the exchange bias field H_{eb} for a given (K_E, K_U) value and compare it with the measured data. The results of the numerical fitting of the anisotropy fields are shown in Figure 6.7(b).

As shown in Figure 6.7(b), the fitted values of the unidirectional anisotropy, H_E and the collinear uniaxial anisotropy, H_U, decreases inversely with the Fe layer thickness, following the $1/t_{Fe}$ dependence.

The unidirectional anisotropy H_E causes the hysteresis loop of the EB sample to shift in the negative field direction, while the uniaxial anisotropy H_U, changes the shape of the hysteresis loop in EB ring samples. In unbiased Fe rings, the major difference for the single-step switching and double-step switching in ring structure is the remanence state. While in typical single-step switching, the ring remains a quasi-uniform state, in double-step switching process, the ring forms a vortex state. In EB rings, the uniaxial anisotropy induced by the exchange bias increases the energy density of forming the vortex state by $1/2K_U$, while the energy density of the quasi-uniform state stays the same (because spins are aligned with the easy axis). Thus, compared to unbiased Fe rings, EB rings with the induced uniaxial anisotropy prefer single-step switching during reversal. However, as the thickness of the Fe layer increase, the strength of the uniaxial anisotropy will decreases and become negligible [Figure 6.7(b)], and then the thick EB ring will show double-step switching again, as we observed in Figures 6.6(d)-6.6(f).

6.3 Conclusion

In summary, we systematically study the effects of exchange bias (EB) on the magnetization reversal behaviors in lithographic IrMn/Fe rings and their unbiased Fe counterparts, with the thickness of the Fe layer, t_{Fe}, varying from 10 nm to 80 nm. It is shown that, in thin IrMn/Fe (10 nm) EB rings, EB induces anisotropic reversal modes in the ring structure. When external field is applied along the bias direction, magnetic reversal of the ring is dominated by domain nucleation and growth. When external field is applied perpendicular to the bias direction, magnetic reversal is dominated by coherent rotation. As t_{Fe} increases, the hysteresis loops of both unbiased and biased ring undergoes a transition from single-step to double-step. However, for EB samples, this transition happens at larger thickness, which is attributed to the uniaxial anisotropy induced by exchange bias in the Fe layer. The magnitude of this uniaxial anisotropy is studied by measuring the angular dependence of the exchange bias field and fitted numerically with an improved effective model.

Chapter 7

NANORING MAGNETIC TUNNEL JUNCTION DEVICE WITH CURRENT PERPENDICULAR TO PLANE

7.1 Introductions

After a systematical study of the magnetic states and switching behavior of Fe rings with different thickness (t_{Fe}), lateral size (D_{out}) and width (D_{in}/D_{out}), and the effects of the exchange bias (EB) coupling on the Fe rings, we now integrate these together into a multilayer nanoring magnetic tunneling junction (MTJ) device as a candidate for future magnetoresistive random-access memory (MRAM). [102]

Magnetoresistive random-access memory (MRAM) has been intensely studied in the past few years [105] because of their potential advantages including nonvolatility, antiradiation, unlimited endurance, high speed, high density, low power consumption etc. However, the high-density and low-power-consumption have not been realized based on either the conventional magnetic field magnetization switching or the elliptic/ rectangular - shaped MTJ structures in the state of the present MRAM devices. [105] The road map of the MRAM demo device development is shown in Figure 7.1. [105]

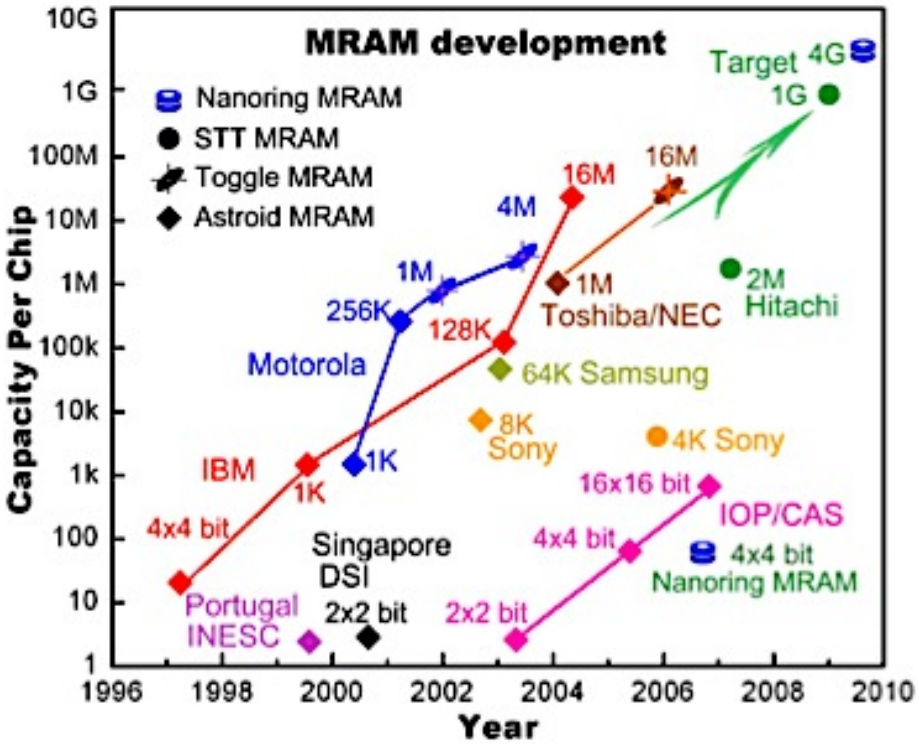

Figure 7.1 Roadmap of MRAM demo device development. [105]

The main cause of the limitation in storage density and power consumption is that the stray field energy and the shape anisotropy energy of a nanoscale size MTJ increase distinctly with increasing density, resulting in the very large coercivity and switching field and further higher power consumption compared with that of a microscale size MTJ.[106] In addition, the strong stray field interactions between the ferromagnetic layers of a MTJ or between the nearest neighboring MTJ cells can result in large magneto-conjunction effect and magnetic noise, which can whittle the independence and consistency for each MTJ as a memory cell. [105]

The ring-MTJ provide the possibility to eliminate the stray field and enhance the thermal stability since the magnetization may ideally form a vortex structure free of magnetic poles and thus could be patterned very close to each other in high density. Thus, the ring-MTJ based MRAM devices are as fast as the Dynamic Random Access Memory (DRAM), while they are non-volatile and energy efficient. While compared with other non-volatile memories like Flash, they have much better reliability. [103]

First proposed by Zhu [103], nanoring-MTJ device is first achieved experimentally by X. F. Han's group in 2007. [104] Since then, several distinct nanoring-MTJ structures have been discussed by X. F. Han,[105, 106, 107, 108] J. C. Wu [109, 110, 111] and J. M. D. Coey's groups. [112] The current-perpendicular-to-plane (CPP) type MTJ devices are fabricated via a combination of lithography and ion-milling techniques. Al-oxide and Al-N are sputtered as the barrier layer. As the magnetization of the free layer and reference layer align parallel and antiparallel with each other, a TMR ratio between 20% ~ 50% is observed. [105] Current (J~10^6 A/cm^2) assisted switching of the magnetization in free layer is also achieved but is largely attributed to the Oersted field of the current in the perpendicular-to-plane direction rather than spin-torque-transfer (STT) effect (in which the magnetization orientation of the free layer is switched by the spin-polarized current after passing through the reference layer). [106]

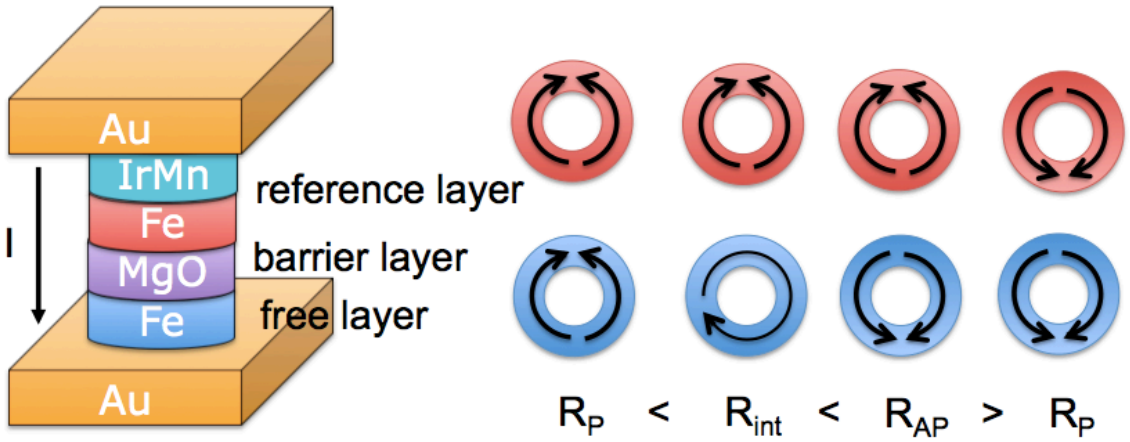

Figure 7.2 Nanoring-MTJ with a CPP configuration. The magnetic states of the free layer and reference layer will generate different resistance of the device.

A magnetic nanoring based MTJ device with a CPP configuration is shown in Figure 7.2. Sandwiched between the top and bottom Au electrodes, the ring-MTJ has a structure of Fe/MgO/Fe/IrMn, with the top reference layer consisting of IrMn/Fe exchange-bias pinned and free layer Fe at the bottom. An MgO barrier layer is deposited between them. Starting from the positive saturation field, as the magnetization of the free-layer and reference-layer align parallel, the resistance of the device should be low (R_P). Reducing the field to zero, the free layer switches to the vortex state, as the magnetization of one half ring is reversed, the resistance now will increase to R_{int}. Switching the field to the negative direction leads to the total switching of the free layer. The magnetization of the free layer and reference layer now are totally opposite to each other, giving a maximum resistance of R_{AP}. Finally, the magnetization of the reference layer reversed and the resistance will drop back to R_P. Thus, by tuning the magnetization direction in the free layer of the ring-MTJ, three distinct magnetic states with different device resistance can be achieved, which can be used to record data in such a device.

7.2 Device fabrication

It is technically challenging to fabricate the nanoring-MTJ in the CPP configuration, as shown in Figure 7.3. Multiple steps of E-beam lithography (EBL) and ion milling are needed. First a Au electrode is lithographically patterned at the bottom [Figure 7.3(2)]. Then, a multilayer ring-MTJ with D_{out}=*500 nm* is aligned and patterned by EBL right on top of the bottom electrode [Figure 7.3(3)]. To insulate the bottom and top electrode, a SiO_2 spacer square is aligned and patterned right on top of the ring-MTJ, burying the device beneath it [Figure 7.3(4)]. Then, focused ion beam (FIB) is focused on top of the ring-MTJ and a hole is ion-milled through the SiO_2 spacer layer until it reaches the top of the ring-MTJ device and stop right at that point [Figure 7.3(5)]. Finally, a top electrode is aligned and patterned on top of the device perpendicular to the bottom electrode, and the device fabrication is completed [Figure 7.3(6)].

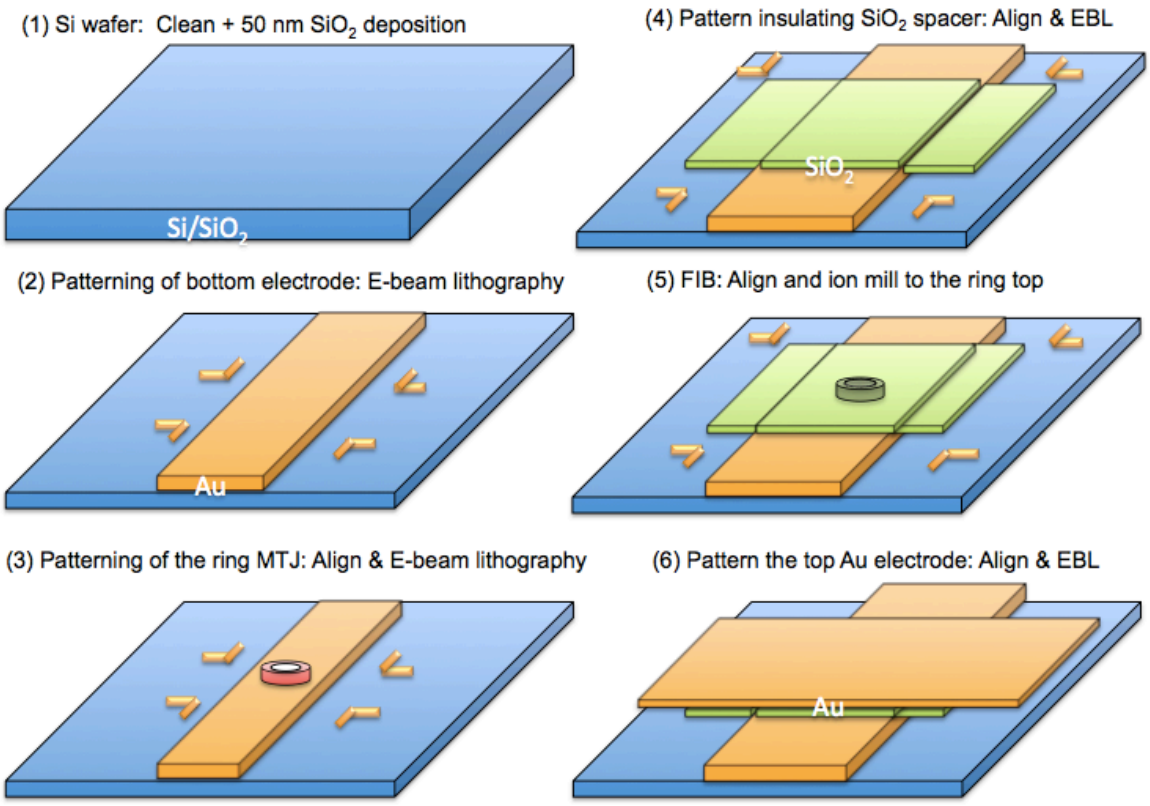

Figure 7.3 Fabrication procedure of the CPP ring-MTJ device.

Below we discuss the fabrication procedure in more detail. Si wafer is first pre-treated with standard RCA cleaning and deposited with 50 nm of SiO_2 to ensure an insulating surface. Then, 20 nm thick Au bottom electrode together with alignment marks are patterned by EBL, deposition and lift-off process, as shown in Figure 7.4. The EBL is implanted using a FEI XL-30 scanning electron microscope (SEM) operated at 30keV beam energy on a 100 nm thick poly-methyl methacrylate (PMMA) resist. The bottom electrode consists of three parts: (1) two bonding pads (2) two extension lines (3) the central electrode bar.

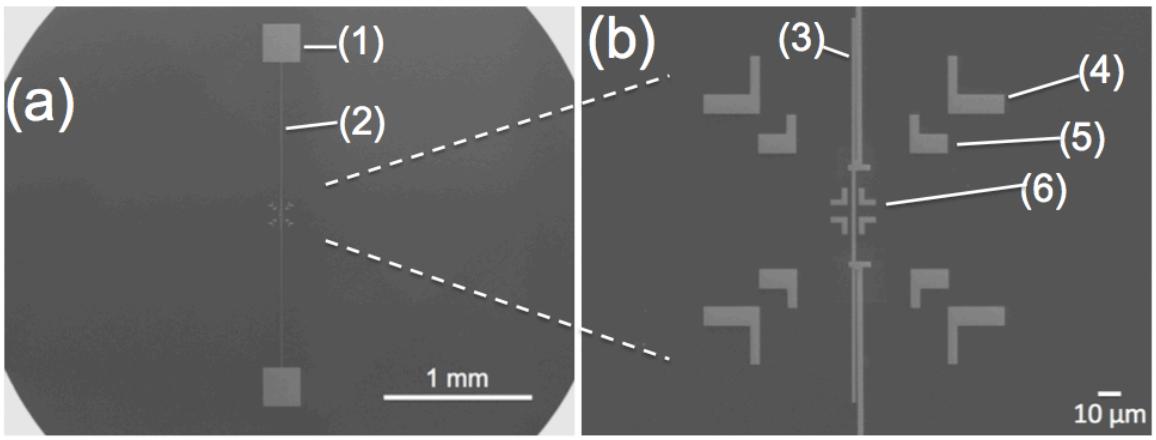

Figure 7.4 Scanning electron microscopy images of the bottom electrode and alignment marks. The bottom electrode consists of (1) bonding pad (2) extension line and (3) central electrode bar. The alignment marks consist of (4) the coarse alignment marks (5) the fine alignment marks and (6) the FIB alignment marks.

The two bonding pads are 250 nm squares separated by 2 mm. They are written by EBL at a magnification of 20, with point-to-point distance of 168 nm, spot size 5 and exposure dosage of 500 μC/cm^2. The two extension lines are 3 μm wide and 1 mm long, connecting the bonding pads and the central electrode bar. At the inner end of the extension lines, where they connect the central electrode bar, there are horizontal bars 3 μm in width and 10 μm in length to ensure their connection in case of misalignment in lithography. The extension lines are patterned at a magnification of 25, with point-to-point distance of 135 nm, spot size 1 and exposure dosage of 250 μC/cm^2. The electrode bar at the center is 2 μm in width and 200 μm in length. It is written at a magnification of 1050, with point-to-point distance of 10 nm, spot size 1 and exposure dosage of 250 μC/cm^2.

There are three sets of L-shape alignment marks surrounding the center of the electrode bar, as shown in Figure 7.4(b): (4) a set of coarse alignment marks that are off the center point by (50 μm, 50 μm) (5) a set of fine alignment marks that are off the center point by

(30 μm, 30 μm) and (6) a FIB alignment mark that is off the center point by (6 μm, 6 μm). The coarse alignment marks and the fine alignment marks are for the alignment of EBL patterns, while the FIB aliment marks serve as guides for the focused ion beam (FIB) before ion milling. The coarse alignment marks are written by EBL at a magnification of 1300, with point-to-point distance of 10 nm, spot size 3 and exposure dosage of 250 $\mu C/cm^2$. The fine alignment marks are patterned at a magnification of 2100, with point-to-point distance of 10 nm, spot size 1 and exposure dosage of 250 $\mu C/cm^2$. The FIB alignment marks are written at a magnification of 9000, with point-to-point distance of 10 nm, spot size 1 and exposure dosage of 250 $\mu C/cm^2$. The detailed EBL information is summarized in the table below.

Table 7.1 EBL details for the ring-MTJ device

	magnification	spot size	point-to-point distance (nm)	line-to-line distance (nm)	dosage ($\mu C/cm^2$)
bonding pads	20	5	168	168	500
extension line	25	1	135	135	250
central electrode bar	1050	1	10	10	250
coarse alignment marks	1300	3	10	10	250
fine alignment marks	2100	1	10	10	250
FIB alignment marks	9000	1	10	10	250
ring-MTJ	9000	1	10	10	300
SiO_2 square	9000	1	10	10	300

After exposure to the electron beam, the pattern is immersed into the 1 Methyl-isobutyl-ketone (MIBK): 3 Isopropyl alcohol (IPA) developer for 70 s, rinsed in IPA solution and blown dry with nitrogen gas. Cr(2 nm)/Au(20 nm) are then sputtered onto the patterned PMMA resist in the ion-beam sputtering chamber. Then the sample is immerged in acetone solution for 24 hours before a 15 s ultrasonic assisted lift-off. The Cr layer enhances the attachment of the Au on the SiO_2 surface.

After the bottom electrode, the ring-MTJ device is written onto the central electrode bar by alignment of the EBL. First, a rehearsal of the alignment writing is performed. The sample with just the bottom electrode is imaged by SEM following the exact same procedure as EBL: the beam is first optimized on the gold standard at a height of 6.5 mm and magnification of 100’000. Then, it is focused on the 4 corners of the sample and a planar fitting by the NPGS software is carried out, as shown in Figure 7.5. Then, sample stage is moved to search for the bottom electrode pads. After the bottom electrode is found on the screen, the *x*-axis and *y*-axis of the screen in aligned with the sides of the square bonding pads by rotating the sample stage. This step is to align the angle of sample for future aligned-writing steps. After alignment of angle, the coordinates of corner No. 4 (point 4 in Figure 7.5), the upper-left corner bonding pad (point 5 in Figure 7.5), and the center of the device (point 6 in Figure 7.5) are recorded, the movement vector from point 4 to point 5, and point 5 to point 6 is calculated and recorded for future aligned writing step.

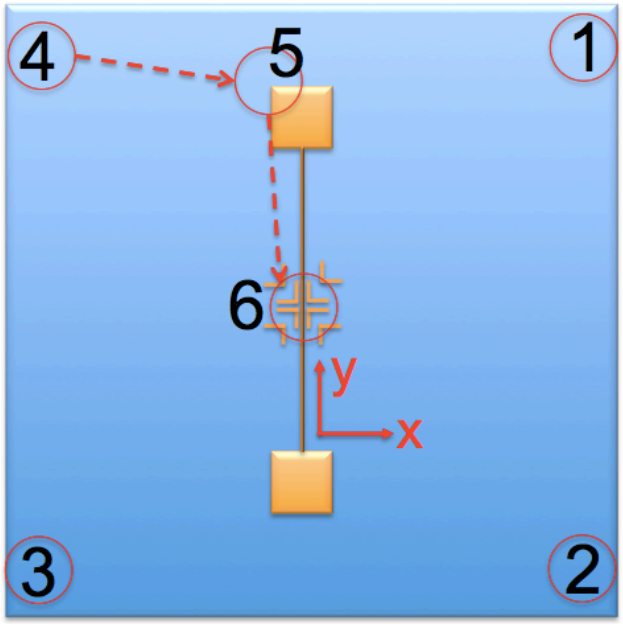

Figure 7.5 Schematic diagram of the rehearsal of the EBL alignment: After the 4-corner planar fitting, the *x*-axis and *y*-axis of the sample is aligned by rotating sample stage. Then, coordinates of the 4th corner (point 4), upper left corner of the bonding pad (point 5) and the device center (point 6) is recorded and the movement vector between them calculated and recorded.

After all the coordinates are recorded, the sample is taken out and again spin-coated with PMMA resist for the EBL of the ring-MTJ device. Like in the rehearsal step, the beam optimization and 4-corner fitting on the sample corners are carried out. Then, beam is set to spot 1 and magnification ×80. The upper-left corner of the bonding pad is searched manually on the sample surface and the *x* and *y*-axis alignments are performed. After the angle is aligned, the beam is focused on the upper-left corner (point 5 in Figure 7.5) of the bonding pads. The beam blanker is turned off to block the beam and a sample stage movement is carried out from the upper corner of the bonding pad (point 5 in Figure 7.5) to the center of the electrode bar (point 6 in Figure 7.5) by inputting the movement vector calculated in the rehearsal step. Now although the sample should be

moved to the center after the stage movement, the movement of the sample stage itself has an error of 10 μm. Thus, to align the feature accurately, windows [dashed blue windows plotted in Figure 7.3(a)] are opened on top of the alignment marks region, as shown in Figure 7.6(a). The alignment process consists of 2 steps: a coarse alignment on alignment marks that are 50 μm off the center and a fine alignment on the alignment marks 30 μm off the center. The coarse alignment is performed by opening 4 windows (blue) on top of the coarse alignment marks. By comparing the position of the real L-shape alignment marks (which is Au thus shines beneath the PMMA resist under the electron beam) with their virtually generated images on the NPGS software, the NPGS program generates an algorism to mapping the real positions of the pattern to their virtual positions. Because of the error in the sample stage movement, the coarse alignment usually shows large offsets between real and virtual positions.

Then, a fine alignment is carried out by opening another four windows [dashed red windows in Figure 7.6(a)] on the 30 μm alignment marks. The NPGS program uses the mapping result from the coarse alignment step and generates new virtual images of the alignment marks on the screen, By manually aligning the real position of the 30 μm alignment marks with their virtual images, the mapping algorism is improved. Therefore after the fine alignment, the writing of the D_{out}=*500 nm* ring is performed at the center of the electrode bar at a magnification of ×9000, with point-to-point distance of 10 nm, spot size 1 and exposure dosage of 0.6. D_{out}=*500 nm* ring is chosen because the FIB alignment marks are 3 μm off-set from the device center (limited by the magnification setting of the FIB) and the central Au electrode bar is thus only 2μm in width. In order to leave enough space for alignment error during the e-beam lithography, D_{out}=*500 nm* ring is a safe

choice. The height of the ring-MTJ device is also limited by the e-beam lithography. During the dosage test, devices with a thickness larger than 30 nm are difficult to lift-off. Therefore, the reference layer of the ring-MTJ is designed to be 10 nm thick to limit the thickness of the whole device. For the free layer, a thickness of 3 nm is chosen to make the maximum difference in switching field compared to the reference layer. After development, magnetic multilayers of Fe(3 nm) /MgO(1.5 nm)/Fe(10 nm)/IrMn(10 nm)/Au (3nm) are sputtered onto the resist layer in the ion-beam sputtering chamber.

Then the sample is immerged in acetone solution for 24 hours before a 15 s ultrasonic assisted lift-off. To introduce exchange bias interfacial coupling in the reference layer, the sample is heated to 600 K in vacuum and then cooled to room temperature under an external field of 200 Oe applied in the surface plane of the sample pointing along the bottom electrode. The SEM image of the ring-MTJ device is shown in Figure 7.6(b), pointed by a yellow arrow. The direction of the exchange bias interfacial coupling is indicated by the red arrow. The slight shift of the ring MTJ to the right side of electrode bar center is because of the magnification increase from the fine alignment (×500) to the D_{out}=*500 nm* ring writing (×3600).

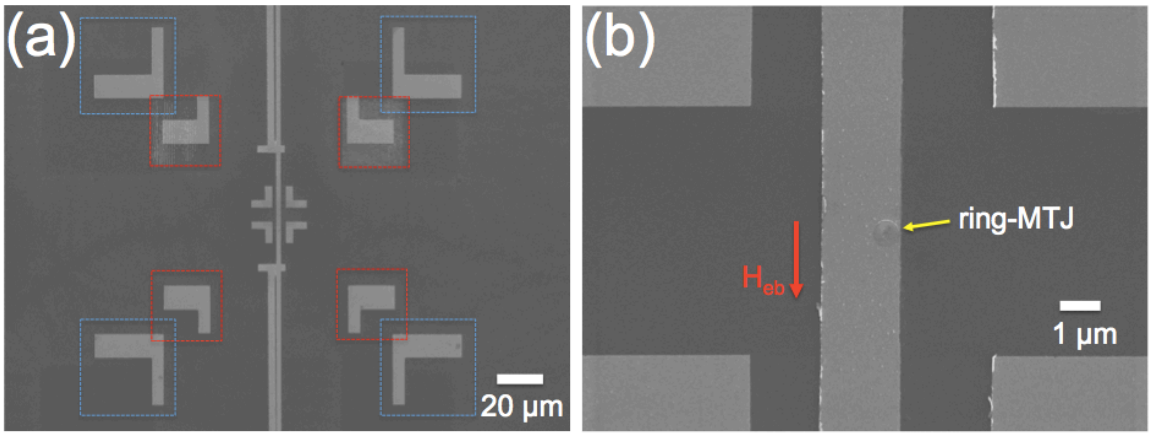

Figure 7.6 Windows are opened on top of the alignment marks (blue for coarse alignment marks and red for fine alignment marks) during the aligned EBL process. The ring-MTJ is shown in (b).

Here in the reference layer of the ring-MTJ device [Fe (10 nm)/IrMn(10 nm)], we put the antiferromagnetic IrMn (10 nm) layer on top of the ferromagnetic layer, which is different in structure from the exchange biased IrMn (10 nm)/Fe (10 nm) rings we discussed in Chapter 6. This is because (1) the ion-milling rate of the latter FIB step is unknown and putting IrMn above Fe layer helps to protect the Fe layer during the milling step; (2) growing IrMn on top of the Fe layer without the Cu (5 nm) seeding layer also helps to reduce the total thickness of the device for following lift-off step. Nevertheless, as many reports point out, [113, 114] the exchange bias induced hysteresis loop shift in the AF/FM structure is slightly larger than their FM/AF counterpart after thermo annealing. However, it is not a major concern for us here.

After patterning the ring-MTJ device on the electrode bar, a 4 μm × 4 μm square is aligned and written by EBL at the center of the device, right on top of the ring-MTJ, following the same procedure of patterning the ring-MTJ. Then, 70 nm of SiO_2 spacer layer is deposited onto the patterned resist layer and lifted-off. The SEM image of the SiO_2 spacer is shown in Figure 7.7(a). The ring-MTJ device can be seen very clearly

beneath the SiO_2 spacer. Figure 7.7(b) shows the AFM image of the SiO_2, the height profile along the red line in the AFM image shows that the SiO_2 spacer has a thickness of 70 nm.

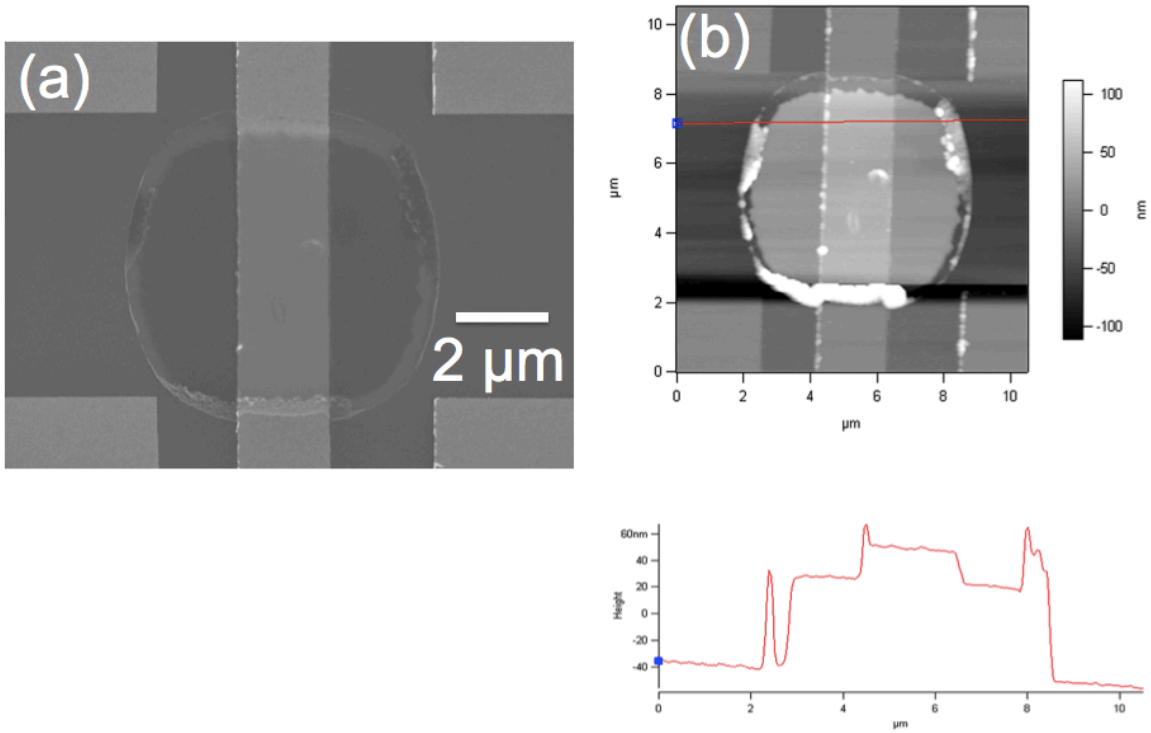

Figure 7.7 (a) SEM image of the patterned 4 µm × 4 µm SiO_2 spacer square. (b) AFM image of the SiO_2 spacer square. The height profile along the red line in the image shows the SiO_2 has a thickness of 70 nm.

After patterning the SiO_2 spacer, focused ion beam (FIB) is used to mill a hole on top of the ring-MTJ device through the SiO_2 spacer layer until the top Au capping layer of the ring-MTJ is reached. For our device, the ion milling is carried out on a FEI XL830 dual beam SEM/FIB at the NTUF. Ga^+ ion beam with beam energy of 30 kV and an emission current of 2.2 µA is used for the milling. The rings-MTJ is merely visible under the SiO_2 spacer so the ion beam is directly focused on the MTJ device and start milling. However, since the milling rate of the SiO_2 film under the FIB is unknown, the depth of the milled

hole can only be estimated. For our sample, milling time of 1s, 2s, 3s and 4s are tested on four devices. Figure 7.8 shows the FIB milled hole on top of the ring-MTJ.

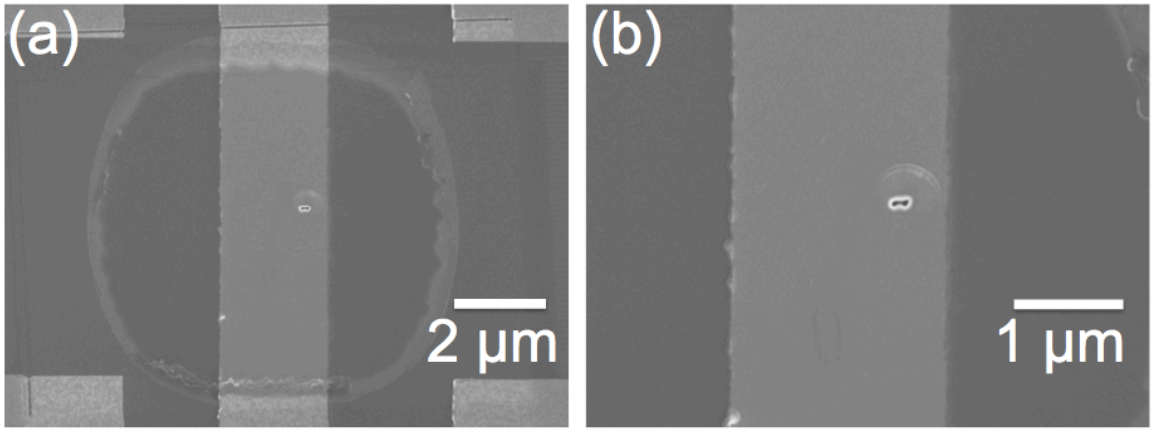

Figure 7.8 SEM images of the FIB milled hole on top of the ring-MTJ through the SiO_2 spacer layer.

The last step of the device fabrication is patterning a top electrode perpendicular to the bottom electrode along the horizontal position on top of the ring-MTJ. The top electrode has the exact same structure as the bottom electrode but along the horizontal direction: two bonding pads, two 1 mm long, 3 μm wide extension lines and a 2 μm wide, 200 μm long central electrode bar, as shown in Figure 7.9. The EBL recipe is the same as the bottom electrode and the alignment procedure is the same as the ring-MTJ and SiO_2 spacer. After development, Au (20 nm) is deposited onto the PMMA resist layer and lifted-off in acetone solution after 24 hours. The result SEM images of the complete ring-MTJ device with CPP configuration are shown in Figure 7.9(a)-7.9(c). Figure 7.9(c) clearly shows that the ring-MTJ device is within the area where the top electrode and bottom electrode intersect.

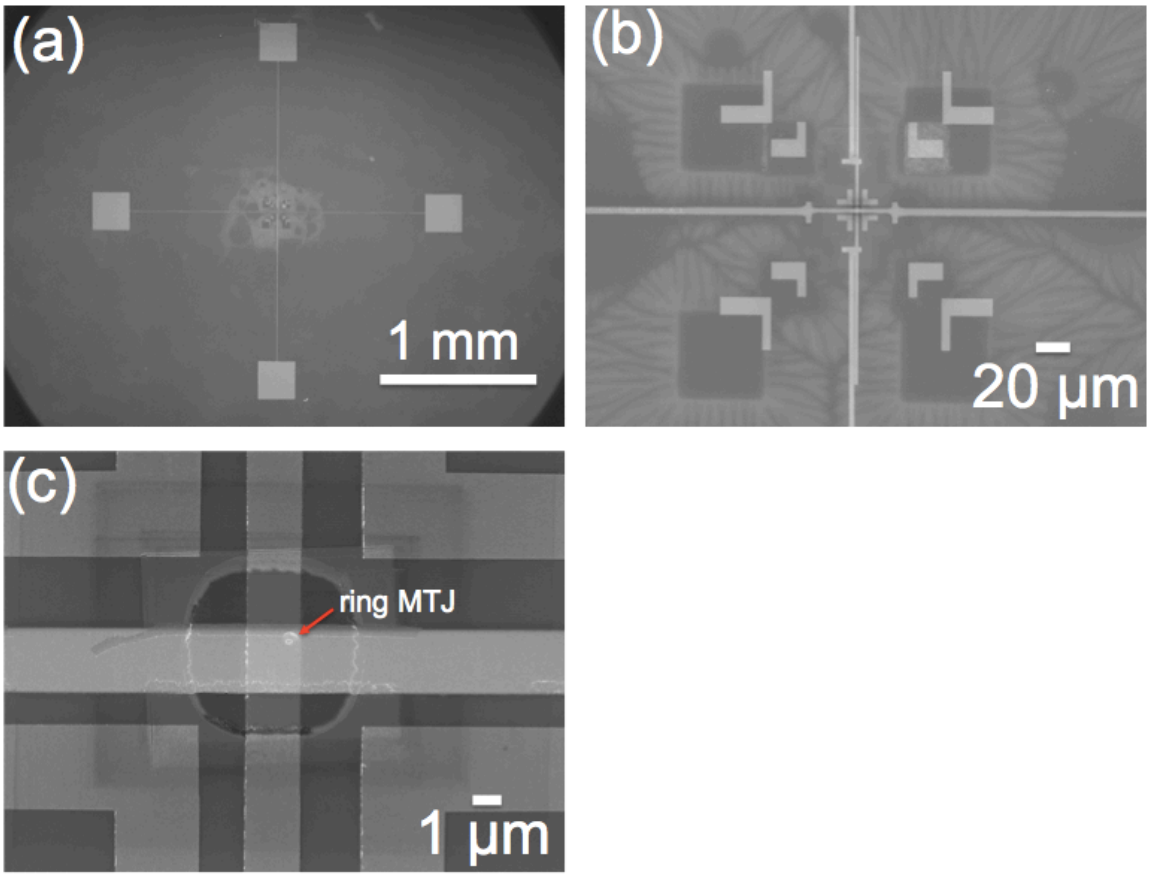

Figure 7.9 SEM images of the complete ring-MTJ device.

Finally, Si substrate with multiple ring-MTJs is manually cut into 5 mm × 5 mm squares, with only one device on each square for the subsequent transport measurement on PPMS.

7.3 Transport measurements of the CPP ring-MTJ

Each nanorings-MTJ device is measured using a four-probe method [115] via leads connected to the top and bottom electrodes. Figure 7.10(a) shows the schematic diagram of the connection and Figure 7.10(b) shows the photo of the connection on a PPMS

electro-transport sample stage. The electro-transport sample stage can rotate in plane so that the external magnetic field can be applied along different directions in the sample plane. For our ring-MTJ, the external magnetic field is applied along the exchange-bias direction, as shown in Figure 7.10 (a).

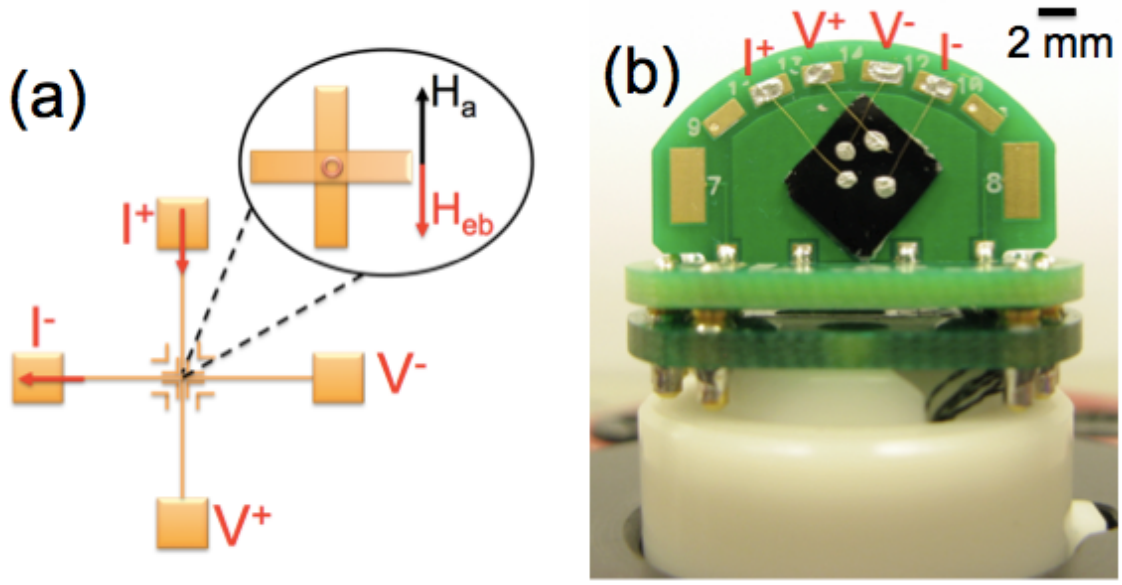

Figure 7.10 (a) Schematic diagram of the four-probe method measurement of the *R-H* loop of the ring-MTJ. The external field is applied along the EB direction. (b) Photo of the ring-MTJ connection on the QD electro-transport rotatable sample stage.

The junction resistance is measured both at 10 K and room temperature, with a constant dc current I=10 μA. The external magnetic field H_a is between -1000 Oe and +1000 Oe, with a step size of 5 Oe. So far, the measured *R-H* loops from the nanorings-MTJs do not show any significant change in resistance of the device due to the TMR effect. Figure 7.11 shows a typical measured *R-H* loop.

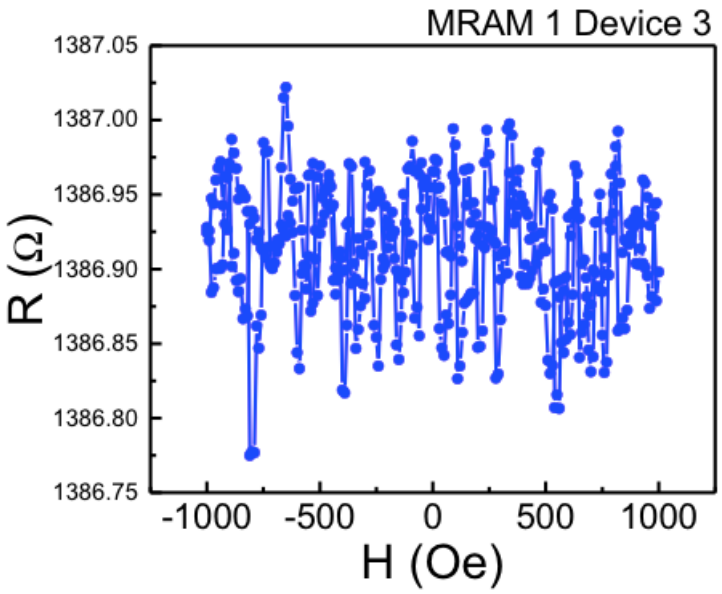

Figure 7.11 Measured resistance (R) vs. magnetic field (H) loops for ring-MTJ with CPP configuration. The temperature is 10 K.

As shown in Figure 7.11, the measured R-H loop is quite noisy with $\frac{R_{max}-R_{min}}{R_{mean}} = 0.02\%$. No obvious change in junction resistance is observed during the measurement. One of the possible reasons is that we do not have a very precise control of the FIB drill depth. The correct milling depth needs a very precise control of the milling time so that it just mills through the whole SiO_2 spacer without damaging the device.

7.4 Conclusion

We fabricated a nanoring-MTJ device with CPP configuration though multiple steps of aligned EBL and FIB milling. However, the TMR induced resistance change is not observed in the resistance measurements. One possible reason is that the milling depth of

the FIB is not correct because we do not know the milling rate of the FIB on SiO_2 film. Alternatively, our transport measurement set up did not have the necessary sensitivity to detect the changes in TMR. In the future, it is suggested that a commercial device with well-known TMR characteristics be measured to ensure that the transport measurements were done correctly before trying to troubleshoot the ring-device that was fabricated.

Chapter 8

CONCLUSIONS AND FUTURE WORK

The distinct magnetic states and highly reproducible switching behavior of the magnetic thin film ring structures not only make them interesting topic in fundamental research but also candidates for multiple magnetoelectronic and sensing devices. A systematic study on the magnetic states and reversal behaviors of the thin film Fe ring structure can therefore help our understanding of nanomagnetism and also provide reference for the design of future nanoring devices.

In this thesis, we have

(1) Studied the effect of thickness t_{Fe} on the magnetic properties of the Fe ring structures. Fe ring structures with different thickness are patterned by photolithography and a mask-transfer process. The magnetic hysteresis behaviors of the Fe rings are characterized by magneto-optical Kerr effect. The magnetic domain configurations are investigated by magnetic force microscopy and micromagnetic simulation. With the increase of the thickness, the magnetic switching of the Fe rings involves from single-step switching with quasi-saturated remanence state to double-step switching with vortex state at remanence. This is explained by the increasing energy density different between the vortex state and single domain state as t_{Fe} increases.

(2) Studied the effect of size D_{out} on the magnetic properties of the Fe ring structures. Fe ring structures with different sizes are patterned by electron-beam lithography and lift-off.

With the decrease of the size, the magnetic switching of the Fe rings involves from double-step switching with vortex state at remanence to single-step switching with quasi-saturated remanence state.

(3) Studied the effect of width D_{in}/D_{out} on the magnetic properties of the Fe ring structures. With the D_{in}/D_{out} ratio of the ring decreasing, the magnetic hysteresis behavior of the ring evolves from double-step with vortex state in-between to single-step. This is explained by the increasing energy difference between vortex state and single domain state as D_{in}/D_{out} ratio increases.

(4) Established a energy density model by using the micromagnetic simulator to calculate the energy density evolution of the vortex state, single-domain state and axial state with the Fe ring size (D_{out}), thickness (t_{Fe}) and width (D_{in}/D_{out}).

(5) Studied the effects of exchange bias (EB) on the magnetization reversal behaviors in lithographic IrMn/Fe rings and their unbiased Fe counterparts, with the thickness of the Fe layer, t_{Fe}, varying from 10 nm to 80 nm. In thin IrMn/Fe (10 nm) EB rings, EB induces anisotropic reversal modes in the ring structure. When external field is applied along the bias direction, magnetic reversal of the ring is dominated by domain nucleation and growth. When external field is applied perpendicular to the bias direction, magnetic reversal is dominated by coherent rotation. As t_{Fe} increases, the hysteresis loops of both unbiased and biased ring undergoes a transition from single-step to double-step. However, for EB samples, this transition happens at larger thickness, which is attributed to the uniaxial anisotropy induced by exchange bias in the Fe layer. The magnitude of this

uniaxial anisotropy is studied by measuring the angular dependence of the exchange bias field and fitted numerically with an improved effective model.

(6) Fabricated a nanoring-MTJ device with CPP configuration though multiple steps of aligned EBL and FIB milling. However, the TMR induced resistance change is not observed in the resistance measurements. One possible reason is that the milling depth of the FIB is not correct because we do not know the milling rate of the FIB on SiO_2 film.

Therefore, in the future, it is desirable if we can replace the FIB step in our device fabrication with a more controllable process. One solution, as shown in Figure 8.1, is to use Poly-methyl methacrylate (PMMA) to replace SiO_2 as the insulating spacer layer between the top and bottom electrodes.

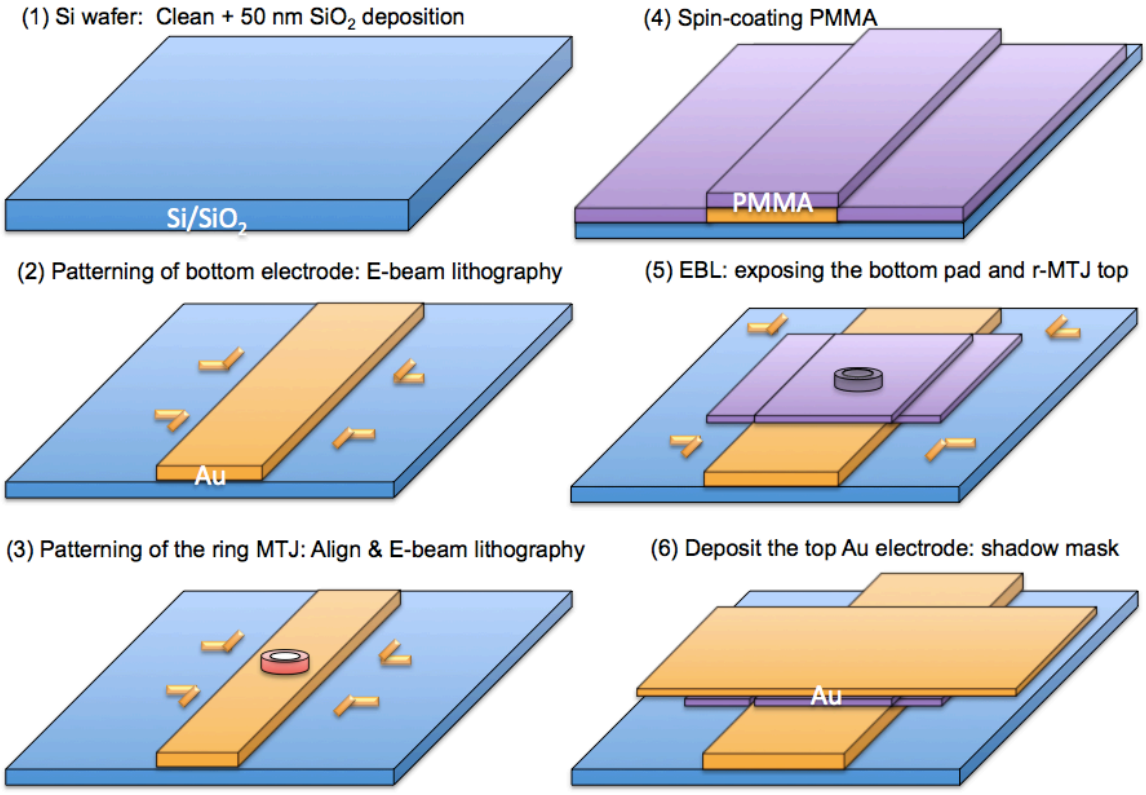

Figure 8.1 Revised fabrication procedure of the CPP ring-MTJ device with PMMA as the insulating spacer layer.

After the ring-MTJ is deposited and lifted-off, PMMA is spin-coated onto the substrate [Figure 8.1(4)]. Then, e-beam lithography is used to expose the bottom bonding pads and also the top of the ring-MTJ device [Figure 8.1(5)]. The e-beam exposure dosage on top of the ring-MTJ needs to be carefully tuned so that the PMMA within the center hole of the ring-MTJ is still intact to maintain the insulation between the top and bottom electrodes. Since the PMMA layer is used as the insulating spacer, the top electrode can only be deposited via shadow mask deposition [Figure 8.1(6)].

BIBLIOGRAPHY

[1] B. D. Terris and T. Thomson, *J. Phys. D: Appl. Phys.* **38**, R199 (2005).

[2] W. Zhang and K. M. Krishnan, *J. Appl. Phys.* 111, 07B509 (2012).

[3] M. Salaun, M. Zelsmann, S. Archambault, D. Borah, N. Kehagias, C. Simao, O. Lorret, M. T. Shaw, C. M. S. Torres and M. A. Morris, *J. Mater. Chem. C* **1**, 3544 (2013).

[4] J. Zaanen, *Science* **323**, 888 (2009).

[5] H. Lee, A. M. Purdon, V. Chu, and R. M. Westervelt, *Nano Lett*. **4**, 995 (2004).

[6] A. O. Adeyeye and N. Singh, *J. Phys. D* **41**, 153001 (2008).

[7] W. Zhang, D. N. Weiss, and K. M. Krishnan, *J. Appl. Phys.* **107**, 09D724 (2010).

[8] F. Cheynis, A. Masseboeuf, O. Fruchart, N. Rougemaille, J. C. Toussaint, R. Belkhou, P. B. Guillemaud, and A. Marty, *Phys. Rev. Lett.* **102**, 107201 (2009).

[9] T. Shinjo, T. Okuno, R. Hassdorf, K. Shigeto, T. Ono, *Science* **289**, 930 (2000).

[10] T. Koyama, D. Chiba, K. Ueda, K. Kondou, H. Tanigawa, S. Fukami, T. Suzuki, N. Ohshima, N. Ishiwata, Y. Nakatani, K. Kobayashi, and T. Ono, *Nature Mater.* **10**, 194 (2011).

[11] H. X. Wei, F. Q. Zhu, X. F. Han, Z. C. Wen, and C. L. Chien, *Phys. Rev. B* **77**, 224432 (2008).

[12] T. Shinjo, T. Okuno, R. Hassdorf, K. Shigeto, T. Ono, *Science* **289**, 930 (2000).

[13] J. Miltat and A. Thiaville, *Science* **298**, 555 (2002).

[14] A. Wachowiak, J. Wiebe, M. Bode, O. Pietzsch, M. Morgenstern, R. Wiesendanger, *Science* **298**, 577 (2002).

[15] S. B. Choe, Y. Acremann, A. Scholl, A. Bauer, A. Doran, J. Stohr, H. A. Padmore, *Science* **304**, 420 (2004).

[16] J. A. J. Burgess, A. E. Fraser, F. Fani Sani, D. Vick, B. D. Hauer, J. P. Davis, M. R. Freeman, *Science* **339**, 1051 (2013).

[17] H. Jung, Y. S. Choi, K. S. Lee, D. S. Han, Y. S. Yu, M. Y. Im, P. Fischer, and S. K. Kim, *ACS Nano* **6**, 3712 (2012).

[18] I. V. Roshchin, C. P. Li, H. Suhl, X. Battle, S. Roy, S. K. Sinha, S. Park, R. Pynn, M. R. Fitzsimmons, J. M. Lopez, D. Altbir, A. H. Romero and I. K. Schuller, *Europhys. Lett.* **86**, 67008 (2009).

[19] N. Martin, N. C. Bigall, I. Mönch, T. Gemming, A. Eychmüller, R. Mattheis, R. Schäfer, L. Schultz, and J. McCord, *Adv. Funct. Mater.* **21**, 891 (2011).

[20] S. Y. H. Lua, S. S. Kushvaha, Y. H. Wu, K. L. Teo, and T. C. Chong, *Appl. Phys. Lett.* **93**, 122504 (2008).

[21] D. H. Kim, E. A. Rozhkova, I. V. Ulasov, S. D. Bader, T. Rajh, M. S. Lesniak and V. Novosad, *Nature Mater.* **9**, 165 (2010).

[22] R. P. Cowburn, D. K. Koltsov, A. O. Adeyeye, and M. E. Welland, *Phys. Rev. Lett.* **83**, 1042, (1999).

[23] R. P. Cowburn, D. K. Koltsov, A. O. Adeyeye, and M. E. Welland, *Phys. Rev. Lett.* **83**, 1042 (1999).

[24] J. Akerman, *Science* **308**, 508 (2005).

[25] J. G. Zhu, Y. F. Zheng, and G. A. Prinz, *J. Appl. Phys.* **87**, 6668 (2000).

[26] F. J. Castano, C. A. Ross and A. Eilez, *J. Phys. D: Appl. Phys.* **36**, 2031 (2003).

[27] C. B. Muratov and V. V. Osipov, *IEEE Trans. Magn.* **45**, 8 (2009).

[28] S. R. Bowden and U. J. Gibson, *IEEE Trans. Magn.* **45**, 5326 (2009).

[29] J. L. Landro, T. J. Hayward, D. Morecroft, J. A. C. Bland, F. J. Castaño, I. A. Colin, and C. A. Ross, *Appl. Phys. Lett.* **91**, 203904 (2007).

[30] P. E. Roy, J. H. Lee, T. Trypiniotis, D. Anderson, G. A. C. Jones, D. Tse, and C. H. W. Barnes, *Phys. Rev. B* **79**, 060407(R) (2009).

[31] M. Negoita, T. J. Hayward, and D. A. Allwood, *Appl. Phys. Lett.* **100**, 072405 (2012).

[32] E. Tadmor, Y. J. Rosen, Ivan K. Schuller, and S. B. Ad, *J. Appl. Phys.* **112**, 103903 (2012).

[33] C. L. Chien, F. Q. Zhu, and J. G. Zhu, *Physics Today* **60**, 40 (2007).

[34] S. D. Bader, *Rev. Mod. Phys.* **78**, 1 (2006).

[35] M. Kläui, C. A. F. Vaz, L. Lopez-Diaz and J. A. C. Bland, *J. Phys.: Condens. Matter.* **15**, R985 (2003).

[36] M. H. Park, Y. K. Hong, B. C. Choi, M. J. Donahue, H. Han, and S. H. Gee, *Phys. Rev. B* **73**, 094424 (2006).

[37] Y. F. Hou, Q. F. Zhan, K. M. Krishnan, *Appl. Phys. Lett.* **98** 042510 (2011).

[38] J. M. D. Coey, *Magnetism and Magnetic Materials*, Cambridge University Press. (2009).

[39] M. R. Fitzsimmons, S. D. Bader, J. A. Borchers, G. P. Felcher, J. K. Furdyna, A. Hoffmann, J. B. Kortright, I. K. Schuller, T. C. Schulthess, S. K. Sinhaa, M. F. Toney, D. Weller, S. Wolf, *J. Magn. Magn. Mater.* **271**, 103 (2004).

[40] M. Beleggia, J. W. Lau, M. A. Schofield, Y. Zhu, S. Tandon, M. De Graef, *J. Magn. Magn. Mater.* **301**, 131 (2006).

[41] C. A. F. Vaz, C. Athanasiou, and J. A. C. Bland, *Phys. Rev. B* **73**, 054411 (2006).

[42] P. Landeros, J. Escrig, and D. Altbir, M. Bahiana and J. d'Albuquerque Castro, *J. Appl. Phys.* **100**, 044311 (2006).

[43] C. A. F. Vaz, L. Lopez-Diaz, M. Kläui, J. A. C. Bland, T. L. Monchesky and J. Unguris, Z. Cui, *Phys. Rev. B* **67**, 140405(R) (2003)

[44] M. Ohring, *Materials Science of Thin Films*, Elsevier Press. (2006).

[45] M. T. Johnson, P. J. H. Bloemen, F. J. A. den Broede and J. J. de Vries, *Rep. Prog. Phys.* **59** 1409 (1996).

[46] R. Advincula and W. Knoll, *Functional Polymer Films*, Wiley. (2011).

[47] B. Lewis and J. C. Anderson, *Nucleation and Growth of Thin Films*, Academic Press, New York. (1978).

[48] D. L. Smith, *Thin film deposition, principles & practice*, McGraw-Hill INC, (1995).

[49] M. D. Deal, P. B. Griffin, *Silicon VLSI Technology, Fu*ndamentals, Practice and Modeling, Wiley. (2011).

[50] D. Qin, Y. Xia, J. A. Rogers, R. J. Jackman, X. M. Zhao, G. M. Whitesides, *Top. Curr. Chem.* **194**, 1 (1998).

[51] G. S. Rohrer, *Structure and bonding in crystalline materials*, Cambridge University Press. (2001).

[52] B. E. Warren, *X-ray Diffraction*, Dover Publications, Inc. (1990)

[53] H. Feng, *X-ray Reflectivity Studies of Thin Film,* Center for Materials for information Technology, University of Alabama, Tuscaloosa, AL (2005).

[54] S. Bader, *J. Magn. Magn. Mater.* **100**, 440 (1991).

[55] Z. Q. Qiu and S. D. Bader, *J. Magn. Magn. Mater.* **200**, 664 (1999).

[56] http://www.asylumresearch.com/ProbeStore/TIP_RADIUS?Entry=JustLooking

[14] T.L. Gilbert, *Phys. Rev.* **100**, 1243 (1955).

[57] W. F. Brown Jr, *Micromagnetics*, Interscience Publishers (1963).

[58] A. Aharoni, *Introduction to the Theory of Ferromagnetism*, Oxford University Press (2001).

[59] J. Fidler, R. W. Chantrell, T. Schrefl, and M. A. Wongsam, Elsevier Science (2001).

[60] L. D. Landau, E.M. Lifshitz, *Theory of the dispersion of magnetic permeability in ferromagnetic bodies*. *Phys. Z. Sowietunion* **8**, 153 (1935).

[61] G. Bertotti, Tutorial Session Notes: *Micromagnetics and Nonlinear Magnetization Dynamics*, 10th Biennal Conference on Electromagnetic Fields Computation, Perugia (2002).

[62] A. Arrott, Plenary Lecture: *Progress in Micromagnetics*, Moscow International Symposium on Magnetism, Moscow (2002).

[63] R. Victora, *Phys. Rev. Lett*. **58**, 1788 (1987).

[64] M. R. Sheinfein, the LLG code can be found at http://IIgmicro.home.mindspring.com/

[65] M. d'Aquino, *Nonlinear Magnetization Dynamics in Thin-films and Nanoparticles*, Ph. D. thesis, (2004).

[66] T. Schrefl, J. Fidler, D. Suess, W. Scholz, V. Tsiantos, *Micromagnetic simulation of dynamic and thermal effects*, Institute of Applied and Technical Physics Vienna University of Technology, Wiedner Haupstr. **8**, 10 (1999).

[67] Y.-F. H. and K. M. Krishnan, *J. Appl. Phys.* **111**, 033910 (2012).

[68] N. Suzuki, H. Tanaka, and T. Kawai, *Adv. Mater.* **20**, 909 (2008).

[69] W. Zhang, D. N. Weiss, and K. M. Krishnan, *J. Micromech. Microeng.* **21**, 045024 (2011).

[70] T. Miyawaki, K. Toyoda, M. Kohda, and A. Fujita, and J. Nitta, *Appl. Phys. Lett.* **89**, 122508 (2006).

[71] E. Tadmor, Y. J. Rosen, I. K. Schuller, and S. Bar-Ad, *J. Appl. Phys.* 112, 103903 (2012)

[72] P. E. Roy, J. H. Lee, T. Trypiniotis, D. Anderson, G. A. C. Jones, D. Tse, and C. H. W. Barnes, *Phys. Rev. B* **79**, 060407(R) (2009).

[73] T. Miyawaki, K. Toyoda, M. Kohda, and A. Fujita, and J. Nitta, *Appl. Phys. Lett.* **89**, 122508 (2006).

[74] M. Beleggiaa, J. W. Laua, M.A. Schofielda, Y. Zhua, S. Tandonb, M. De Graefb, *J. Magn. Magn. Mater.* **301**, 131 (2006).

[75] M. Kläui, C. A. F. Vaz, L. J. Heyderman, U. Rudiger, and J. A. C. Bland, *J. Magn. Magn. Mater.* **290**, 61 (2005).

[76] R. P. Cowburn, D. K. Koltsov, A. O. Adeyeye, and M. E. Welland, *Phys. Rev. Lett.* 83, 1042 (1999).

[77] P. Landeros, J. Escrig, and D. Altbir, M. Bahiana and J. d'Albuquerque e Castro, *J. Appl. Phys.* **100,** 044311 (2006).

[78] C. A. F. Vaz, C. Athanasiou, J. A. C. Bland, and G. Rowlands, *Phys. Rev. B* **73,** 054411 (2006).

[79] H. X. Wei, J. He, Z. C. Wen, X. F. Han, W. S. Zhan, and S. Zhang, *Phys. Rev. B* **77,** 134432 (2008).

[80] E. Tadmor, Y. J. Rosen, Ivan K. Schuller, and S. Bar-Ad, *J. Appl. Phys.* **112**, 103903 (2012).

[81] F. J. Castaño, C. A. Ross, A. Eilez, W. Jung, and C. Frandsen, *Phys. Rev. B* **69**, 144421 (2004).

[82] T. Miyawaki, K. Toyoda, M. Kohda, and A. Fujita, and J. Nitta, *Appl. Phys. Lett.* **89**, 122508 (2006).

[83] F. J. Castano, C. A. Ross, C. Frandsen, A. Eilez, D. Gil, H. I. Smith, M. Redjdal and F. B. Humphrey, *Phys. Rev. B* **67**, 184425 (2003).

[84] Y. Ren and A. O. Adeyeye, *J. Appl. Phys.* **111**, 013909 (2012).

[85] G. Shimon, A. O. Adeyeye, and C. A. Ross, *J. Appl. Phys.* **105**, 063901 (2009).

[86] http://www.asylumresearch.com/Probe/ASYMFMHC,Asylum

[87] T. Miyawaki, K. Toyoda, M. Kohda, and A. Fujita, and J. Nitta, *Appl. Phys. Lett.* **89**, 122508 (2006).

[88] M. Klaui, C. A. F. Vaz, J. A. C. Bland, W. Wernsdorfer, G. Faini, and E. Cambril, *Appl. Phys. Lett.* **81**, 108 (2002).

[89] F. Q. Zhu, G. W. Chern, O. Tchernyshyov, X. C. Zhu, J. G. Zhu and C. L. Chien, *Phys. Rev. Lett.* **96**, 027205 (2006).

[90] P. Vavassori, M. Grimsditch, V. Novosad, V. Metlushko, and B. Illic, *Phys. Rev. B* **67**, 134429 (2003).

[91] A. O. Adeyeye, S. Goolaup, N. Singh, C. C. Wang, X. S. Gao, C. A. Ross, W. Jung, and F. J. Castano, *J. Phys. D: Appl. Phys.* **40**, 6479 (2007).

[92] C. A. F. Vaz, L. Lopez-Diaz, M. Klaui, J. A. C. Bland, T. L. Monchesky, J. Unguris, and Z. Cui, *Phys. Rev. B* **67**, 140405 (2003).

[93] Z. B. Guo, Y. K. Zheng, K. B. Li, Z. Y. Liu, P. Luo, and Y. H. Wu, *J. Appl. Phys.* **95**, 4918 (2004).

[94] W. Jung, F. J. Castano and C. A. Ross, *Phys. Rev. Lett.* **97**, 247209 (2006).

[95] W. Jung, F. J. Castano, D. Morecroft, C. A. Ross, R. Menon, and H. I. Smith, *J. Appl. Phys.* **97**, 10113 (2005).

[96] D. Tripathy, A. O. Adeyeye, N. Singh, and R. L. Stamps, *Nanotechnology* **20**, 015304 (2009).

[97] N. Suzuki, H. Tanaka, and T. Kawai, *Adv. Mater.* **20**, 909 (2008).

[98] H. S. Jung, H. Fujiwara, and S. Matsunuma, *J. Magn. Magn. Mater.* **286**, 229 (2005).

[99] T. Ambrose, R. L. Sommer, and C. L. Chien, *Phys. Rev. B* **56**, 83 (1997).

[100] B. Beckmann, U. Nowak, and K. D. Usadel, *Phys. Rev. Lett*. **91**, 18 (2003).

[101] W. Zhang, D. N. Weiss, and K. M. Krishnan, *J. Micromech. Microeng.* **21** 045024 (2011).

[102] X. F. Han, H. X. Wei, Z. L. Peng, H. D. Yang, J. F. Feng, G. X. Du, Z. B. Sun, L. X. Jiang, Q. H. Qin, M. Ma, Y. Wang, Z. C. Wen, D. P. Liu and W. S. Zhan, *J. Mater. Sci. Technol.* 23, 304 (2007).

[103] J. G. Zhu, Y. Zheng, and G. A. Prinz, *J. Appl. Phys.* **87** 6668 (2000).

[104] Z. C. Wen, H. X. Wei, and X. F. Han, *Appl. Phys. Lett.* **91**, 122511 (2007).

[105] X. F. Han, Z. C. Wen, and H. X. Wei, *J. Appl. Phys.* **103**, 07E933 (2008).

[106] H. X. Wei, M. C. Hickey, G. I. R. Anderson, X. F. Han and C. H. Marrows, *Phys. Rev. B* **77**, 132401 (2008).

[107] H. X. Wei, J. He, Z. C. Wen, X. F. Han, W. S. Zhan, S. Zhang, *Phys. Rev. B* **77**, 134432 (2008).

[108] H. X. Wei, F. Q. Zhu, X. F. Han, Z. C. Wen, and C. L. Chien, *Phys. Rev. B* **77**, 224432 (2008).

[109] C. C. Chen, C. C. Chang, Y. C. Chang, C. T. Chao, C. Y. Kuo, L. Horng, J. C. Wu, T. Wu, G. Chern, C. Y. Huang, M. Tsunoda, and M. Takahashi, *IEEE Trans. Mag.* **43**, 920 (2007).

[110] C. C. Chen, C. T. Chao, C. Y. Kuo, L. Horng, G. Chern, C. Y. Huang, S. Isogami, M. Tsunoda, M. Takahashi and J. C. Wu, *IEEE Trans. Mag.* **43**, 2824 (2007).

[111] C. C. Chen, J. Y. Lin, L. Horng, J. S. Yang, S. Isogami, M. Takahashi and J. C. Wu, *IEEE Trans. Mag.* **45**, 3546 (2009).

[112] J. F. Feng, Z. Diao, G. Feng, E. R. Nowak, and J. M. D. Coey, *Appl. Phys. Lett.* **96**, 052504 (2010).

[113] G. Malinowski, M. Hehn and P. Panisso, *J. Phys.: Condens. Matter.* **18**, 3385 (2006).

[114] V. K. Sankaranarayanan, S. M. Yoon, D. Y. Kim, C. O. Kim, and C. G. Kim, *J. Appl. Phys.* **96**, 7428 (2004).

[115] H. X. Wei, Q. H. Qin, M. Ma, R. Sharif, and X. F. Han, *J. Appl. Phys.* **101**, 09B501 (2007).

APPENDIX A

Photolithography recipes

Procedure:

Clean the Si wafer

(1) Clean the Si wafer with piranha solution (3:1 mixture of H_2SO_4 and H_2O_2) for 10 minutes. DI water rinse 3 times.

(2) Immerse the Si wafer in $5H_2O + 1H_2O_2 + 1NH_4OH$ solution (SC-1) at 70 – 80 °C for 10 minutes. DI water rinse 3 times.

(3) Immerse the Si wafer in 1:50 solution of HF for 5 minutes. DI water rinse 3 times.

(4) Immerse the Si wafer in 1:1:6 solution of $HCl + H_2O_2 + H_2O$ (SC-2) at 75 - 80 °C for 10 minutes. DI water rinse 3 times.

(5) Spin dry the Si wafer.

Spin coat the photoresist

(6) Put the Si wafer into the hexamethyldisilazane (HMDS) vapor oven, baking for a complete cycle (45 mins).

(7) Spin coat the photoresist (AZ1512) onto the Si wafer surface at 4000 rpm for 1 min.

(8) Pre-bake the Si wafer on the hot plate at 90°C for 30 minutes.

Exposure

(9) Expose the wafer using the EVG 610 semi-automated mask alignment system, with an UV light source of 450 nm wavelength and power of 500 W for 3.3 seconds. The exposure energy dose is 23 mJ/cm^2.

(10) Post-exposure bake (PEB) the Si wafer on hot plate at 100 °C for 10 minutes.

Develop

(11) Develop the Si wafer in the 3:1 AZ312 MIF developer: H_2O solution for 60 seconds.

(12) Rinse the wafer in DI water 3 times, spin dry.

APPENDIX B

Electron-beam lithography (EBL) recipes

Procedure:

Prepare substrate

(1) Cut the Si wafer into 2 cm × 2 cm square.

(2) Clean the Si substrate with acetone. Blow-dry with N_2.

(3) Spin coat PMMA (6% solution in IPA) onto the Si substrate at 3000 rpm for 45 s.

(4) Bake the substrate on hot plate at 180 °C for 90 seconds.

(5) Scratch the 4 corners of the Si wafer using diamond scribe.

(6) Mount the substrate on the sample holder with carbon tape.

(7) Blow the substrate with N_2.

Load substrate

(8) Mount the Gold Nanoparticle Standard and the Ferriday Cup on the sample holder.

(9) Put the switch of the FEI XL-30 SEM from “A” to “C”, C for conducting.

(10) Pump down the SEM chamber.

Prepare the SEM

(11) Connect the picoammeter to the SEM port in front of the chamber door.

(12) Power on the picoammeter. Wait for 5 s and press “ZCHK” to put it in the “nA” range.

(13) Connect the NPGS bundle to the SEM control board.

(14) Switch data box to “NPGS” and monitor to “2”.

(15) Set the beam to 30 kV and spot size 3.

(16) Turn on the electron beam.

Beam optimization and current measurement

(17) Focus and stigmata on gold nanoparticles at 6.5 mm forward distance and 100,000× magnification.

(18) Use stage “tracking mode” and move to the Ferriday Cup.

(19) Center and magnify the 70 μm hole at the center of the Ferriday Cup. Go to maximum magnification at the hole.

(20) Wait for current reading on the picoammeter to stabilize.

(21) Input the values of the current (spot 1, spot 3 and spot 5) in the NPGS run file.

Point focus and planar fitting

(22) Use stage “tracking mode” to move to corner #1 of the Si substrate.

(22) Change SCAN to Slow Scan 2 and select stage “Get Mode”.

(23) Select a clean edge and center in field. Magnify and re-center clean edge to reach 2000×.

(24) Raise the stage manually with the “Z” knob on the chamber door to focus on the PMMA edge.

(25) Magnify to 8000× and fine adjust stage height manually by focus.

(26) Click Magnification > Reference, change from “Videopoint” to “Display”.

(27) In the NPGS software, select Command > Direct Stage Control, collect the position of corner #1.

(28) Zoom out and move to corner #2, switch to Slow Scan 2.

(29) Focus with mouse at 8000× magnification on a clean edge of the PMMA. Collect the position of corner #2.

(30) Repeat previous steps for corner 3 and corner 4.

(31) In the NPGS software, perform a planar fitting after the positions of corner #1-4 are collected. If the RMS value is smaller than 0.02, the planar fitting is good enough for the exposure.

Prepare the NPGS software for Run

(32) Turn on the External Beam Blanker.

(33) Change the Scan mode of the SEM from “Full Frame” to “External XY”.

(34) In the NPGS program, under “Command”, choose “Calibrate DACs” and wait for 40 seconds.

(35) Press DAC [+3.6, +5.0] button.

(36) In the NPGS software, choose your runfile and right click to check the parameter settings.

(37) For Fe ring samples with D_{out} and D_{in}/D_{out} variation, the magnification of writing is set at 3600×, using post size 1, point-to-point distance of 10.3 nm and line-to-line distance of 10.3 nm. The pattern covers an area of 60 μm× 60 μm. The exposure dosage of the PMMA layer is between 50 ~ 500 μC/cm^2, however, the dosage of a specific pattern is usually determined by a dosage test in advance.

The detailed recipe for the device fabrication is discussed in detail in Chapter 7.

Process the run file

(38) Move the sample stage to the center of the substrate and process the runfile in NPGS software.

(39) After writing, turn off the electron beam, vent the chamber and take the sample out.

Develop the pattern

(40) Immerse the substrate is into the 1:3 MIBK to IPA developer for 70 s

(41) Rinse the substrate in IPA solution and blow dry with nitrogen gas.

APPENDIX C

Energy density calculation of the vortex state, single-domain state and axial state

We use the LLG micromagnetic simulator software to calculate the energy density of the vortex state, single-domain state and axial state of Fe ring structure with D_{out} varying from 30 nm to 1000 nm, D_{in}/D_{out} from 0.1 to 0.9, t_{Fe}/D_{out} from 0.1 to 1.0. Since there are 3 independent variables (D_{out}, D_{in}/D_{out}, t_{Fe}/D_{out}) determine the energy density, we fix one variable and plot the energy density as a function of the other two variables:

(1) D_{out} fixed, E vs. D_{in}/D_{out} and t_{Fe}/D_{out}:

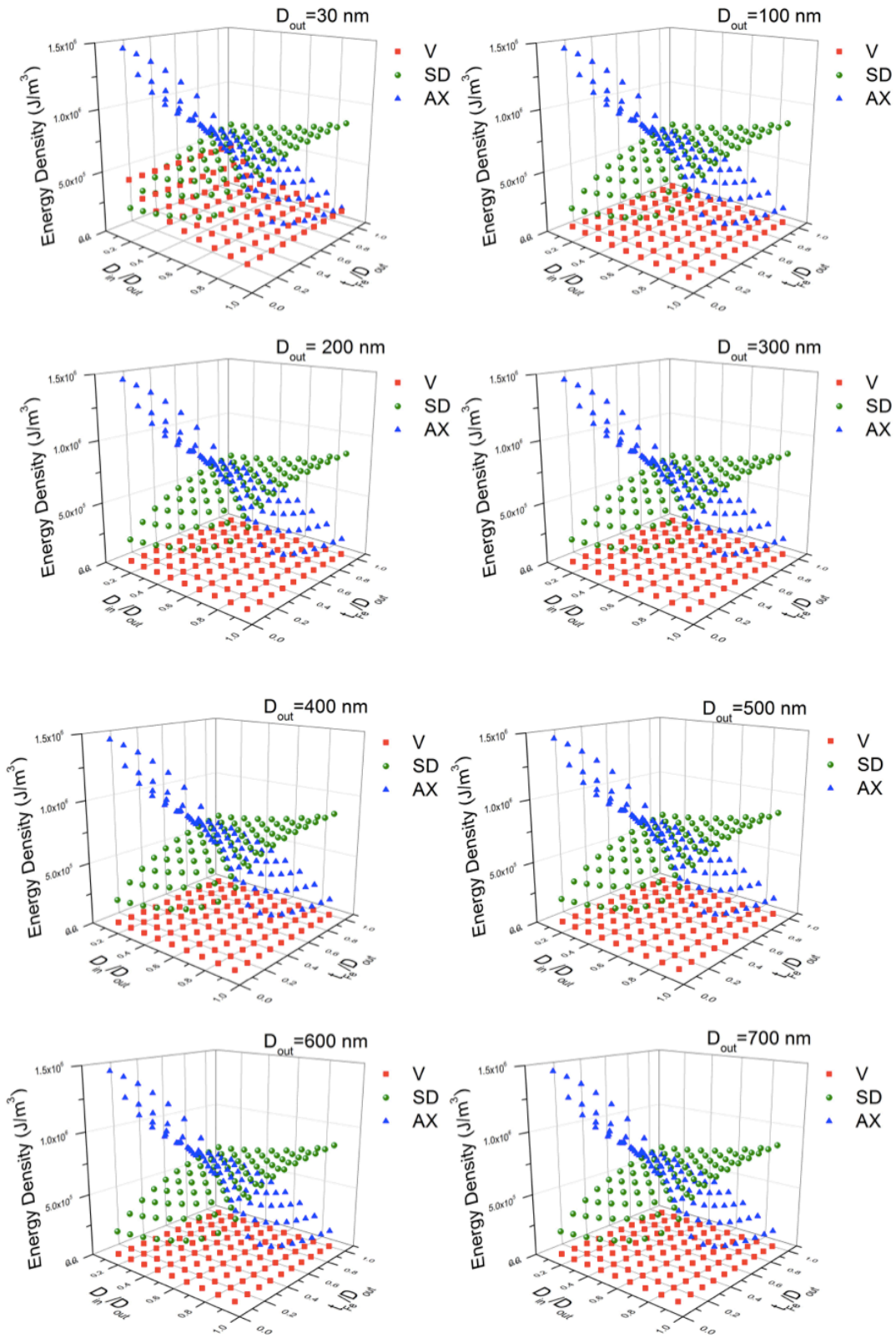
D_out=30 nm
D_out=100 nm
D_out= 200 nm
D_out=300 nm
D_out=400 nm
D_out=500 nm
D_out=600 nm
D_out=700 nm
V
SD
AX
Energy Density (J/m³)
D_in/D_out
t_ins/D_out

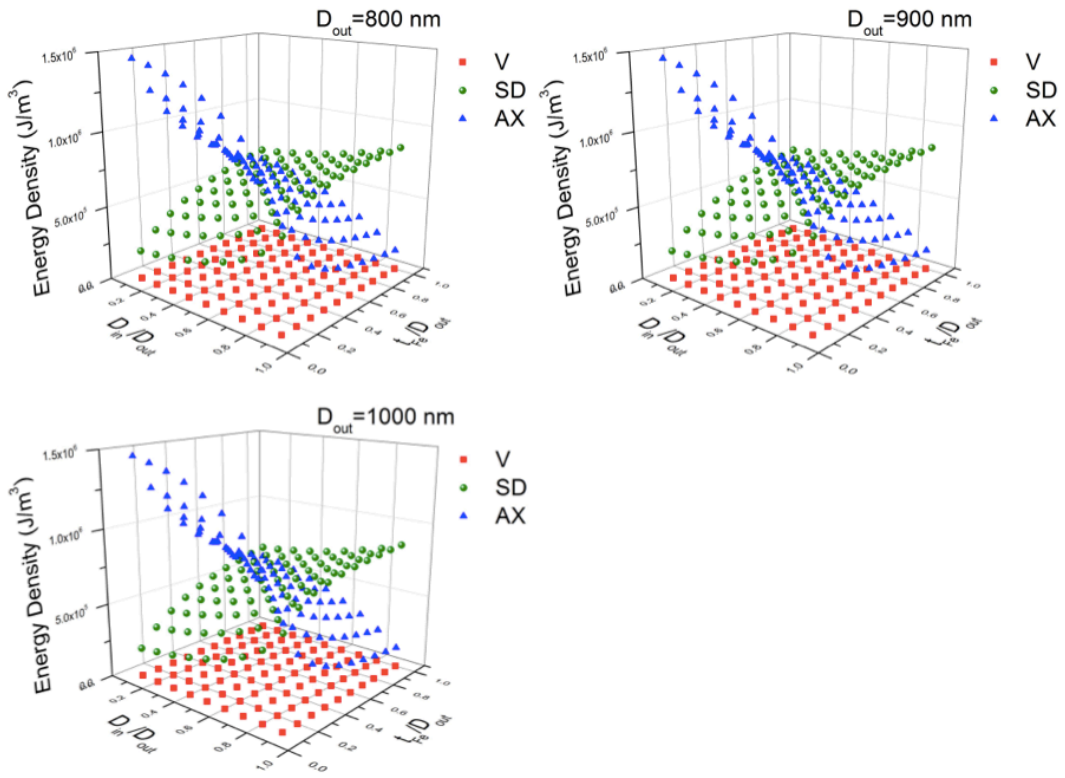

(2) D_{in}/D_{out} fixed, E vs. D_{out} and t_{Fe}/D_{out}:

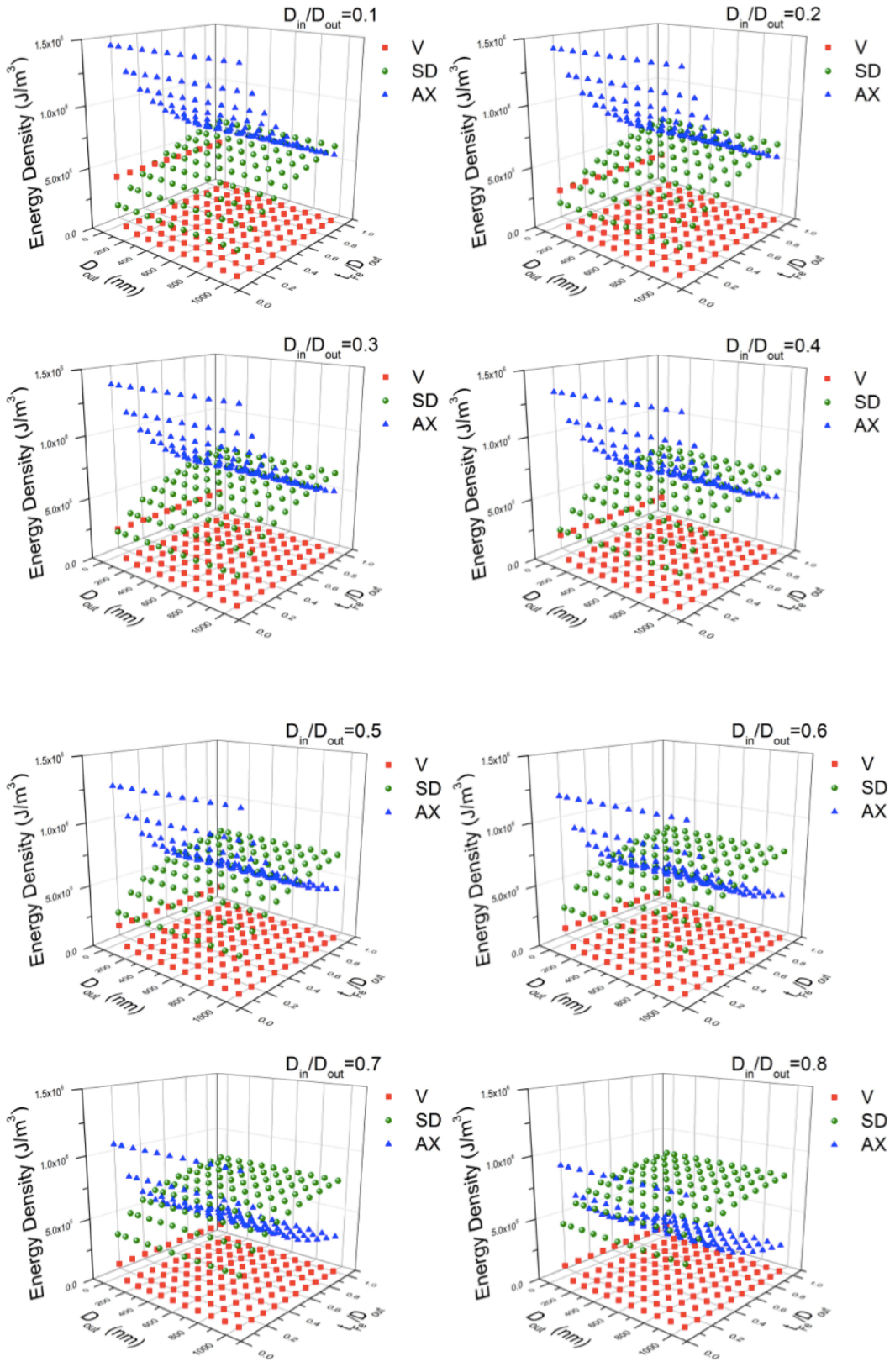
D_in/D_out=0.1
D_in/D_out=0.2
D_in/D_out=0.3
D_in/D_out=0.4
D_in/D_out=0.5
D_in/D_out=0.6
D_in/D_out=0.7
D_in/D_out=0.8
V
SD
AX
Energy Density (J/m^3)
D_out (nm)
t_Fe/D_out

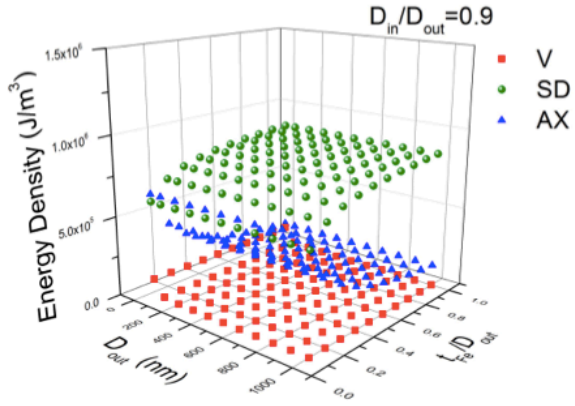

(3) t_{Fe}/D_{out} fixed, E vs. D_{out} and D_{in}/D_{out}:

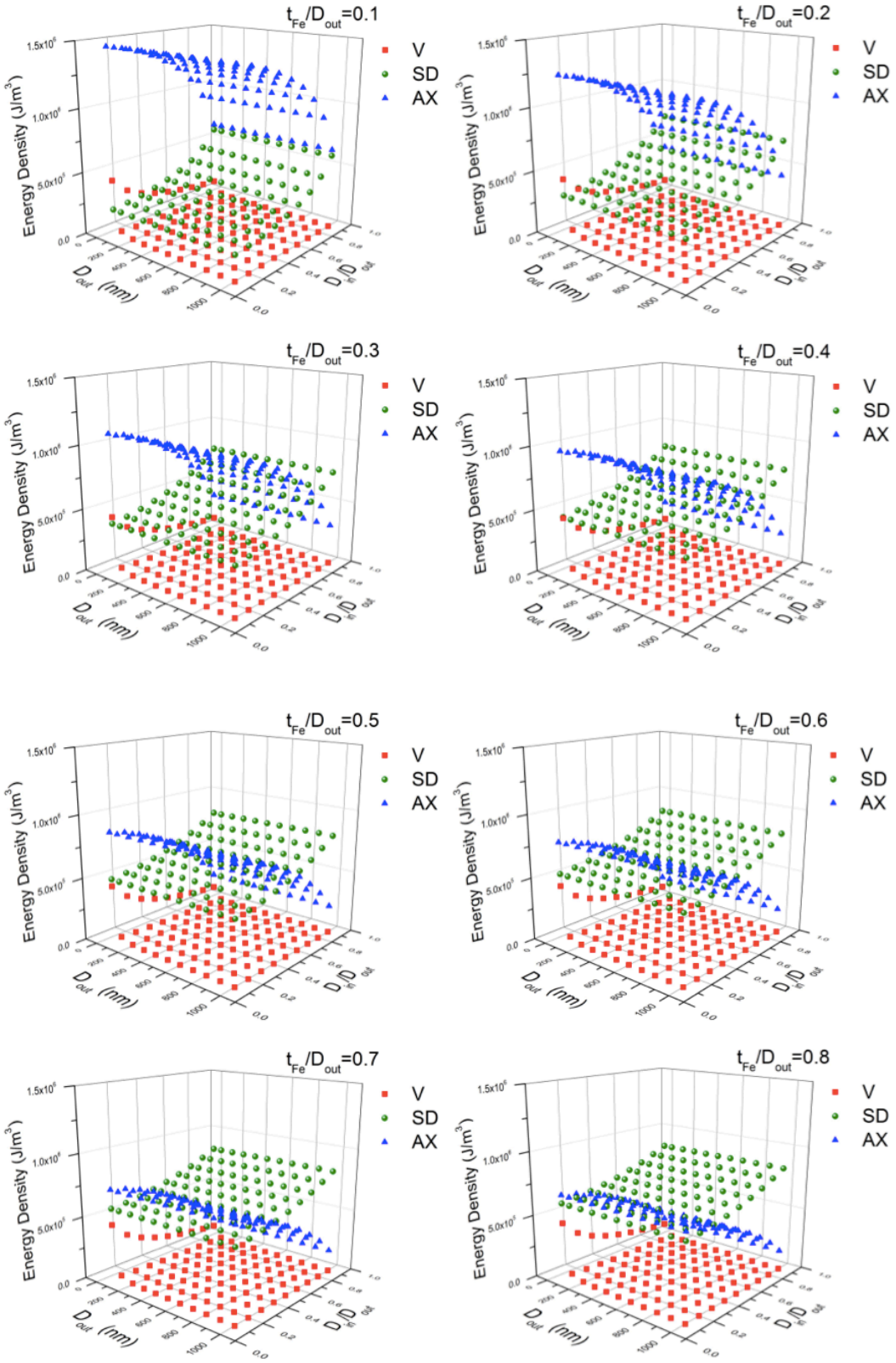
t_{Fe}/D_{out}=0.1
t_{Fe}/D_{out}=0.2
t_{Fe}/D_{out}=0.3
t_{Fe}/D_{out}=0.4
t_{Fe}/D_{out}=0.5
t_{Fe}/D_{out}=0.6
t_{Fe}/D_{out}=0.7
t_{Fe}/D_{out}=0.8
V
SD
AX
Energy Density (J/m^3)
D_{out} (nm)
D_{in}/D_{out}

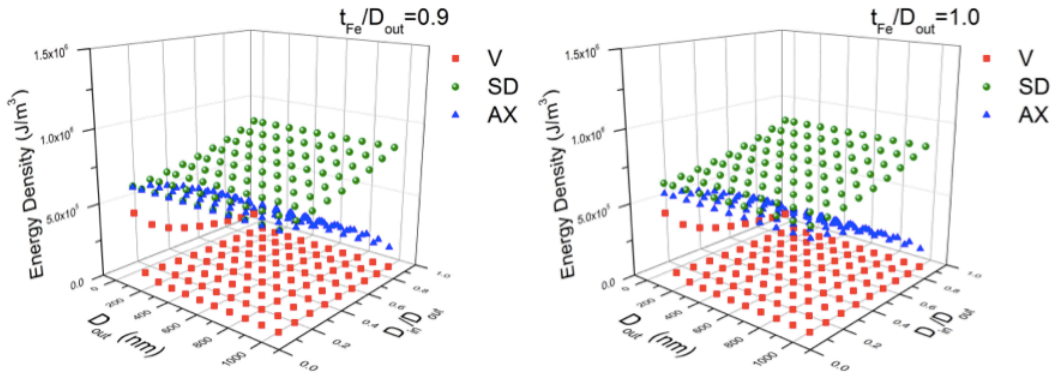
t_{Fe}/D_{out}=0.9
t_{Fe}/D_{out}=1.0
V
SD
AX
Energy Density (J/m^3)
D_{out} (nm)
D_{in}/D_{out}

APPENDIX D

Effect of different materials on the magnetic ring structures

In this thesis, we have discussed the magnetic properties of polycrystalline Fe ring structures. In these polycrystalline Fe ring samples, the easy axes of each small grains are randomly distributed and cancel out with each other, so on the macroscopic level the polycrystalline Fe rings are isotropic. However, if the intrinsic magnetocrystalline anisotropies of the material do not effectively cancel out, such as in the epitaxial Fe or Co thin films, then the magnetic ring structures form some distinct magnetic states as shown in the figure below:

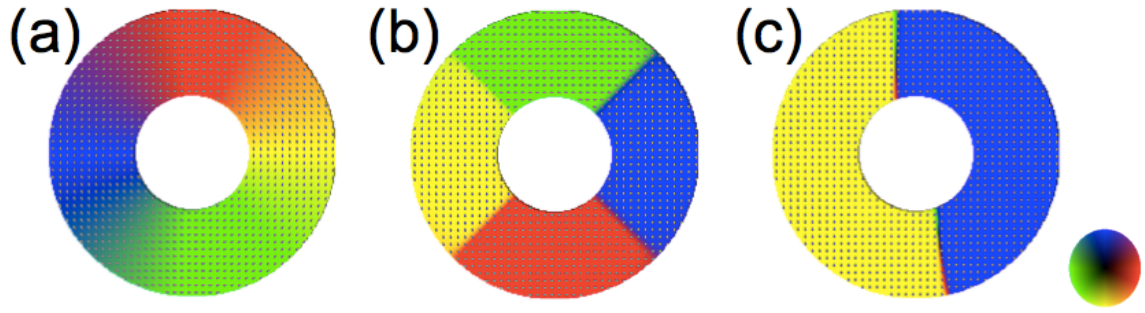

Figure (a) shows the micromagnetic simulated domain image for D_{out}=*500 nm* polycrystalline Fe ring structure at remanence is a vortex state. Figure (b) shows the remanence state for D_{out}=*500 nm* epitaxial Fe ring structure, with its easy axes of the cubic magnetocrystalline anisotropy along the horizontal and vertical directions, is a 4-domain state. Figure (c) shows the remanence state for D_{out}=*500 nm* epitaxial Co ring, with its easy axis of the uniaxial magnetocrystalline anisotropy along the vertical

direction, is a bi-domain state. Therefore, the intrinsic magnetocrystalline anisotropy of the magnetic material can affect the magnetic states the ring structures form.

Besides the magnetocrystalline anisotropy, different values of saturation magnetization M_s and exchange stiffness constant A can also affect the magnetic properties of the ring structures. Here we use polycrystalline Permalloy ($Fe_{0.2}Ni_{0.8}$) with M_s= *800 emu/cm*^{3}, A=*1.05 μerg/cm* (compared with Fe: M_s=*1714 emu/cm*^{3} and A=*12 μerg/cm*) as an example to show how the energy densities of vortex state, single-domain state and axial state change with respect to the ring size (D_{out}), width (D_{in}/D_{out}) and aspect ratio (t/D_{out}).

(1) The effect of ring size (D_{out}) in Permalloy (Py) ring structures:

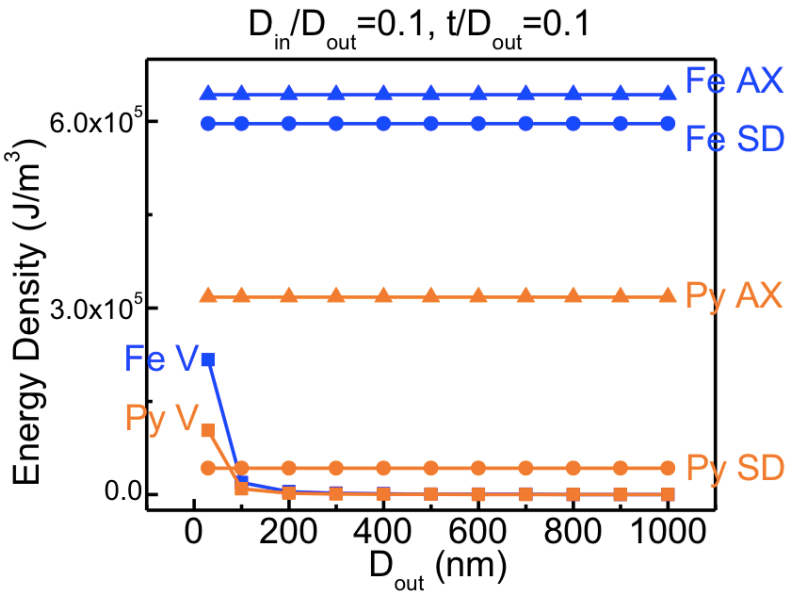

As shown in the figure above, the energy densities of different magnetic states in Py rings are plotted in orange, while their Fe counterparts are plotted in blue. The energy density of the vortex states is plotted with square symbol, while the single-domain state use circle and axial state use triangle.

From the figure, the evolution trends of the energy density in Py rings are the same as in Fe rings. The energy density of vortex state is decreasing with D_{out}, while the energy density of single-domain state and axial state stays constant. However, the energy density of vortex state, single-domain state and axial state are lower than in Fe ring. Increasing D_{out} favors the formation of vortex state in both Py and Fe rings, but the transition size from single-domain state to vortex state in Py is larger than in Fe ring.

(2) The effect of ring width (D_{in}/D_{out}) in Permalloy (Py) ring structures:

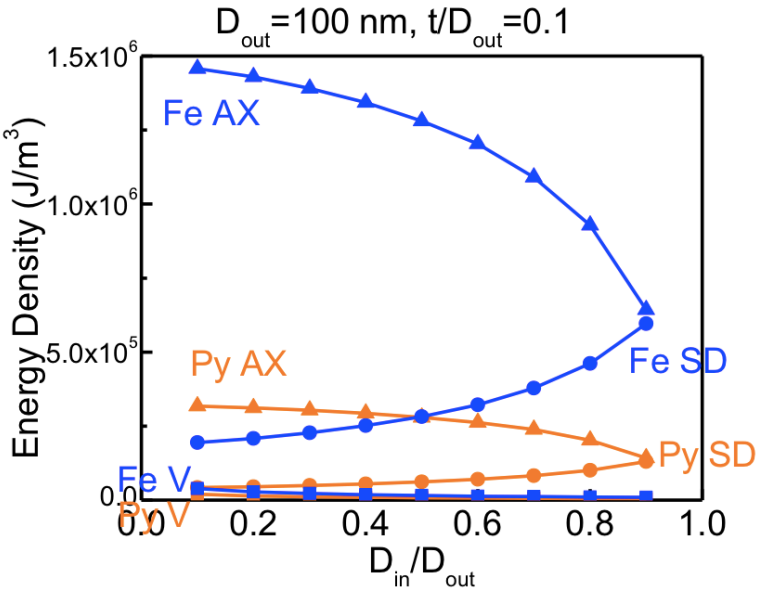

Although in both Py and Fe rings, the energy density of the vortex state and axial state decrease with D_{in}/D_{out}, the energy density of the single-domain state increase with D_{in}/D_{out}. The energy densities of all these three states are lower in Py rings than in Fe rings. Increasing D_{in}/D_{out}. favors the formation of vortex state and axial state.

(3) The effect of ring aspect ratio (t/D_{out}) in Permalloy (Py) ring structures:

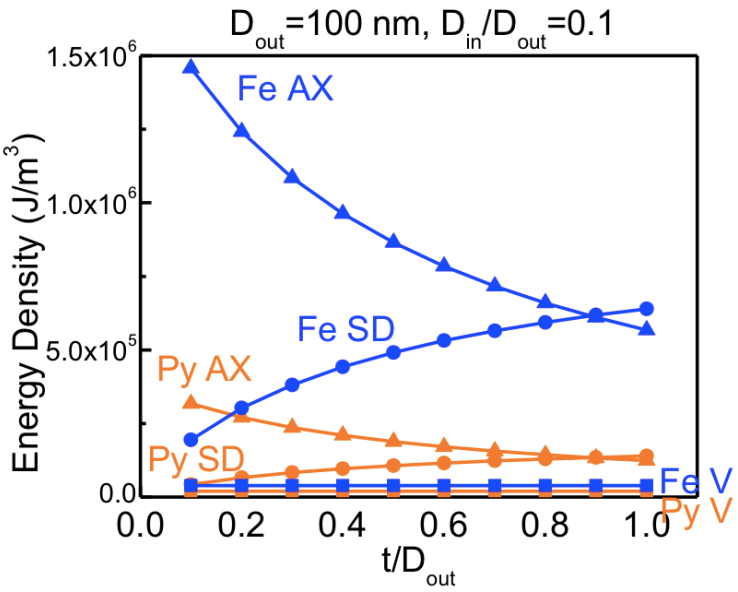

In both Py and Fe rings, the energy density of the vortex state stays constant as t/D_{out} changes. The energy density of single-domain state increases with t/D_{out} while the energy density of the axial state decrease with t/D_{out}. The energy densities of all these three states are lower in Py rings than in Fe rings. Increasing t/D_{out} favors the formation of vortex state and then axial state.

As a conclusion, in other polycrystalline materials with different saturation magnetization M_s and exchange stiffness constant A values, the evolution of energy densities of vortex state, single-domain state and axial state are same in trend as in Fe rings. The energy density of the vortex state increases with D_{out}, D_{in}/D_{out} and is independent with t/D_{out}. The energy density of the single-domain state is independent with D_{out}, while increase with D_{in}/D_{out} and t/D_{out}. The energy density of the axial state shows the opposite trend of the single-domain state. However, the energy densities of all

these three states are lower in Py compared with Fe. The critical transition points between these three states are also different in values.